STUDY OF THE PHOTON CHEMICAL POTENTIAL IN SEMICONDUCTOR RADIATIVE ENERGY CONVERTERS AT MICRO/NANOSCALES

A Dissertation
Presented to
The Academic Faculty

by

Dudong Feng

In Partial Fulfillment
of the Requirements for the Degree
Doctor of Philosophy in the
George W. Woodruff School of Mechanical Engineering

Georgia Institute of Technology
December 2021

Copyright © 2021 by DUDONG FENG

STUDY OF THE PHOTON CHEMICAL POTENTIAL IN SEMICONDUCTOR RADIATIVE ENERGY CONVERTERS AT MICRO/NANOSCALES

Approved by:

Dr. Zhuomin Zhang, Co-Advisor
George W. Woodruff School of Mechanical Engineering
Georgia Institute of Technology

Dr. Peter Hesketh
George W. Woodruff School of Mechanical Engineering
Georgia Institute of Technology

Dr. Shannon Yee, Co-Advisor
George W. Woodruff School of Mechanical Engineering
Georgia Institute of Technology

Dr. Dragica Vasileska
School of Electrical, Computer and Energy Engineering
Arizona State University

Dr. Ajeet Rohatgi
School of Electrical and Computer Engineering
Georgia Institute of Technology

Date Approved: 11/17/2021

To my family

ACKNOWLEDGEMENTS

First and foremost, I would like to express my sincere appreciation and gratitude to my Ph.D. advisors, Dr. Zhuomin Zhang and Dr. Shannon Yee, for their invaluable guidance, continuous support, and tremendous encouragement in my research and daily life at Georgia Tech. Throughout my Ph.D. study, I have been grateful to Dr. Zhang for offering me the opportunity to do scientific research with his mentorship. His patience, rigorous scholarship, and passion have laid down significant influences on my future career. I have also felt fortunate to have Dr. Yee serve as my advisor, who has always been responsive, supportive, and insightful on my research. Without the help from either of my advisors, this dissertation would never be possible.

I would also like to thank Dr. Ajeet Rohatgi, Dr. Dragica Vasileska, and Dr. Peter Hesketh for taking their time serving on my dissertation reading committee and providing me with valuable suggestions and comments. I am indebted to Dr. Rohatgi for not only imparting me knowledge on photovoltaic physics but also offering me his lab facilities for my research. Much appreciation should also go to Dr. Vasileska for her generous knowledge sharing of the simulation and solid-state physics. I am very grateful to Dr. Hesketh for his help on teaching skills during teaching practicum and inspiring me with his breadth of expertise and knowledge. I would like to thank for the funding support from Department of Energy.

Deepest appreciation also extends to my former and current group members in both Nanoscale Thermal Radiation Laboratory and the Scalable Thermal Engineering Laboratory. I would like to thank Dr. Eric Tervo particularly for his tutorship, enlightening

discussions and fruitful collaborations. I also appreciate Dr. Peiyan Yang, Dr. Xiaohu Wu, Dr. Zhaolong Wang, Chuyang Chen, Chiyu Yang, Shin Young Jeong, Matthew Burg and Preston Bohm for their help and discussions. Many thanks to Dr. Bo Zhao, Dr. Xianglei Liu, Dr. Liping Wang, Dr. Keunhan Park, Dr. Richard Zhang. Dr. Ceji Fu, and Dr. Bong Jae Lee for their advice and tutoring on the research. Much appreciation also goes to Dr. Andrey Gunawan, Aravindh Rajan, Daron Spence, Jordan Kocher, Josh Rinehart, Dr. Alexander Lima, Jong Ha, Dr. Michael Adams, Amalie Atassi, Dr. James Ponder, and Dr. Daniel Morton. I would also like to thank Dr. Young Woo Ok and Wookjin Choi from Dr. Rohatgi's lab, and Dr. Durga Rao GaJula from IEN, for their effort on the sample fabrication. Great thanks to all the people who directly or indirectly help and assist me during my Ph.D. study.

Finally, I would like to express all my love and thanks to my friends and family, who make me feel beloved and supported. Without the company from any of you, I could not reach where I am now and open out on my next milestone.

TABLE OF CONTENTS

LIST OF TABLES

LIST OF FIGURES

LIST OF SYMBOLS AND ABBREVIATIONS

A, B, C, D	Amplitude coefficients
a, b	matrix summation operator of three orthogonal components
$\mathbf{B}$	magnetic field, T
$C_{(\mathrm{e,h})}$	Auger recombination coefficient, $\mathrm{m}^{-6}\ \mathrm{s}^{-1}$
c	speed of light in vacuum, 299 792 458 m s^{-1}
$\mathbf{D}$	Electric displacement field, A
$D_{(\mathrm{e,h})}$	diffusion coefficient, m s^{-2}
d	thickness or gap distance, m
$\mathbf{E}$	electric field, V m^{-1}
$E_{\mathrm{c}}, E_{\mathrm{v}}$	conduction and valance band energy, J
E_{f}	Fermi energy, J
E_{g}	bandgap energy, $\hbar\omega_{\mathrm{g}}$, J
E_{i}	intrinsic Fermi energy, J
e	elementary charge, 1.6×10^{-19} C
e^{-}, h^{+}, ph	electron, hole, and photon
F	function
G	Gibbs free energy, J
$\mathbf{G}$	Green's function, m^{-1}
G	generation rate, m^{-2}
$\mathbf{g}$	dyadic Green's tensor, m

$\mathbf{H}$ magnetic field, A m^{-1}

h height, m

$\hbar$ the reduced Planck constant, 1.055×10^{-34} J s

$\mathbf{I}$ unit matrix

i $\sqrt{-1}$

J current (density), A m^{-2}

$\mathbf{J}$ fluctuating current density field, A m^{-2}

J_0 (reverse) saturation current, A m^{-2}

j,m,L layer j, m and L

k magnitude of wavevector, m^{-1}

k_0 wavevector in vacuum

k_B Boltzmann constant, J K^{-1}

$\mathbf{M}$ matrix

N particle number

N_A, N_D acceptor and donor concentration, m^{-3}

n_i intrinsic donor concentration

n, p electron and hole concentration, m^{-3}

n_0, p_0 donor concentration at equilibrium

P pressure, Pa

P output power density, W m^{-2}

Q absorbed power density, W m^{-2}

q radiative heat flux, W m^{-2}

R rectification ratio

R recombination rate, m^{-2}

R_b Bulk recombination rate, m^{-2}

R_s surface recombination rate, m^{-2}

$\mathbf{R}$ matrix of Fresnel's reflection coefficients

r recombination density rate, m^{-3}

$\mathbf{r}, \mathbf{r}', \mathbf{r}''$ random location in a cylindrical coordinate

r, t Fresnel's reflection and transimission coefficient

S entropy, $J\ K^{-1}$

$\mathbf{S}$ Poynting vector

S surface recombination velocity

$\hat{\boldsymbol{s}}, \hat{\boldsymbol{p}}$ TE- and TM-polarized unit vector

T temperature, K

t time, s

t depth into cell, m

V volume, m^3

V voltage, V

W_{J_m,J_n} product of imaginary part of dielectric function from two fluctuating currents

x, y, z Cartesian coordinates

z' Source location, m

z_t top surface location of *p*-region in z component, m

z_b bottom surface location of *n*-region in z component, m

z_d detected location, m

Greek symbols

α	absorption coefficient, m^{-1}
β_{max}	max parallel wavevector, rad s^{-1}
γ	damping frequency, rad s^{-1}
Δz	thickness of one layer
δ	Dirac delta function
ε	relative permittivity
ε_0	electric permittivity of vacuum, 8.854×10^{-12} F m^{-1}
η	energy conversion efficiency
Θ	mean energy of a Planck oscillator base on Bose-Einstein distribution, J
μ	photon chemical potential, J
μ_0	magnetic permeability of vacuum, $4\pi\times10^{-7}$ H m^{-1}
υ	mobility, m^2 V^{-1} s^{-1}
ξ	energy transmission coefficient
ρ,θ,z	polar coordinates
ρ_e	charge density
τ	relaxation time, s
Υ	fraction of absorbed photons
Φ	spectral transmission coefficient
Ψ	modified Bose-Einstein statistics
ψ	Bose-Einstein statistics
φ	electric potential, V

χ_g	relative error
ω	angular frequency, rad s^{-1}
ω_g	frequency corresponding to the bandgap, rad s^{-1}
ω_p	plasma frequency, rad s^{-1}

Superscripts

*	complex conjugate
^	unit vector
',""	real and imaginary part
+, -	front and back
E, H	electric and magnetic components

Subscripts

$\perp$	ordinary
$\|\|$	parallel component or extraordinary
∞	infinite
Auger	Auger recombination
avg	average
b, t	bulk, trap
cell	cell
dark	dark condition
diff	diffusion

eff	effective
e, h	electron and hole
FE	fluctuational electrodynamics
g	corresponding frequency of the bandgap
ib	interband
LO, TO	longitudinal and transverse optical
lum	luminescence
max	maximum
min	minumum
nonrad	nonradiative
n, p	n and p region
oc	open-circuit
pn	*pn* diode
rad	radiative
ref	reference
r, f	reverse and forward
SRH	Shockley-Read-Hall recombination
sc	short-circuit
s, *p*	s- and p-polarization
thermal	thermal radiation
vrs	van Roosbroeck-Shockley
x, y, z	component direction
zz	tensor component of z direction with z basis.

SUMMARY

Radiative energy converters are semiconductor devices that realize energy conversions between thermal energy and electricity. These newly proposed solid-state heat engines/pumps are considered as promising technologies for energy harvesting and conversion applications on thermal energy storage, aerospace power generation, local thermal management, and thermal regulation for building and human thermal comfort. This dissertation is designated to develop a detailed and comprehensive modeling method to depict the photon-charge coupled transport for radiative energy converters, investigate the unique physical phenomena induced by the photon chemical potential inside the devices and explore the performance enhancement by using two-dimensional (2D) materials.

A modification of the direct method is proposed using Boltzmann approximation to link the conventional and direct method for the modeling of near-field TPV cells. By contrasting different modeling approaches, the effect of evanescent waves on the dark current of a near-field TPV cell is quantitatively analyzed for different emitter and cell materials.

To fully model a working near-field TPV cells, an iterative solver that combines fluctuational electrodynamics (FE) with the drift-diffusion (DD) model is developed to tackle the coupled photon and charge transport problem, enabling the determination of the spatial profile of photon chemical potential beyond the detailed balance approach. The difference between the results obtained by allowing the photon chemical potential to vary spatially and by assuming a constant value demonstrates the limitations of the conventional approaches.

The performance improvement on a thin-film, near-field InAs TPV device with a back gapped reflector is investigated, comparing its performance to that with a conventional metal back surface reflector. Surface passivation conditions are also investigated to further improve the performance of TPV devices with back reflectors. The output power and efficiency are calculated using the newly proposed photon-charge coupled model. The absorption of the back reflectors and external luminescence loss are analyzed to explain the performance improvement.

The external radiative recombination in thin-film, near-field radiative energy converters is investigated using FE. The spatial profile of the local external radiative recombination coefficient is calculated to investigate the thin-film effect, geometric effect, and doping effect on the external luminescence of a thin-film radiative energy converters under different configuration and working conditions.

A novel photonic thermal diode is achieved in the near-field regime by coupling (or decoupling) the hyperbolic phonon polaritons (HPhPs) in hexagonal boron nitride (hBN) and temperature-dependent interband transition of indium antimonide (InSb). Taking the advantages of the forward bias operation condition, a near-field thermoradiative device with high performance can be realized.

This thesis provides a comprehensive investigation of optical and electrical processes of radiative energy converters, which can benefit the design and optimization of solid-state energy converters with wide application scenarios. Fundamental understanding of the photon chemical potential may exploit a new pathway of control the radiative heat transfer for both far- and near-field regimes.

CHAPTER 1. INTRODUCTION

All forms of matter emit radiation through various mechanisms. Since Kirchhoff first introduced the term of *black body* in 1860, thermal radiation, also known as blackbody radiation, has stood in the spotlight throughout the history of classical physics. Almost all the biggest names in physics and math have contribute to the establishment of classical electromagnetism. To summarize from the perspective of thermodynamics treatment of electromagnetism [1], Josef Stefan and Ludwig Boltzmann complete the derivation of Stefan-Boltzmann law to describe the intensity radiated from a black body as a function of temperature. Wien derived the Wien's displacement law and Wien's spectrum to describe the blackbody spectrum at short-wavelength region. The Rayleigh-Jeans formula proposed by Lord Rayleigh and Sir James Jeans matched with blackbody spectrum at high temperature and long wavelengths range [2]. The study of blackbody radiation culminated until Max Planck obtained Planck's law to fully describe the blackbody spectrum based on Boltzmann's entropy expression. In his book *The Theory of Heat Radiation*, Planck created the "quanta" hypothesis to derive Planck's law [3], which opened the door to the modern physics.

As depicted by Planck's law, thermal radiation is essentially thermally excited electromagnetic waves, whose intensity and spectrum are only a function of local temperature. However, according to the dual theory, thermal radiation can also be characterized as a photon gas with zero chemical potential because the number of photons is not conserved in a blackbody enclosure. However, in general, photons obey the Bose-Einstein statistics and can carry chemical potential via thermodynamic processes or

photochemical reactions, such as interacting with other quasiparticles [1, 4, 5]. For a semiconductor, the emission or absorption of photons whose energies exceed the bandgap energy (E_g) are mainly associated with the radiative recombination or photogeneration processes, in which an electron-hole pair is either eliminated or created. To represent the interaction between the electron-hole pairs (e^- and h^+) and photons (ph), a photochemical reaction is given:

$$e^- + h^+ \rightleftharpoons ph \tag{1.1}$$

From a thermodynamics point of view, the Gibbs free energy should be conserved in these processes, which can be written as [6]:

$$d\,\mathrm{G} = -\mathrm{S}\,dT - \mathrm{V}\,d\,\mathrm{P} + \sum_i \mu_i dN_i \tag{1.2}$$

where the product of entropy (S) and the change of temperature (T) represents the heat exchanged in a grand canonical ensemble, and the product of volume (V) and the change of pressure (P) is defined as compressional energy. The total change of chemical potential of this system can be calculated by the summation of the chemical potential change of each quasiparticle, which is expressed as the chemical potential (μ_i) times the change of quasiparticle number (N_i). [6].

With the assumption of a steady-state system at local equilibrium of temperature and pressure, the conservation of the Gibbs free energy can be simplified [1, 6]:

$$\mu_\mathrm{e} dN_\mathrm{e} + \mu_\mathrm{h} dN_\mathrm{h} = \mu_\mathrm{ph} dN_\mathrm{ph} \tag{1.3}$$

Since the number of the electron-hole pairs is equal to that of generated photons, i.e., the photon chemical potential should equal the difference between those of the electrons (μ_e) and holes (μ_h), which is expressed as [1]:

$$\mu_{ph} = \mu_e + \mu_h = E_{f,e} - E_{f,h} \tag{1.4}$$

where $E_{f,e}$ and $E_{f,h}$ are the quasi-Fermi levels of electrons and holes in a semiconductor. In a nonequilibrium semiconductor, the radiative recombination and photogeneration are simultaneously proceeding. These photons that emitted from such semiconductors carry a photon chemical potential and is defined as non-thermal radiation or luminescence, which is a function of both temperature and chemical potential at local equilibrium. The emitted photon flux may be higher or lower than that from a blackbody at the same temperature,

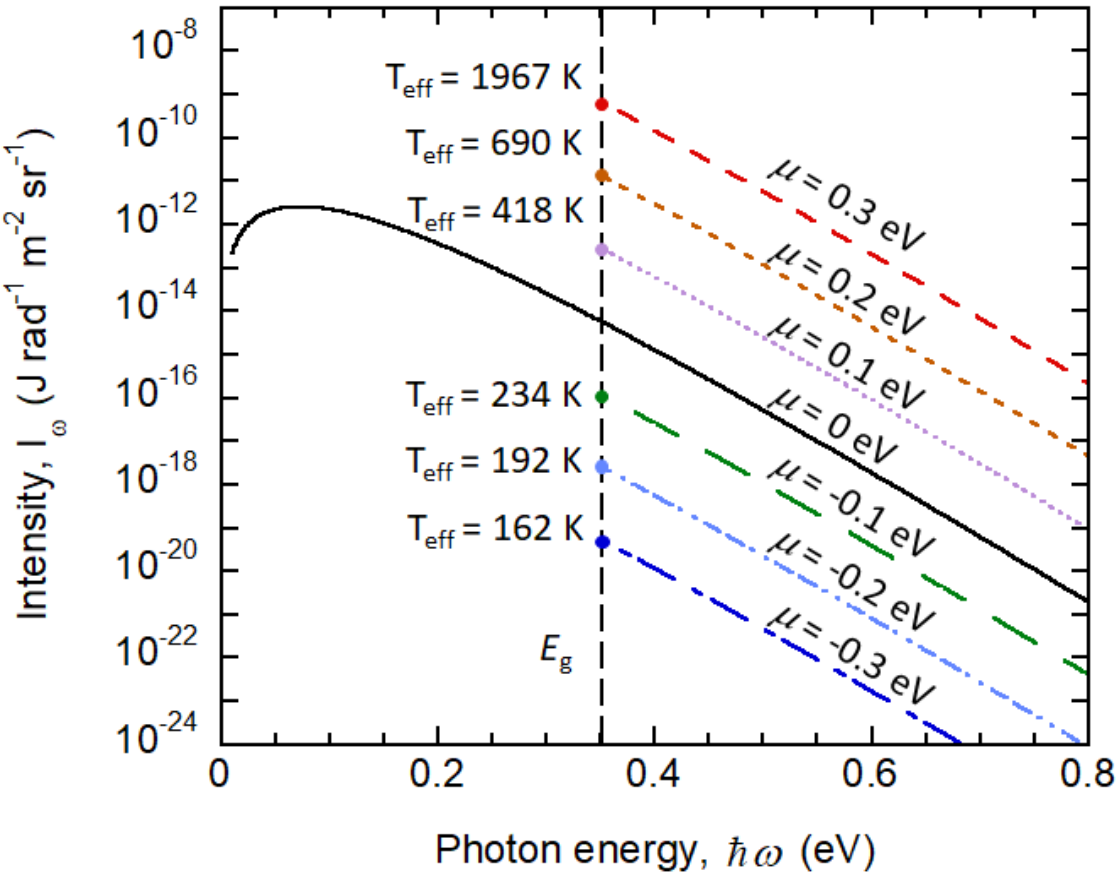

Figure 1.1 Spectral intensity and apparent temperature for a blackbody semiconductor with a bandgap energy of 0.354 eV at 300 K under varying photon chemical potential.

depending on whether photon chemical potential is positive or negative, resulting in luminescence or negative luminescence effects. Let us assume a photon chemical potential on a semiconductor material with bandgap energy $E_g = 0.354$ eV (corresponding to that of InAs). It can be seen in Figure 1.1 the spectral intensity increases significantly at frequencies above the bandgap, especially when the chemical potential is close to the bandgap energy. The effective or apparent temperature can approach to 2000 K at the bandgap frequency with $\mu = 0.3$ eV when compared to the equilibrium blackbody (300 K) spectral intensity. Reversely, the spectral intensity is suppressed and the effective temperature can be lower than the blackbody temperature when photon chemical potential is negative. The luminescence effect is essential to the operation of light-emitting diodes (LEDs) [1]. Furthermore, radiative energy converters may also be subject to nontrivial electroluminescence due to the radiative recombination of injected electrons and holes in different radiative energy converters, especially in the near-field regime [5, 7-11].

In general, photovoltaic (PV) cells and LEDs are the archetypical examples of the radiative energy converters without an emitting/receiving body. By tunning the photon chemical potential and the working temperatures, radiative energy converters can realize energy conversion between thermal radiation and electrical energy. As shown in Figure 1.2, four kinds of radiative energy converters are investigated in this thesis and they are made of three components: a p-n diode, an emitter/receiver, and a vacuum gap separating these two bodies. Depending on whether the *p-n* diode is generating or consuming electricity, the device can operate as a heat engine: thermophotovoltaic (TPV) cell and thermoradiative (TR) cell, or a heat pump: electroluminescent refrigerator (EL) and negative electroluminescent refrigerator (NEL). TPV cells generate electrical current by

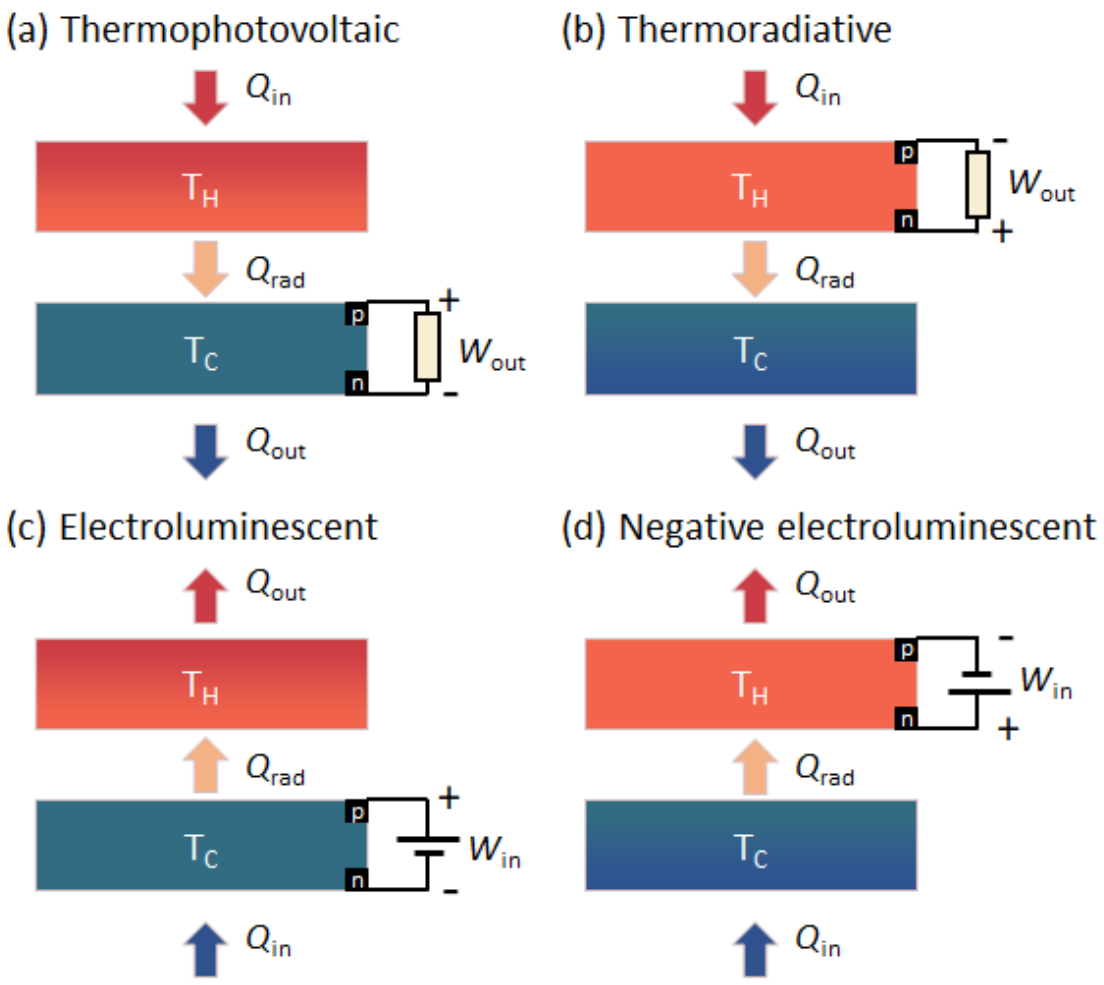

Figure 1.2 Schematics of the four types of radiative energy converters: (a) TPV cell, (b) TR cell, (c) EL refrigerator, and (d) NEL refrigerator.

absorbing thermal radiation from hot objects; while TR cells generate electrical current by emitting thermal radiation to cold objects. In a likely manner, EL refrigerators can cool the objects by emitting more luminescence to the surroundings; while NEL refrigerators can cool the surroundings by suppressing the luminescence from the refrigerators [2, 5, 7]. A representative current-voltage characteristic (i.e., the *J-V* curve) diagram for four types of radiative energy converters is shown in Figure 1.3. The four *J-V* curves are essentially diode curves when facing another body at different temperatures. Both the *J-V* curves of

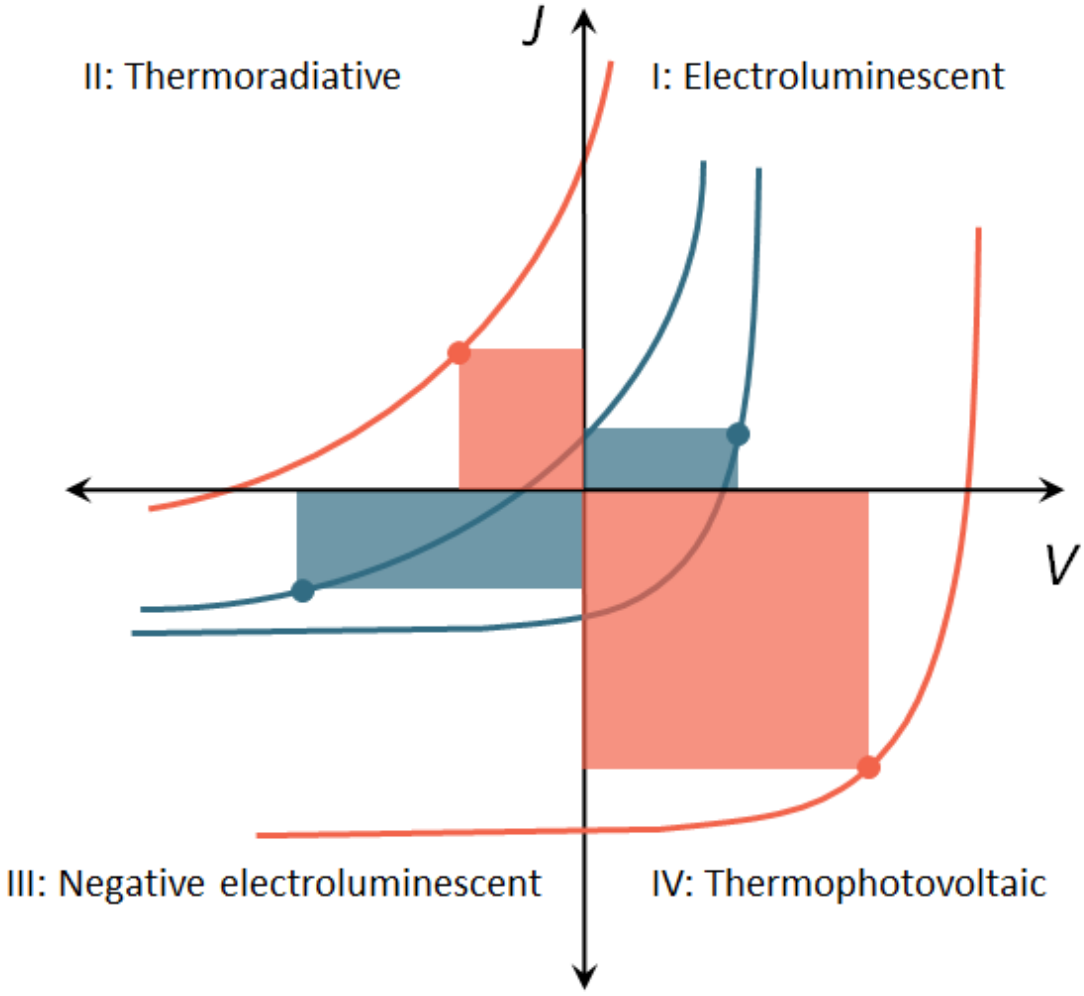

Figure 1.3 The current-voltage characteristics of four types of radiative energy converters.

TPV and EL are created by shifting a diode curve downward, since the emitter/ receiver possesses a higher temperature than the *p-n* diode. While the *J-V* curves of TPV and EL are created by shifting a diode curve upward, since the temperature of the emitter/receiver is lower than that of the *p-n* diode. Since TR cells and TPV cells operate as heat engines, their operation conditions locate at the second and fourth quadrant of the *J-V* diagram, respectively, where the output powers of the devices are positive. Therefore, the second and fourth quadrant represent the load quadrants, which produce electrical power. While

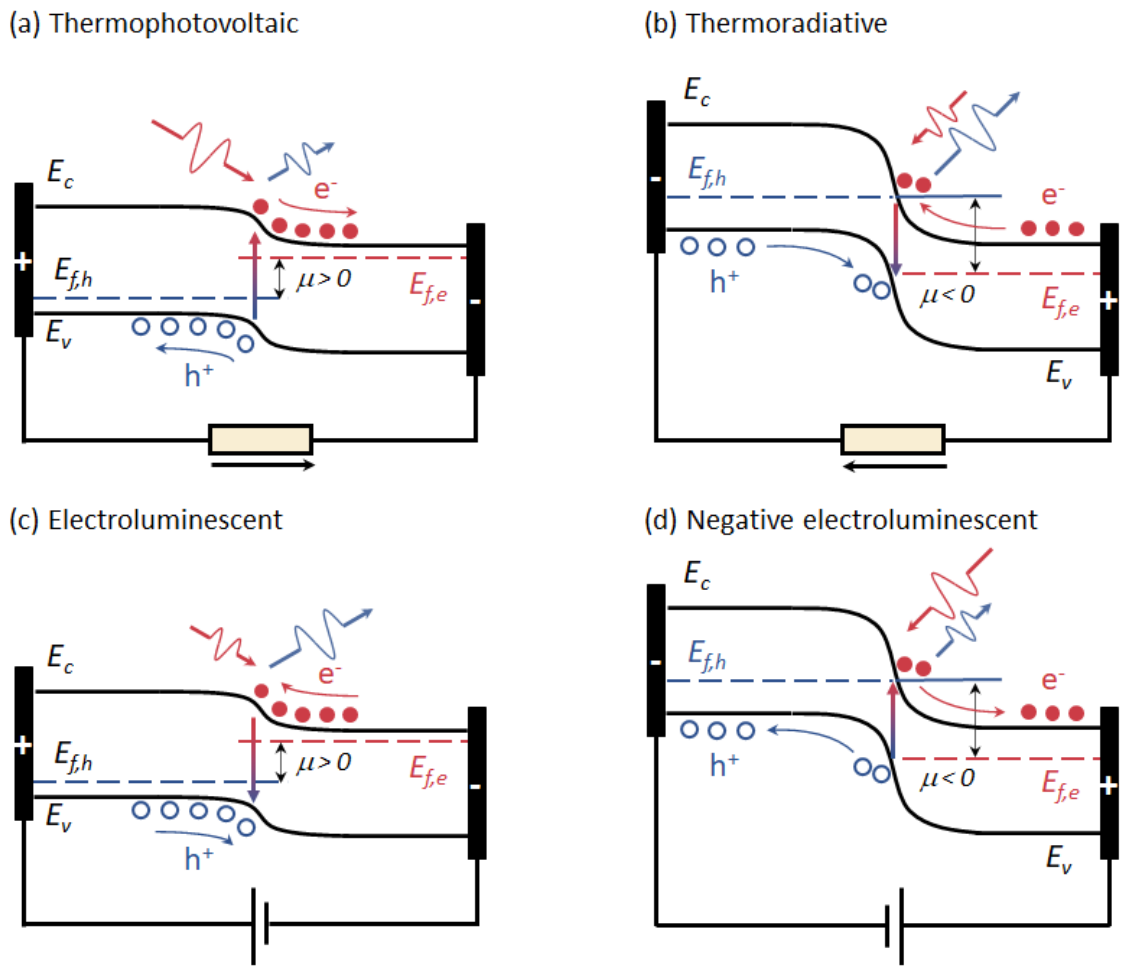

Figure 1.4 Band diagrams of a working (a) TPV cell, (b) TR cell, (c) EL refrigerator, and (d) NEL refrigerator under illumination and bias, showing the conduction band (E_c), valence band (E_v), and quasi-Fermi levels whose difference equal the photon chemical potential.

EL refrigerators and NEL refrigerators are working as heat pumps, thus the operation conditions locate at the first and third quadrant of the *J-V* diagram, where the output powers of the devices are negative. Therefore, the first and fourth quadrant represent the power supply quadrants, which consume electrical power. The shadowing areas represents the power consumed or supplied for different radiative energy converters.

The working band diagrams of four types of radiative energy converters are shown in Figure 1.4. For a working TPV cell, an incident photon above the bandgap energy is absorbed by a TPV cell, which generates one electron–hole pair. Some of these free carriers are separated in the depletion region and flow in opposite directions, providing electrical power to an external load. Meanwhile, some of these excess electrons and holes recombine and generate luminescent photons, which carry a positive chemical potential equal to the difference between the quasi-Fermi levels of the electrons and the holes. For a working TR cell, the temperature of the *p*-*n* diode is higher than that of the surroundings or the receiver. Although there are incoming photons generating free carriers, more electron-hole pairs recombine in the *p*-*n* diode and emit out photons, which carry a negative chemical potential. As the bias becomes more and more negative, the luminescence effect is suppressed and the TR cell reaches a balance of radiative recombination and photogeneration with an output power. Reversely, when one electrically injects free carriers into the *p*-*n* diode and create a positive photon chemical potential, it can function as a EL refrigerator since the external luminescence intensity is larger than the summation of incoming radiation and Joule heating. Similarly, the free carriers in the *p*-*n* diode can be electrically taken away to create a negative photon chemical potential, which results a suppression on the external luminescence. Therefore, the *p*-*n* diode can absorb more photons from the surroundings/receiver of same temperature to act as a refrigerator.

Due to the growing concerns of climate change and environment pollutions, conventional energy generation and conversion technologies are urgently required to be replaced by clean energy innovation. The radiative energy converters with the advantages of compact size and solid-state operation are promising alternatives to conventional thermal-fluid thermodynamic cycles for power generation and heat pumping, which make these device

attractive candidates for a variety of applications, such as local thermal storage, waste heat recovery, solar and nuclear energy conversion, aerospace power generation, thermal management and building thermal regulation [2, 12-18].

Near-field radiation is derived from near-field optics [2]. When the separation distance between two objects or the size of radiant bodies is comparable or smaller to the characteristic wavelength, the radiation transport may exceed the blackbody limit depicted by Planck's law. However, Planck already indicated this issue when he made the fundamental assumption to derive the blackbody radiation in his book [3], "*Throughout the following discussion it will be assumed that the linear dimensions of all parts of space considered, as well as the radii of curvature of all surfaces under consideration, are large compared with the wavelengths of the rays considered.*" Coupled evanescent waves from total internal reflection and surface polaritons in certain materials dominate the radiative heat exchange in the near-field, which leads to the enhancement of radiative heat flux by several orders of magnitude [2, 19-27]. Maxwell's equations perfectly describe the propagation of electromagnetic waves in media, while they are not sufficient to solve the radiative heat transfer between two separated bodies. By treating thermal radiation as the spontaneous emission originating from random thermal fluctuation of dipoles in a medium with temperature larger than 0 K, Rytov et al. [28] established the fluctuational electrodynamics (FE) by combining the fluctuation-dissipation theorem with Maxwell's equations, which first gave detailed and comprehensive mathematical expressions to link the local equilibrium temperature and thermal radiation. Following this groundbreaking work, the theoretical studies and numerical methods on near-field radiative heat transfer are performed in planar structures [29-36] , tip/sphere-plane structures[37-41], sphere-sphere structures [40, 42, 43] and even arbitrary geometries [44, 45]. The experimental

demonstrations of near-field radiation enhancement are conducted since last century. Due to the limitation of micro fabrication techniques, the near-field enhancement on the radiative heat transfer can only be demonstrated qualitatively by some pioneer works [46-50]. Boosted by the advancement of nanotechnologies and computational powers, researchers have measured the near-field radiative heat transfer in various configurations made of dielectrics, metals, semiconductors, and metamaterials [51-71], and detailed discussions can be found in the review articles [27, 72]. The experimental demonstrations of near-field radiation enhancement pave the way for applying near-field radiation to radiative energy converters to further improve their performance.

Among the four types of radiative energy converters, TPV cells have been most extensively investigated because the technical developments in the solar cell industry can almost be transplanted due to their similarities in operation. Whale and Cravalho first proposed the concept of a near-field TPV device with a simplified model predicting performance improvements on its power density and efficiency [73]. Inspired by this pioneer work, extensive efforts have been put into the theoretical modeling to investigate the fundamental mechanism and theoretical limit of near-field TPV devices, and the design of novel emitters and absorbers to further improve the performance of near-field TPV devices. Large number of theoretical investigations on the optical and electrical processes in near-field TPV devices have provided a comprehensive understanding about the working principle and unique physical phenomena of this radiative energy converter [73-87]. The optimizations on the design of the emitter and cell include using 2D materials (i.e., graphene [88-92] and hyperbolic metamaterials [93-95]), photonic structures (i.e., thin-film [8, 96-98], gratings [99-101], nanowires [102, 103], multilayered photonic crystals

[104-108]), waveguides [109, 110], and back reflectors [111, 112]. Instead of using *p-n* diode, some other works explored the possibility of using Schottky junctions [92, 113, 114] and tandem cells [115]. Experimental studies were carried out as early as 2001 [116] and 2007 [117] with qualitative demonstration of near-field enhancement effect on the device performance. More recently, several works from three different groups reported the realization of near-field TPV device with quantitative demonstrations of practical surface areas [118-122].

TR cells made of a *p-n* diode has been experimentally demonstrated at room temperature by Santhanam and Fan, however, there are only theoretical studies on the performance analysis of near-field TR cells [82, 123-128]. The Auger generation and reliability of semiconductors at moderate temperature (> 500 K) are the largest practical concerns to realize such devices [14]. As stated by numbers of publications [129-143], EL in the far-field operation can predict very little cooling capacity with low efficiency since the nonradiative recombination processes cause parasitic heating and deteriorate the performance. The experimental demonstrations of the EL refrigeration validated the theoretical prediction on the performance [144-146]. One important way to improve the performance of EL refrigeration is adding a PV cell to collect the emitting photons from the LED to compensate the electricity consumed by the LED. This is also as known as thermophotonic (TPX) cooling, which was first proposed by Green [147, 148]. More information about the development of EL refrigeration and TPV cooling can be found in the review articles [5, 149-151]. Accounting for the struggle of far-field EL refrigeration, several theoretical works have already demonstrate that near-field operation can provide apparent benefits of large cooling power and high extraction efficiency of photons [9, 152-

154]. Although the experimental demonstration of the EL refrigeration effect should be in the near future, there is still a long journey for the EL refrigeration to be compete with conventional refrigeration cycles and the major challenges would remain in the finding of LED materials with high light extracting efficiency [5]. Negative luminescence effect in a reversely biased semiconductors has been discovered for decades [155-157]. Although the refrigeration application of negative luminescence effect has been studied less than the EL refrigeration effect [11], near-field NEL has been experimental demonstrated by Zhu et al. [158]. Despite these radiative energy converters, multiple devices can combine together to made a complex energy converter, such as TPX refrigerators or TPV-TR devices. The studies of radiative energy converters in the near-field operation only started recently, therefore, there are enormous research opportunities in near-field radiative energy converters, which can potentially provide a new solution for energy crisis, global warming and environment pollutions.

This dissertation is divided into 8 chapters. Chapter 2 gives an introduction of theoretical backgrounds of the modeling methods for optical and electrical processes in radiative energy converters. This chapter presents the fundamentals of near-field radiation in stratified media made of isotropic and anisotropic materials. Detailed balance analysis and drift-diffusion model for charge transport inside semiconductor materials are also covered in Chapter 2. Chapter 3 discusses the effect of evanescent waves on the dark current of near-field TPV devices. A comparison between conventional model and direct model is conducted to address the importance of near-field effect on the performance prediction of near-field TPV devices. Chapter 4 introduce an iterative solver of photon-charge coupled model to simulate the transport phenomenon inside near-field TPV devices.

The spatial profile of photon chemical potential is also discussed with an emphasis on the relation between applied bias and local photon chemical potential. By means of newly proposed photon-charge coupled model, Chapter 5 shows the performance improvement of a near-field TPV device by replacing a conventional metal back reflector with a back gapped reflector. Chapter 6 presents a comprehensive model of external luminescence especially for thin-film radiative energy. The spatial effect and doping effect on the external luminescence are also discussed in Chapter 6. This chapter also quantitatively distinguish the non-thermal and thermal radiation above the bandgap energy of semiconductors. Chapter 7 introduces a novel design for near-field photonic thermal diode and near-field thermoradiative device by employment of 2D metamaterials. Finally, Chapter 8 summarizes all the findings and conclusion of this dissertation with future direction of this research.

CHAPTER 2. THEORETICAL BACKGROUND

This Chapter covers the common modeling methods used in radiative energy converters, which can be divided into two parts: photon transport and charge transport. In section 2.1, the fundamental theory of the fluctuational electrodynamics (FE) and recursive transfer matrix method for both isotropic and anisotropic stratified media is discussed. The near-field radiative heat transfer between two semi-infinite bulks is explicitly expressed. Section 2.2 introduces two modeling methods and their theoretical hypotheses to characterize the charge transport mechanism.

2.1 Photon Transport within Radiative Energy Converters

The classical theory of radiative heat transfer is considerably simplified by using geometric optics, where the thermal energy of the emitting object is all converted to propagating electromagnetic waves. The radiant intensity carried by the propagating waves from an object can be characterized by Planck's law with integration of wavelengths and hemispherical emissivity. Nonetheless, if the vacuum gap between objects exchanging radiation is comparable or smaller than the characteristic thermal wavelength, the evanescent modes of electromagnetic waves resulted from total internal reflection (i.e., frustrated modes) and surface resonance (i.e., surface modes) can tunnel though the vacuum spacing and the wave nature of electromagnetic waves can result in interference effect. The near-field tunneling phenomenon is also as known as photon tunneling effect, which are not captured by the classical far-field radiative heat transfer. To fully describe the photon transport phenomenon within radiative energy converters for both far-field and near-field operation conditions, FE approach coupling the fluctuation-dissipation theorem

and Maxwell's equations provides a mathematical solution to calculate the radiative heat transfer or the number of exchanging photons between any two source points within a radiative energy converter.

2.1.1 Fluctuational Electrodynamics

From the perspective of electromagnetics, thermal radiation originates from the random thermal fluctuations of the charged particles inside the body with temperature greater than 0 K [2]. Maxwell's equations provide a rigorous mathematical modelling that fully can describe the generation and propagation of electromagnetic waves with given boundary conditions. A fluctuating current due to the thermal fluctuations of the volume densities of charges and current is added in Ampere's law to represent the source of generated electromagnetic fields, which is at local equilibrium [32]. The electromagnetic fields at any point other than the source point are the superposition of the generated electromagnetic fields from the emitting objects. Following this logic, FE is also applicable to calculate local nonthermal radiation, which will be discussed in Chapter 6.

Maxwell's equation of non-magnetic materials can be written as:

$$\nabla \times \mathbf{E}(\mathbf{r},\omega) = \mathrm{i}\omega\mu_0 \mathbf{H}(\mathbf{r},\omega) \tag{2.1}$$

$$\nabla \times \mathbf{H}(\mathbf{r},\omega) = -\mathrm{i}\omega\varepsilon \mathbf{E}(\mathbf{r},\omega) + \mathbf{J}(\mathbf{r},\omega) \tag{2.2}$$

$$\nabla \cdot \mathbf{D}(\mathbf{r},\omega) = \rho_e \tag{2.3}$$

$$\nabla \cdot \mathbf{B}(\mathbf{r},\omega) = 0 \tag{2.4}$$

where **E**, **H**, **D**, and **B** represent the electric field, the magnetic field, the electric displacement current, and the magnetic induction at a random location **r** in a cylindrical coordinate for a specific frequency ω, respectively. ε is the electric permittivity, ρ_e is the

charge density, and μ_0 is the magnetic permeability of vacuum. By the employment of Lorentz gauge and the Green's function of a point impulse response of the system, the electric and magnetic fields can be written in terms of the volumetric integration of the Green's function as follows [2, 32]:

$$\mathbf{E}(\mathbf{r},\omega) = i\omega\mu_0 \int_{\mathrm{V}} \mathbf{G}^{E}(\mathbf{r},\mathbf{r}',\omega)\mathbf{J}(\mathbf{r}',\omega)d\mathbf{r}' \tag{2.5}$$

$$\mathbf{H}(\mathbf{r},\omega) = \int_{\mathrm{V}} \nabla\times\mathbf{G}^{H}(\mathbf{r},\mathbf{r}',\omega)\mathbf{J}(\mathbf{r}',\omega)d\mathbf{r}' \tag{2.6}$$

where $\mathbf{J}(\mathbf{r}',\omega)$ is the fluctuating current density corresponding to the frequency ω at the location $\mathbf{r}'$, and $\mathbf{r}$ is a random location in a cylindrical coordinate. $\mathbf{G}^{E}$ and $\mathbf{G}^{H}$ are the electric and magnetic Green's function, respectively. Applying the Poynting theorem, the heat flux can be represented by the time average of spectral Poynting vector in Cartesian coordinates:

$$q(\mathbf{r},\omega) = \left\langle \mathbf{S}(\mathbf{r},\omega)\right\rangle = 4\times\frac{1}{2}\mathrm{Re}\left\{\left\langle \mathbf{E}\times\mathbf{H}^{*}\right\rangle\right\} \tag{2.7}$$

To be noted, the factor 4 represents only the positive frequencies are accounted for in the Fourier transfer from the time space to frequency space. When one plugs Eqs. (2.5) and (2.6) into Eq. (2.7), the spatial correlation function of the fluctuating current density for a non-magnetic medium is given by fluctuation-dissipation theorem [28]:

$$\left\langle J_a(\mathbf{r}',\omega)J_b^{*}(\mathbf{r}'',\omega)\right\rangle = \frac{\omega\varepsilon_0\,\mathrm{Im}(\varepsilon)\Theta(\omega,T)\delta(\mathbf{r}'-\mathbf{r}'')\delta(\omega-\omega')\delta_{ab}}{\pi} \tag{2.8}$$

where $\langle\,\rangle$ and * denote the ensemble average and the complex conjugate. ε_0 represents the electric permittivity of vacuum. J_a or J_b $(a,b = x,y,z)$ stands for the x, y, z component of $\mathbf{J}$, δ_{ab} is the Kronecher delta function, and $\delta(\mathbf{r}'-\mathbf{r}'')$ is the Dirac delta function.

$\delta(\omega-\omega')$ represents the fluctuating current is spectral stationary. $\Theta(\omega,T)$ is the mean energy of a Planck's oscillator, which is defined as:

$$\Theta(\omega,T)=\hbar\omega\cdot\psi(\omega,T) \tag{2.9}$$

where $\psi(\omega,T)$ is the Bose-Einstein distribution To include the effect of photon chemical potential μ, the modified Bose-Einstein distribution, Ψ, is given as:

$$\Psi(\omega,T,\mu)=\begin{cases}\left[\exp\left(\dfrac{\hbar\omega}{k_{\mathrm{B}}T}\right)-1\right]^{-1}, & \omega<\omega_{\mathrm{g}}\\ \left[\exp\left(\dfrac{\hbar\omega-\mu}{k_{\mathrm{B}}T}\right)-1\right]^{-1}, & \omega\geq\omega_{\mathrm{g}}\end{cases} \tag{2.10}$$

where $\hbar$ is the reduced Planck constant, k_{B} is the Boltzmann constant and T is the temperature at local equilibrium. $\omega_{\mathrm{g}}=E_{\mathrm{g}}/\hbar$ is the frequency corresponding to the bandgap energy (E_{g}).

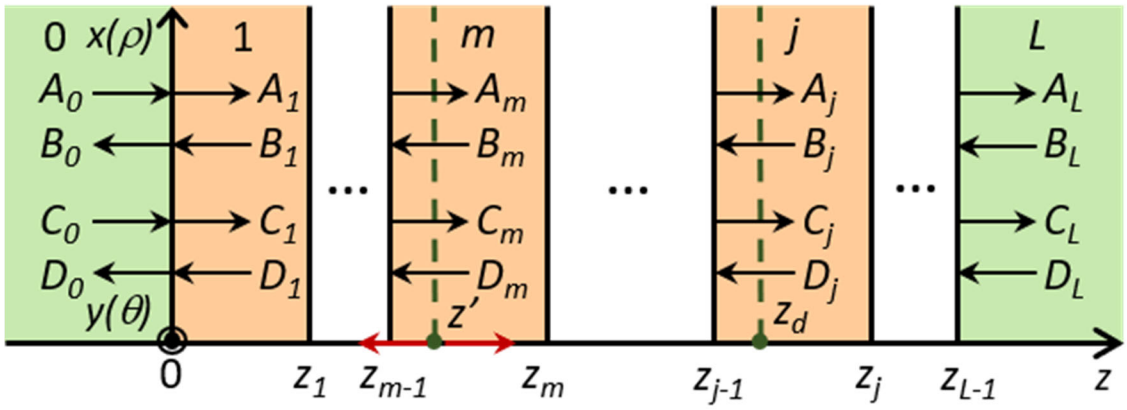

Figure 2.1 Schematic of one-dimensional stratified medium with the amplitude pattern of electric and magnetic field shown in each layer due to a point source z' located in layer *m*, and z_{d} is the detected point in a random layer *j* where the heat flux is calculated.

2.1.2 Dyadic Green's Function for an Isotropic Stratified Media

The one-dimensional (1D) stratified medium shown in Figure 2.1 represents the general geometric structure of a radiative energy converters. There are *L*-1 layers with finite thicknesses sandwiched between two semi-infinite bulks, which are usually air or substrate. Each layer can possess different optical and electrical properties at different local equilibrium. The temperature and photon chemical potential of a single layer are assumed to be constant. Therefore, to describe a stratified medium with varying spatial profile of equilibrium conditions, a finer mesh is required to make sure each layer at local equilibrium. The switch between Cartesian (x, y, z) and polar (ρ, θ, z) coordinate systems are required to calculate the electromagnetic field in every layer. By applying a spatial Fourier transform on the Green's function, the z-component spectral radiative heat flux of at z_d from the source point z' can be written as [32]:

$$\begin{aligned} q_{mj}\left(z_{\mathrm{d}},\omega\right) = & \left(\frac{\omega}{c\pi}\right)^2 \hbar\omega\Psi\left(\omega,T,\mu\right) \\ & \times \mathrm{Re}\left[i\mathrm{Im}\left(\varepsilon_m\right)\int_0^{\infty} k_{\|}dk_{\|}\int_z F_{mj}\left(\omega,k_{\|},z',z_{\mathrm{d}}\right)dz \right] \end{aligned} \tag{2.11}$$

where c is the speed of light in vacuum, $i=\sqrt{-1}$, ε_m is the relative permittivity of layer m, where the source point z' is located. $k_{\|}=\sqrt{k_x^2+k_y^2}$ is the parallel wavevector component. The function F_{mj} is essentially the z-component of the product of the electric dyadic Green's tensor and the conjugated magnetic dyadic Green's tensor, which are expressed as:

$$F_{mj}\left(\omega,k_{\|},z',z_{\mathrm{d}}\right)=\left[\mathbf{g}_{mj}^{E}\left(\omega,k_{\|},z',z_{\mathrm{d}}\right)\mathbf{g}_{mj}^{H*}\left(\omega,k_{\|},z',z_{\mathrm{d}}\right)\right]_{zz} \tag{2.12}$$

By substitution of the Weyl development of the dyadic Green's function, the electric dyadic Green's tensor is given as:

$$\mathbf{g}_{mj}^{E}\left(\omega,k_{\|},z',z_{\mathrm{d}}\right)=\frac{i}{2k_{zm}}\begin{bmatrix}\left(A_j^{TE}\hat{\mathbf{s}}\hat{\mathbf{s}}+A_j^{TM}\hat{\mathbf{p}}_j^{+}\hat{\mathbf{p}}_m^{+}\right)e^{i\left[k_{zj}\left(z_d-z_{j-1}\right)-k_{zm}z'\right]}\\+\left(B_j^{TE}\hat{\mathbf{s}}\hat{\mathbf{s}}+B_j^{TM}\hat{\mathbf{p}}_j^{-}\hat{\mathbf{p}}_m^{+}\right)e^{i\left[-k_{zj}\left(z_d-z_{j-1}\right)-k_{zm}z'\right]}\\+\left(C_j^{TE}\hat{\mathbf{s}}\hat{\mathbf{s}}+C_j^{TM}\hat{\mathbf{p}}_j^{+}\hat{\mathbf{p}}_m^{-}\right)e^{i\left[k_{zj}\left(z_d-z_{j-1}\right)+k_{zm}z'\right]}\\+\left(D_j^{TE}\hat{\mathbf{s}}\hat{\mathbf{s}}+D_j^{TM}\hat{\mathbf{p}}_j^{-}\hat{\mathbf{p}}_m^{-}\right)e^{i\left[-k_{zj}\left(z_d-z_{j-1}\right)+k_{zm}z'\right]}\end{bmatrix} \tag{2.13}$$

Similarly, the magnetic dyadic Green's tensor can be written as:

$$\mathbf{g}_{mj}^{H}\left(\omega,k_{\|},z',z_{\mathrm{d}}\right)=\frac{k_j}{2k_{zm}}\begin{bmatrix}\left(A_j^{TE}\hat{\mathbf{p}}_j^{+}\hat{\mathbf{s}}-A_j^{TM}\hat{\mathbf{s}}\hat{\mathbf{p}}_m^{+}\right)e^{i\left[k_{zj}\left(z_d-z_{j-1}\right)-k_{zm}z'\right]}\\+\left(B_j^{TE}\hat{\mathbf{p}}_j^{-}\hat{\mathbf{s}}-B_j^{TM}\hat{\mathbf{s}}\hat{\mathbf{p}}_m^{+}\right)e^{i\left[-k_{zj}\left(z_d-z_{j-1}\right)-k_{zm}z'\right]}\\+\left(C_j^{TE}\hat{\mathbf{p}}_j^{+}\hat{\mathbf{s}}-C_j^{TM}\hat{\mathbf{s}}\hat{\mathbf{p}}_m^{-}\right)e^{i\left[k_{zj}\left(z_d-z_{j-1}\right)+k_{zm}z'\right]}\\+\left(D_j^{TE}\hat{\mathbf{p}}_j^{-}\hat{\mathbf{s}}-D_j^{TM}\hat{\mathbf{s}}\hat{\mathbf{p}}_m^{-}\right)e^{i\left[-k_{zj}\left(z_d-z_{j-1}\right)+k_{zm}z'\right]}\end{bmatrix} \tag{2.14}$$

where the unit vector for transverse electric (TE) and transverse magnetic (TM) are respectively defined as:

$$\hat{\mathbf{p}}_j^{\pm}=\left(k_{\|}\hat{\mathbf{z}}\mp k_{zj}\hat{\boldsymbol{\rho}}\right)\Big/k_j \tag{2.15}$$

$$\hat{\mathbf{s}}=-\hat{\boldsymbol{\theta}} \tag{2.16}$$

where $\hat{\boldsymbol{\rho}}$, $\hat{\boldsymbol{\theta}}$, and $\hat{\mathbf{z}}$ are the unit vector in the polar coordinate system. k_{zj} is the *z*-component wavevector in layer *j* and $k_j=\sqrt{\varepsilon_j}\,\omega/c$. *A* and *B* denote the amplitudes of forward and backward waves due to a forward emitting wave from the source point z', and *C* and *D* denote the amplitudes of forward and backward waves due to a backward emitting wave from the same source point, which are shown in Figure 2.1. The superscript TE and

TM represent two different polarizations. The calculation of these amplitude coefficient requires recursive transfer method, which will be discussed in the next section.

2.1.3 Recursive Transfer Matrix Method

The continuity of parallel components of the electromagnetic waves at the layer interface is the key to determine the amplitude coefficients *A*, *B*, *C*, and *D*. Transfer matrix method is an efficient and conventional way to calculate these coefficients. However, due to numerical instabilities, Auslender and Hava [159] modified the transfer matrix method and proposed an improved method, called scattering matrix method, which is applied to near-field thermal radiation by Drevillon [160]. Francoeur et al. [33] gave detailed comparisons between transfer matrix method and scattering matrix method, where the potential limitation is also discussed in this work. A similar method proposed by Kovacs [161] solved the amplitude coefficients without using a matrix form, which could get rid of the singularity warning when inversing the matrix. The relation of the amplitude coefficient *A* between the incident waves and another random layer is written as follows:

$$\frac{A_L}{A_{L-1}} = t_{L-1,L} \exp\left(ik_{z,L-1}\Delta z_{L-1}\right) \tag{2.17}$$

$$\frac{A_{j+1}}{A_j} = \frac{t_{j,j+1} \exp\left(ik_{zj}\Delta z_j\right)}{1 + r_{j,j+1} r_{j+1,l} \exp\left(ik_{z,j+1}\Delta z_{j+1}\right)} \tag{2.18}$$

$$\frac{A_1}{A_0} = \frac{t_{01}}{1 + r_{01} r_{1L} \exp\left(2ik_{z1}\Delta z_1\right)} \tag{2.19}$$

where $\Delta z_j = z_j - z_{j-1}$. The Fresnel reflection coefficient between a random layer and the bottom layer is expressed as:

$$r_{jL} = \frac{r_{j,L-1} + r_{L-1,L} \exp\left(2ik_{z,L-1}\Delta z_{L-1}\right)}{1 + r_{j,L-1} r_{L-1,L} \exp\left(2ik_{z,L-1}\Delta z_{L-1}\right)} \tag{2.20}$$

The relation of the amplitude coefficients between the forward waves and backward wave is given by $B_j / A_j = r_{jL} \exp\left(2ik_{zj}\Delta z_j\right)$ and $B_0 / A_0 = r_{0L}$. Same relation could also be applied to calculate the amplitude coefficients *C* and *D* for the backward waves.

2.1.4 Near-field Radiative Heat Transfer between Two Semi-Infinite Bulks

A typical near-field geometric structure is two semi-infinite bulks separated by a vacuum gap with a distance of *d*, which is shown in Figure 2.2. The temperatures of the two semi-infinite bulks are T_1 and T_2, respectively. The photon chemical potential emitted by medium 1 and medium 2 are also assigned as μ_1 and μ_1, respectively. By simplifying Eq. (2.11), the net heat flux in z direction between medium 1 and medium 2 can be written as [2, 162]:

$$\begin{aligned} q_{12} = {} & \frac{1}{4\pi^2} \int_0^\infty \left[\Psi\left(\omega, T_1, \mu_1\right) - \Psi\left(\omega, T_2, \mu_2\right)\right] \hbar\omega d\omega \\ & \times \int_0^\infty \sum_{j=s,p} \xi_j\left(\omega, k_{\|}\right) k_{\|} dk_{\|} \end{aligned} \tag{2.21}$$

where ξ_j is the energy transmission coefficient for each polarization, which can be calculated by [2, 162]:

$$\xi\left(\omega, k_{\|}\right) = \begin{cases} \mathrm{Tr}\left[\left(\mathbf{I} - \mathbf{R}_2^* \mathbf{R}_2\right) \mathbf{M} \left(\mathbf{I} - \mathbf{R}_1 \mathbf{R}_1^*\right) \mathbf{M}^*\right], & k_{\|} < k_0 \\ \mathrm{Tr}\left[\left(\mathbf{R}_2^* - \mathbf{R}_2\right) \mathbf{M} \left(\mathbf{R}_1 - \mathbf{R}_1^*\right) \mathbf{M}^*\right] e^{-2|k_{z0}|d}, & k_{\|} > k_0 \end{cases} \tag{2.22}$$

where $k_0 = \omega/c$ is the wavevector in vacuum and $k_0 = \sqrt{k_0^2 - k_{||}^2}$ is the z-component wavevector in vacuum. Note that the symbol * represents the Hermitian transpose and Tr stands for trace operation. The Fresnel's reflection coefficients matrix is written as:

$$\mathbf{R}_{(1,2)} = \begin{bmatrix} r_{ss}^{(1,2)} & r_{sp}^{(1,2)} \\ r_{ps}^{(1,2)} & r_{pp}^{(1,2)} \end{bmatrix} \tag{2.23}$$

The matrix **M** is defined as:

$$\mathbf{M} = \left(\mathbf{I} - \mathbf{R}_1 \mathbf{R}_2 e^{2ik_{z_0} d} \right)^{-1} \tag{2.24}$$

where "-1" represent the inverse matrix operation. For an isotropic or a uniaxial anisotropic material, $r_{sp} = r_{ps} = 0$. The calculation of the transmission coefficients and Fresnel coefficients for isotropic and uniaxial anisotropic materials will be exhibited in each Chapter.

2.1.5 Local Photogeneration Rate and Absorbed Power

The introduced multilayer FE formalism can be applied to calculate photon exchange between any two layers in this 1D stratified medium. Dividing the radiative heat flux by the energy carried by single photon, the photo flux can be determined using Eq. (2.11). Therefore, the net photogeneration per unit area in layer *j* for a radiative energy converter with a 1D mesh can be expressed as:

$$G_j = \sum_{m=0}^{L} \int_{\omega_g}^{\infty} \left[\Psi\left(\omega, T_m, \mu_m\right) - \Psi\left(\omega, T_j, \mu_j\right) \right] \Upsilon_{mj}\left(\omega\right) d\omega \tag{2.25}$$

The function Υ_{mj} is the fraction of photons emitted at a given frequency from source layer *m* that is absorbed by layer *j* and vice versa. It can be calculated by subtracting the outgoing photons from the incoming photons.

$$\Upsilon_{mj}(\omega)=\left(\frac{\omega}{c\pi}\right)^2 \mathrm{Re}\left\{i\,\mathrm{Im}\left(\varepsilon_m\right)\int_0^\infty k_{\|}dk_{\|} \times\int_{z_{m-1}}^{z_m}\left[F(\omega,k_{\|},z,z_{j-1})-F(\omega,k_{\|},z,z_j)\right]dz\right\} \tag{2.26}$$

Eq. (2.10) gives the general expression of the *F* unction. However, a simplified formulation can be found in Ref. [33, 79]. Note that Υ depends on the vacuum gap distance *d*, and is reciprocal, i.e., $\Upsilon_{mj}=\Upsilon_{jm}$.

The rate of the net absorbed energy per unit area of the cell from the emitter (i.e., net heat flux) is calculated from [2]

$$Q=\sum_{m}^{emitter}\sum_{j}^{diode}\int_0^\infty \hbar\omega\left[\Psi\left(\omega,T_m,\mu_m\right)-\Psi\left(\omega,T_j,\mu_j\right)\right]\Upsilon_{mj}(\omega)d\omega \tag{2.27}$$

2.2 Charge Transport within Radiative Energy Converters

2.2.1 Drift-Diffusion Model

Electrons and holes are the two types of charge carriers moving inside a semiconductor device. The conservation of charge number is prescribed by the continuity equations for electrons and holes expressed as [163, 164]

$$\frac{\partial n}{\partial \mathrm{t}}=\frac{1}{e}\nabla\cdot J_{\mathrm{e}}+g-r_{\mathrm{b}} \tag{2.28}$$

$$\frac{\partial p}{\partial \mathrm{t}}=-\frac{1}{e}\nabla\cdot J_{\mathrm{h}}+g-r_{\mathrm{b}} \tag{2.29}$$

where n and p are the electron and hole concentrations, which are functions of time and space, e is the elementary charge, g is the net generation rate that is obtained by $G_j / \Delta z_j$ in a given layer j, and r_{b} is the (bulk) nonradiative recombination rate, which is the sum of the Auger recombination rate and the Shockley-Read-Hall (SRH) recombination rate, expressed respectively in the following [163, 165] :

$$r_{\mathrm{Auger}} = \left(C_{\mathrm{e}} n + C_{\mathrm{h}} p\right)(np - n_{\mathrm{i}}^2) \tag{2.30}$$

and

$$r_{\mathrm{SRH}} = \frac{np - n_{\mathrm{i}}^2}{\tau_{\mathrm{h}}(n + n_{\mathrm{t,b}}) + \tau_{\mathrm{e}}(p + p_{\mathrm{t,b}})} \tag{2.31}$$

In Eqs. (2.30) and (2.31), C_{e} and C_{h} are the Auger recombination coefficients for electrons and holes, n_{i} is the intrinsic carrier concentration, τ_{e} and τ_{h} are the bulk lifetimes for electrons and holes, respectively, $n_{\mathrm{t,b}}$ and $p_{\mathrm{t,b}}$ are the electron and hole trap concentrations that are set to be the same as the n_{i} in the modeling.

The charge current densities, J_{e} and J_{h}, are modeled in terms of drift and diffusion forces as follows

$$J_{\mathrm{e}} = -e\upsilon_{\mathrm{e}} n \nabla\varphi + eD_{\mathrm{e}} \nabla n \tag{2.32}$$

$$J_{\mathrm{h}} = -e\upsilon_{\mathrm{h}} p \nabla\varphi + eD_{\mathrm{h}} \nabla p \tag{2.33}$$

where υ_{e} and υ_{h} are the mobility of electrons and holes, respectively, and D_{e} and D_{h} are the diffusion coefficients, which are related to mobility according to Einstein's relation $D = \upsilon k_{\mathrm{B}} T / e$ for each type of carrier. In Eqs. (2.32) and (2.33), φ is the electrostatic potential, which obeys Poisson's equation:

$$\nabla \cdot \left(\varepsilon \nabla \varphi \right) = \left(e / \varepsilon_0 \right) \left(N_{\mathrm{A}} - N_{\mathrm{D}} + n - p \right) \tag{2.34}$$

where ε is the dielectric constant of the cell material, ε_0 is the vacuum permittivity, and N_{A} and N_{D} are the acceptor and donor concentrations, respectively.

Substituting Eqs. (2.25) and (2.30) through (2.33), into the three governing equations (2.28), (2.29) and (2.34) for prescribed conditions gives three differential equations in terms of the three unknown variables *n*, *p*, and φ. Obtaining stable and converging solutions is not a trivial task especially with high injection [80]. Here, a finite-difference method applying the Scharfetter-Gummel discretization scheme is used to solve the transient charge transport model with given boundary conditions and the initial guess obtained under the equilibrium condition [165-167]. This transient time-marching scheme allows the steady-state solutions to be obtained with relatively higher converging speed than directly solving the steady-state problem. This model considers both the majority and minority carrier concentrations, which provide detailed information beyond the depletion approximation typically used to determine the minority carrier concentrations in modeling PV and TPV devices [75, 76, 78, 91, 112, 168].

Boundary conditions for both sides of a *p-n* diode are required to solve the carrier transport equations. For a semiconductor device, the interface between semiconductor and metal is the most complicated part to model, which depends on material properties and operating conditions [169]. Surface passivation and selective contacts have often been used to boost the performance [170, 171]. Ohmic contact is assumed and simplified boundary conditions are used to describe the surface recombination[163, 169, 172]:

$$J_{\mathrm{e}}(z_{\mathrm{t}}) = eS_{\mathrm{e},p}\left[n(z_{\mathrm{t}}) - n_0(z_{\mathrm{t}})\right] \tag{2.35}$$

$$J_{\mathrm{h}}(z_{\mathrm{t}}) = -eS_{\mathrm{h},p}\left[p(z_{\mathrm{t}}) - p_0(z_{\mathrm{t}})\right] \tag{2.36}$$

$$J_{\mathrm{e}}(z_{\mathrm{b}}) = -eS_{\mathrm{e},n}\left[n(z_{\mathrm{b}}) - n_0(z_{\mathrm{b}})\right] \tag{2.37}$$

$$J_{\mathrm{h}}(z_{\mathrm{b}}) = eS_{\mathrm{h},n}\left[p(z_{\mathrm{b}}) - p_0(z_{\mathrm{b}})\right] \tag{2.38}$$

where $S_{\mathrm{e},p}$, $S_{\mathrm{h},p}$, $S_{\mathrm{e},n}$, and $S_{\mathrm{h},n}$ are the surface recombination velocities for electrons and holes in the *p* and *n* regions, respectively, and n_0 and p_0 are the carrier concentrations at equilibrium. Note that n_0 and p_0 are related to the intrinsic carrier concentrations and the acceptor concentrations (in the *p*-region) or the donor concentrations (in the *n*-region). z_{t} and z_{b} represents the location at the top surface of *p*-region and bottom surface of *n*-region.

The obtained electron or hole concentration is related to electron or hole quasi-Fermi levels ($E_{\mathrm{f,e}}$ or $E_{\mathrm{f,h}}$) using the Boltzmann approximation:

$$n = n_{\mathrm{i}} \exp\left(\frac{E_{\mathrm{f,e}} - E_{\mathrm{i}}}{k_{\mathrm{B}}T}\right) \tag{2.39}$$

or

$$p = n_{\mathrm{i}} \exp\left(\frac{E_{\mathrm{i}} - E_{\mathrm{f,h}}}{k_{\mathrm{B}}T}\right) \tag{2.40}$$

where E_{i} is the intrinsic Fermi energy. The quasi-Fermi levels obtained from Eqs. (2.39) and (2.40) are used to calculate photon chemical potential,

$$\mu(z) = E_{\mathrm{f,e}}(z) - E_{\mathrm{f,h}}(z),\ z_t \le z \le z_b \tag{2.41}$$

The voltage-dependent power per unit area and conversion efficiency are given by

$$P(V) = J(V)V \tag{2.42}$$

and

$$\eta(V) = P(V) / Q(V) \tag{2.43}$$

The net heat flux Q depends on the photon chemical potential profile which, in turn, is a function of the bias voltage.

2.2.2 Detailed Balance Analysis

Detailed balance analysis was first applied by Shockley and Queisser to calculate the theoretical efficiency limit of a solar cell, which is also called Shockley-Queisser limit [173]. Same approaches can be transplanted to evaluate the performance of radiative energy converters, since they share the same mechanism of energy conversion. Two major assumptions are the key to implement the detailed balance analysis: the mobility of the free carriers inside the p-n diode is infinite; the intrinsic internal quantum efficiency is 100%, which means the complete photogeneration of all photons above the bandgap energy. In this way, the radiative energy converter is treated as a homogenous bulk without considering the spatial variation of optical and electrical processes. Therefore, the current density generated by the *p-n* diode is calculated as

$$J = e\left(G_{pn} - R_{pn}\right) \tag{2.44}$$

Here, G_{pn} is the net photogeneration rate in the active region per unit area and is calculated by the summation of every layer of the *p-n* diode:

$$G_{pn} = \sum_{diode} G_j \tag{2.45}$$

In Eq. (2.44), R_{pn} is the recombination rate per unit area that includes both bulk and surface recombination according to

$$R_{pn} = \left(r_{\text{Auger},p} + r_{\text{SRH},p}\right) d_p + R_{\text{s},p} + \left(r_{\text{Auger},n} + r_{\text{SRH},n}\right) d_n + R_{\text{s},n} \tag{2.46}$$

where d_p and d_n is the thickness of p- and n-region. In the detailed balance analysis, it is assumed that $p = p_0 + \Delta$ and $n = n_0 + \Delta$, where Δ depends on the bias voltage and temperature according to [163, 173]:

$$pn = p_0 n_0 \exp(Ve / k_{\text{B}} T) \tag{2.47}$$

Equation (2.45) can be solved to obtain p and n either in the p-region or the n-region of the p-n diode, and then used to compute the bulk recombination rates from Eqs. (2.30) and (2.31).

The surface recombination rates per unit area are given as [163, 165]

$$R_{\text{s},p} = \frac{np - n_{\text{i}}^2}{(n + n_{\text{t,s}}) / S_{\text{h},p} + (p + p_{\text{t,s}}) / S_{\text{e},p}} \tag{2.48}$$

$$R_{\text{s},n} = \frac{np - n_{\text{i}}^2}{(n + n_{\text{t,s}}) / S_{\text{h},n} + (p + p_{\text{t,s}}) / S_{\text{e},n}} \tag{2.49}$$

In the modeling, the surface trap concentrations are assumed to be the same as the intrinsic carrier concentration, i.e., $n_{\text{t,s}} = p_{\text{t,s}} = n_{\text{i}}$. The surface recombination velocities are the same as those used in the iterative model.

Substituting Eq. (2.44) into Eq. (2.42) gives the power generation per unit area, which is a function of the bias voltage. Then Eq. (2.43) is used to calculate the efficiency in the detailed balance analysis. However, in applying Eq. (2.25) to calculate the net photogeneration rate and Eq. (2.27) for the net absorbed energy rate, one may set the photon chemical potential either as a constant ($\mu = Ve$) to approximate the luminescence effect or

as zero ($\mu = 0$) to ignore the luminescence effect. In the detailed balance analysis, the photon transport and charge transport equations are decoupled and, therefore, they can be independently solved. In the Chapter 4, these two scenarios ($\mu = Ve$ and $\mu = 0$) are used to compare with the solutions obtained from the iterative method in order to demonstrate the importance of considering the photon chemical potential as well as its spatial variation.

CHAPTER 3. NEAR-FIELD EFFECT ON THE DARK CURRENT OF THERMOPHOTOVOLTAIC CELLS

This Chapter quantitatively analyze how near-field radiation affects the *J-V* characteristics of TPV cells. The difference between near-field dark current and far-field dark current highlights that near-field effects on the saturation current may lead to changes in diode parameters including dark current and open-circuit voltage. In the end, these effects can alter the modeling prediction of the output electric power and efficiency. It should also be noted that near-field radiative heat transfer calculations used in the standard method do not include the photon chemical potential and therefore may cause substantial error when the emitter is operated at relatively low temperatures. The theory and methodology in the previously mentioned modeling methods are overviewed with an emphasis on the modified direct method (MDM) algorithm and applicability. An ideal case with a blackbody emitter and cell is used to show the dependence of saturation current on the energy gap and temperature based on radiative recombination. The enhancement effect of evanescent waves on the saturation current for selected cells is then illustrated. The *J-V* curves for several TPV cells are plotted for various separation distances to further demonstrate the near-field effects. The error in the standard method without considering the distance dependent saturation current and chemical potential of photons is quantified based on a TPV device with a tungsten emitter and an $In_{0.18}Ga_{0.82}Sb$ cell. The limitations of the current modeling methods are also discussed with an aim to point out future work that is needed to model realistic TPV cell performance.

3.1 Modeling Methods of Near-Field TPV devices

For near-field TPV devices, different modeling approaches have been applied without examining their consistencies and discrepancies. Figure 3.1(a) shows a typical TPV device consisting of an emitter at a temperature of and a cell at a temperature, separated by a distance d. The conventional method or standard method to model near-field TPV operation is based on the Shockley diode theory for far-field PV cells [163, 173-175] and has been extensively applied in modeling near-field TPV devices [73-76]. This method assumes that the operating current, denoted as curve D in Figure 3.1(b), can be modeled as a superposition of the dark current (curve B) and the short-circuit photocurrent ($-J_{sc}$). Zenker et al. [175] employed the photon chemical potential concept proposed by Würfel [42] to directly calculate the photocurrent under illumination without decoupling the effects of bias and illumination. The photon chemical potential enables the calculation of the bias-dependent blackbody distribution according to modified Bose-Einstein statistics [5, 10, 123]. This method has also been applied in analyzing TPV and other radiative energy conversion devices [9, 10, 88, 89, 129, 176]. Typically, the standard method uses a constant saturation current in the Shockley diode equation that does not depend on the separation distance between the emitter and cell, thereby assuming evanescent waves do not affect dark current. While the direct method makes no such assumption, neither the dark current nor other significant diode parameters are explicitly defined. Recently, Lin et al. [123, 177] analyzed an ideal photoconverter by making a connection between the standard method and the direct method in both the near- and far-field regimes. We call this method the modified direct method, since it can be derived from the direct method using Wien's approximation. The use of the MDM allows the assessment of the standard method

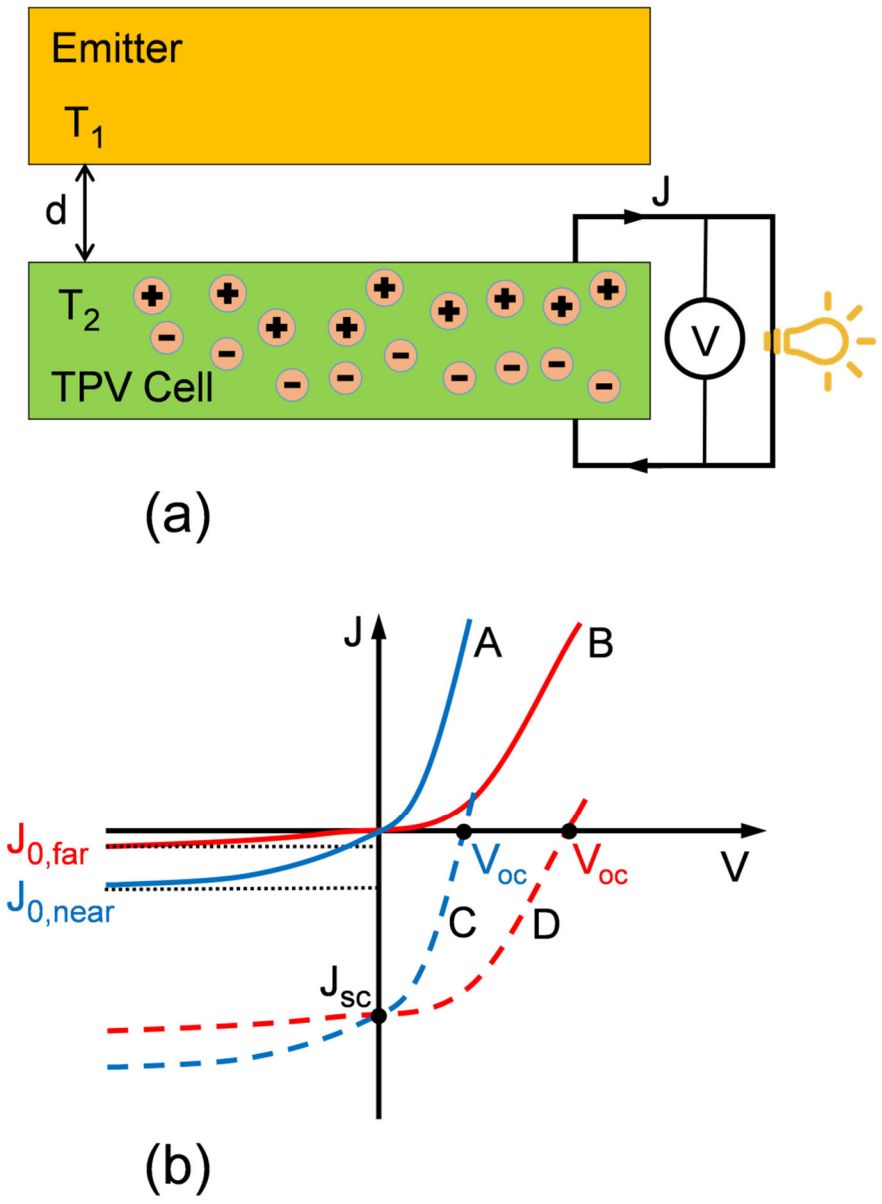

Figure 3.1(a) Schematic of a near-field TPV device, where the emitter and cell are assumed to be semi-infinite in the modeling, separated by a vacuum gap of distance *d*. (b) Schematic of the current-voltage curves for a photodiode (TPV cell) in four cases: (A) far-field in dark conditions ($T_1 = T_2 = T$), (B) near-field in dark conditions, (C) near-field under illumination, (D) near-field under illumination obtained from the standard method using the far-field saturation current.

commonly used in analyzing near-field TPV devices. As shown in Figure 3.1(b), if the near-field effect is considered, the saturation current must be treated as a function of the separation distance that modifies the dark current curve from B to A as d is changed from the far field to the near field. Subsequently, the *J-V* curve is shifted from D to C and the open-circuit voltage is reduced.

An overview of the standard method and the direct method is given in this section. Then the MDM based on Lin et al. [123, 177] is introduced and assessed in its applicable range. This allows a connection between the standard method and direct method for modeling ideal photoconverters. The drawbacks in the standard method typically used in modeling TPV cells are indicated.

3.1.1 Standard Method

For simplicity and to better contrast different modeling methods, we assume the TPV cell acts as an ideal photoconverter as defined in Ref. [163], which requires several assumptions: (a) the bulk material has an energy gap which separates states which are normally full from states which are normally empty; (b) all incident photons with energy larger than the bandgap are absorbed and generate exactly one electron-hole pair per photon; (c) only radiative recombination is considered; and (d) charge transport losses are negligible.

Based on the principle of detailed balance [173], it can be shown that the photocurrent is a summation of the short-circuit current ($-J_{sc}$) and the dark current J_{dark}, as shown in Figure 3.1(b) with J_{sc} being the absolute value. Note that presented herein, the currents (J) are actually current densities, normalized per unit area. A photovoltaic cell operates in the regime $0 < V < V_{oc}$, where V_{oc} is the open-circuit voltage. To analyze the

photodiode performance, it is common to express the *J-V* characteristics in the first quadrant of the *J-V* plot (using the magnitude of the photocurrent) as follows [163, 173, 174]:

$$J(V) = J_{\text{sc}} - J_{\text{dark}}(V) \tag{3.1}$$

The dark current is the current that flows through the cell as a function of voltage V in the absence of illumination when the emitter and cell are at the same temperature, as shown in Figure 3.1(b). Most photovoltaic cells have a diode-like behavior as described by the Shockley diode equation [173, 174],

$$J_{\text{dark}}(V) = J_0\left[\exp\left(\frac{eV}{k_{\text{B}}T}\right) - 1\right] \tag{3.2}$$

where J_0 is a positive quantity called the (reverse) saturation current, which is typically assumed to depend only on material properties, e is the electron charge, k_{B} is the Boltzmann constant, and T is the temperature of the PV cell. The saturation current can be measured under a large negative bias in dark conditions. For real *p-n* diodes, J_0 includes contributions from the diffusion current $J_{0,\text{diff}}$ in the *p* and *n* regions, current in the depletion region (space charge region) $J_{0,\text{scr}}$, and radiative recombination current $J_{0,\text{rad}}$. Generally, for indirect gap materials like silicon, the diffusion of minority carriers dominates the dark current characteristics, allowing the saturation current to be approximated as [163, 174]

$$J_0 \approx J_{0,\text{diff}} = e\left(\frac{n_{\text{i}}^2}{N_{\text{A}}}\sqrt{\frac{D_{\text{e}}}{\tau_{\text{e}}}} + \frac{n_{\text{i}}^2}{N_{\text{D}}}\sqrt{\frac{D_{\text{h}}}{\tau_{\text{h}}}}\right) \tag{3.3}$$

where N_A, N_D, and n_i represent the concentrations of acceptors, donors, and intrinsic carriers, respectively, and $D_{e,h}$ and $\tau_{e,h}$ are the diffusion coefficient and relaxation time of electrons or holes in *p* or *n* regions, respectively. Equation (3.3) may be a proper approximation of the saturation current for a far-field TPV cell with a *p*-*n* junction structure. It has been applied for the analysis of near-field TPV devices by a number of researchers [73-76]. Nevertheless, the relation between the three components of saturation current is more complicated for a near-field TPV cell. In the scenario with an ideal photoconverter, only radiative recombination contributes to the dark current.

An ideal photodiode assumes 100% quantum efficiency signifying that every absorbed photon whose energy is above the bandgap will generate one electron-hole pair with perfect charge separation and deliver an electron to an external circuit [173]. In this case, the short-circuit photocurrent J_{sc} is the current through the circuit without an external load and is given by [74-76]

$$J_{sc} = \frac{e}{4\pi^2}\int_{\omega_g}^{\infty} k_0^2 \left[\psi(\omega, T_1) - \psi(\omega, T_2)\right] \Phi(\omega, \beta_{max}) d\omega \tag{3.4}$$

where $\omega_g = E_g / \hbar$ is the frequency corresponding to the bandgap energy E_g with $\hbar$ being the reduced Planck constant, $k_0 = \omega / c$ is the free space wavevector with *c* being the speed of light in vacuum, $\psi(\omega, T) = \left(e^{\hbar\omega / k_B T} - 1\right)^{-1}$ is the Bose-Einstein distribution, T_1 and T_2 denote the temperature of the source (or emitter) and the TPV cell, respectively, and Φ is the spectral transmission coefficient defined by

$$\Phi(\omega, \beta_{max}) = \frac{1}{k_0^2}\int_0^{\beta_{max}} \sum_{h=s,p} \xi_h(\omega, k_{||}) k_{||} dk_{||} \tag{3.5}$$

where ξ is the mode transmission coefficient or photon tunneling probability (in the case with evanescent waves) for a given polarization (*s* or *p*), $k_{||}^2 = k_x^2 + k_y^2$ is the parallel component of the wavevector, with the coordinate system shown in Figure 3.1(a), and $\beta_{\max}$ is the upper limit of integration. The transmission coefficient can be calculated using FE for given emitter and cell temperatures and dielectric functions [2, 22, 78, 178]. Equation (3.4) can be used to calculate the short-circuit current for both near- and far-field TPV operation. For the far-field case, only propagating waves should be included, which can be done by setting $\beta_{\max} = k_0$. In the near-field case, evanescent waves must be included so that $\beta_{\max} = \infty$. However, in practical calculations, an upper limit is often set in the numerical evaluation of the integral [179].

Under illumination, the TPV cell achieves the maximum potential difference when the circuit is cut off. This is called the open-circuit voltage, which is computed by setting $J(V_{\text{oc}}) = 0$ in Eq. (3.1) so that $J_{\text{sc}} = J_{\text{dark}}(V_{\text{oc}})$. By using Eq. (3.2), we have

$$V_{\text{oc}} = \frac{k_{\text{B}}T}{e} \ln\left(\frac{J_{\text{sc}}}{J_0} + 1\right) \tag{3.6}$$

The output electric power (per unit area) of the TPV cell is the product of the current and voltage of the load, which under an ideal situation is the same as the voltage across the *p*-*n* diode, as illustrated in Figure 3.1(a). It can be calculated by Eq. (2.42).

The net radiant power received by the TPV cell per unit area or net heat flux from the emitter to the receiver is calculated by [78, 178]

$$Q = \frac{1}{4\pi^2} \int_0^\infty k_0^2 \left[\Theta(\omega, T_1) - \Theta(\omega, T_2)\right] \Phi(\omega, \beta_{\max}) d\omega \tag{3.7}$$

Note that the radiative heat transfer includes photons at frequencies both higher and lower than the bandgap. For radiative heat transfer between two blackbodies, we have $\Phi(\omega, \beta_{\max}) = 1$, and Eq. (3.7) reduces to the conventional formula governed by the Stefan-Boltzmann law. The conversion efficiency of the TPV cell as a function of operating voltage can be calculated from Eq. (2.43), which can be optimized with matching load conditions to maximize the output power $P_{\max}$ or the conversion efficiency $\eta_{\max}$ at certain voltage [75, 123].

3.1.2 Direct Method

Unlike the standard method, the direct method does not separate the effects of bias and illumination into dark current and short-circuit photocurrent. By using the modified Bose-Einstein distribution to include the chemical potential of photons [1, 123], the direct method describes the photon exchange process under bias and illumination simultaneously. The typical Bose-Einstein distribution (without chemical potential) for emitted photons is only valid when the emitting material is at thermodynamic equilibrium. A TPV cell under bias, however, is in a non-equilibrium state. Würfel [1] analyzed this case by assigning the photon distribution a chemical potential μ, which is related to the difference in electron and hole chemical potentials or quasi-Fermi levels. In a TPV device, this chemical potential in the space charge region is given by $\mu = eV$. The emitted photons from a photodiode can be described by the modified Bose-Einstein distribution [5], which is already shown in Eq. (2.10). Similar to the short-circuit photocurrent calculation in the standard method, the general form of *J-V* characteristics for both near- and far-field TPV cells may be described using the modified Bose-Einstein distribution as follows [88, 176]:

$$J(V)=\frac{e}{4\pi^2}\int_{\omega_g}^{\infty}k_0^2\left[\Psi(\omega,T_1,0)-\Psi(\omega,T_2,\mu)\right]\Phi(\omega,\beta_{\max})d\omega \tag{3.8}$$

since only the photons from the TPV cell carry chemical potential $\mu = eV$. Note that a 100% internal quantum efficiency is assumed in the calculation. The net radiative heat transfer between the emitter and the cell must also be modified so that it depends on the chemical potential

$$Q(V)=\frac{1}{4\pi^2}\int_{0}^{\infty}k_0^2\hbar\omega\left[\Psi(\omega,T_1,0)-\Psi(\omega,T_2,\mu)\right]\Phi(\omega,\beta_{\max})d\omega \tag{3.9}$$

Equations (2.42) and (2.43) are still valid to calculate the output electric power and corresponding efficiency of TPV cells. Notice that Eq. (3.9) should be used as the denominator in the efficiency calculation since the net heat flux is a function of the bias voltage. Although the direct method makes no assumptions about the dark current behavior of the TPV cell, it also does not separately specified diode parameters such as saturation current and open-circuit voltage. This makes it difficult to clearly analyze the influence of operating conditions such as separation distance, bias, and temperatures of the cell and emitter.

3.1.3 Modified Direct Method (MDM)

The standard and direct methods may be connected through the use of Wien's approximation when describing the photon exchanges. This MDM provides a linkage between the standard method and the direct method. Wien's approximation was originally proposed to describe the complete spectrum of blackbody radiation, but it fails to give an accurate description of the distribution at low frequencies. Statistically, Wien's formula uses the Boltzmann distribution to approximate the Bose-Einstein distribution [2, 123].

When $\hbar\omega >> k_{\mathrm{B}}T_1$, we see that $\Psi(\omega, T_1, 0) \approx \exp\left(-\hbar\omega / k_{\mathrm{B}}T_1\right)$. Furthermore, when $(\hbar\omega - \mu) >> k_{\mathrm{B}}T$, we have

$$\Psi(\omega, T_2, \mu) \approx \exp\left(-\frac{\hbar\omega}{k_{\mathrm{B}}T_2}\right)\exp\left(\frac{\mu}{k_{\mathrm{B}}T_2}\right) \tag{3.10}$$

If Wien's approximation is applied to the direct method, Eq. (3.8) is reduced to [123, 177]

$$\begin{aligned} J(V) = {} & \frac{e}{4\pi^2}\int_{\omega_{\mathrm{g}}}^{\infty} k_0^2 \Phi(\omega, \infty)\left(\mathrm{e}^{-\hbar\omega/k_{\mathrm{B}}T_1} - \mathrm{e}^{-\hbar\omega/k_{\mathrm{B}}T_2}\right) d\omega \\ & - \frac{e}{4\pi^2}\left[\int_{\omega_{\mathrm{g}}}^{\infty} k_0^2 \Phi(\omega, \infty)\mathrm{e}^{-\hbar\omega/k_{\mathrm{B}}T_2} d\omega\right]\left(\mathrm{e}^{eV/k_{\mathrm{B}}T_2} - 1\right) \end{aligned} \tag{3.11}$$

The first term on the right-hand side is the short-circuit photocurrent J_{sc}, given in Eq. (3.4), under Wien's approximation. The second term on the right-hand side has the same form as Eq. (3.2), which is the dark current of the TPV cell, when the saturation current is dominated by the contribution from radiative recombination, i.e.,

$$J_0 \approx J_{0,\mathrm{rad}} = \frac{e}{4\pi^2}\int_{\omega_{\mathrm{g}}}^{\infty} k_0^2 \Phi(\omega, \infty)\mathrm{e}^{-\hbar\omega/k_{\mathrm{B}}T_2} d\omega \tag{3.12}$$

Subsequently, we can express the dark current given in Eq. (3.2) as follows:

$$J_{\mathrm{dark}}(V) = J_{0,\mathrm{rad}}\left[\exp\left(\frac{eV}{k_{\mathrm{B}}T_2}\right) - 1\right] \tag{3.13}$$

This is essentially the Shockley diode equation when radiative recombination dominates the saturation current rather than diffusion. Equations (3.11) to (3.13) suggest that the direct method and the standard method are related under Wien's approximation, as long as the saturation current is calculated according to Eq. (3.12). Shockley and Queisser [173] originally determined the corresponding dark current expression for a far-field photodiode using a similar formulation.

Before these approximations can be applied, it is important to understand their limitations. For $\hbar\omega = 3k_{\mathrm{B}}T_1$, the Boltzmann distribution yields approximately 5% error compared to the Bose-Einstein distribution. For further analysis, let us assume a maximum tolerance of 5% at $\omega = \omega_{\mathrm{g}}$ as the acceptable criterion. The resulting error after the integration is generally much smaller than 5%. For example, with an emitter at temperature $T_1 = 1000$ K, its thermal emission can be described with Wien's approximation within 5% error for photon energies higher than 0.26 eV. Since we are only interested in photons with energy higher than the bandgap for electricity generation, 0.26 eV corresponds to the minimum cell bandgap that can be analyzed with such an emitter. Similarly, if the cell temperature is T_2 = 300 K, the minimum value of $(\hbar\omega - \mu)$ that can be analyzed is about 0.08 eV, which will occur for the lowest $\hbar\omega$ (corresponding to the bandgap energy) and highest μ (corresponding to the open-circuit voltage). If we use a material with a bandgap of 0.26 eV, the corresponding open-circuit voltage should be lower than 0.18 V for 5% maximum error at V_{oc}. In general, it is safe to apply Wien's approximation for the situation of higher bandgap materials and lower temperatures of the TPV cell and emitter. Since the operating voltage is taken as the voltage corresponding to the maximum efficiency or output power, the resulting error in the MDM is usually negligibly small once the above criteria are satisfied.

It must be noted that, according to Eq. (3.12), the saturation current depends on the spectral transmission coefficient and hence is a function of separation distance, especially in the near-field regime. This is one of the main points of the present study. Notice that the net radiant power received by the cell should still be calculated with Eq. (3.9) without using Wien's approximation since the lower limit of the integration is at $\omega = 0$.

Next, we can use Eqs. (2.42) and (2.43) to compute the output power and efficiency, respectively. While the MDM is an approximation of the direct method, it allows the evaluation of the dark current in both the far- and near-field regimes and enables the study of the near-field effect on other diode performance parameters. For example, we can also derive an analytical expression of the open-circuit voltage based on the diode equation, Eq. (3.6), to obtain

$$V_{\mathrm{oc}} = \frac{k_{\mathrm{B}}T_2}{e} \ln\left(\frac{\int_{\omega_{\mathrm{g}}}^{\infty} k_0^2 e^{-\hbar\omega/k_{\mathrm{B}}T_1} \Phi(\omega,\infty)\, d\omega}{\int_{\omega_{\mathrm{g}}}^{\infty} k_0^2 e^{-\hbar\omega/k_{\mathrm{B}}T_2} \Phi(\omega,\infty)\, d\omega} \right) \tag{3.14}$$

In terms of the photocurrent calculation, the standard method and the MDM are essentially the same for an ideal photoconverter as long as the radiative recombination current is properly accounted for as a function of separation distance. However, this was not typically done in the standard method as mentioned previously, since the near-field effect on the saturation current has never been investigated. Furthermore, as to be discussed later, when the emitter temperature is not very high, Eq. (3.9) must be used to properly calculate the net heat flux. This has not been properly taken into consideration in the literature when applying the standard method.

3.2 Result Comparisons of Three Modeling Methods

A schematic of the TPV system under consideration is shown in Figure 3.1(a). The cell temperature is maintained at 300 K. Depending on the operating condition, the emitter temperature is either 1000 K for illumination or 300 K for dark conditions. A reference case of a blackbody emitter and blackbody cell is first used to show the relation between diode parameters and bandgap. Results for real materials are normalized to this reference

case in order to indicate the effect of evanescent waves on different diode parameters. The cell materials (with optical properties given in the corresponding references) examined are InAs [93] and $In_{0.18}Ga_{0.82}Sb$ [180, 181] for low direct bandgap cells and Si [181, 182] for a higher indirect bandgap cell. For the emitter material, we examine two different cases for each cell: an emitter made of tungsten [181] and an emitter made of the same material as the cell. For an ideal photoconverter, only the radiative recombination component exists in the saturation current, i.e., $J_0 = J_{0,\mathrm{rad}}$. In the following, the standard method refers to the case when $J_{0,\mathrm{rad}}$ is treated as a constant based on the far-field result and Q is calculated from Eq. (3.7) without considering photon chemical potential. On the other hand, the MDM treats $J_{0,\mathrm{rad}}$ as a function of separation distance based on Eq. (3.12), while Q is calculated from Eq. (3.9) which includes the effect of photon chemical potential of the cell. The effect of diffusion contributions and other non-idealities will be discussed near the end of this section.

3.2.1 A Reference Blackbody Case

A TPV device with a black emitter and cell is an idealized device that may serve as a reference case when we study the effect of evanescent waves on diode parameters. Using the MDM, the transmission coefficient is 1 for both s and p polarization $\xi_s = \xi_p = 1$ because both objects are treated as blackbodies. Furthermore, when the contributions of the two polarizations are included, we see that the spectral transmission coefficient $\Phi(\omega, k_0) \equiv 1$ by setting $\beta_{\max} = k_0$ in Eq. (3.7). After some lengthy derivations, we can show that the four diode parameters are expressed as follows:

$$J_{\mathrm{sc}} = \frac{e}{4\pi^2 c^2}\left[F(x_1) - F(x_2)\right] \tag{3.15}$$

$$J_{\mathrm{dark}}(V) = \frac{e}{4\pi^2 c^2} F(x_2)\left[\exp\left(\frac{eV}{k_{\mathrm{B}} T_2}\right) - 1\right] \tag{3.16}$$

$$J_0 = \frac{e}{4\pi^2 c^2} F(x_2) \tag{3.17}$$

and $$V_{\mathrm{oc}} = \frac{k_{\mathrm{B}} T_2}{e} \ln\left[\frac{F(x_1)}{F(x_2)}\right] \tag{3.18}$$

Here, $x_i = E_{\mathrm{g}} / k_{\mathrm{B}} T_i$, where i = 1 or 2 for the emitter or cell, respectively, and

$$F(x_i) = \left(\frac{k_{\mathrm{B}} T_i}{\hbar}\right)^3 \left(x_i^2 + 2x_i + 2\right) \mathrm{e}^{-x_i} \tag{3.19}$$

In this case, the saturation current is a function of cell material bandgap and cell temperature. It should be noted that the exponentially decaying trend, i.e., $J_0 \approx A(T) \exp\left(-E_g / k_{\mathrm{B}} T\right)$, has been theoretically obtained considering charge diffusion [174] and experimentally demonstrated for semiconductor photovoltaic cells [183]. The relation between the saturation current and the bandgap of the cell material is shown in Figure 3.2 for a cell temperature of 300 K. In the *y*-axis label, $J_{0\mathrm{b}}$ stands for saturation current due to radiative recombination between a blackbody emitter and cell. The exponential decrease of the saturation current as the bandgap increases is clearly shown. The saturation current can also be interpreted as the total emission due to radiative recombination under dark conditions without any bias. The vertical dashed lines indicate the bandgap energies for three semiconductors. Compared to a higher bandgap material like $In_{0.18}Ga_{0.82}Sb$ or Si, an InAs cell emits more photons above the bandgap because of its lower bandgap energy. Since the quantum efficiency is taken as 100%, these photons

represent more electron-hole pairs recombining and contributing to the saturation current. The reference values for blackbodies provided here will be used in normalizing the saturation current for real materials.

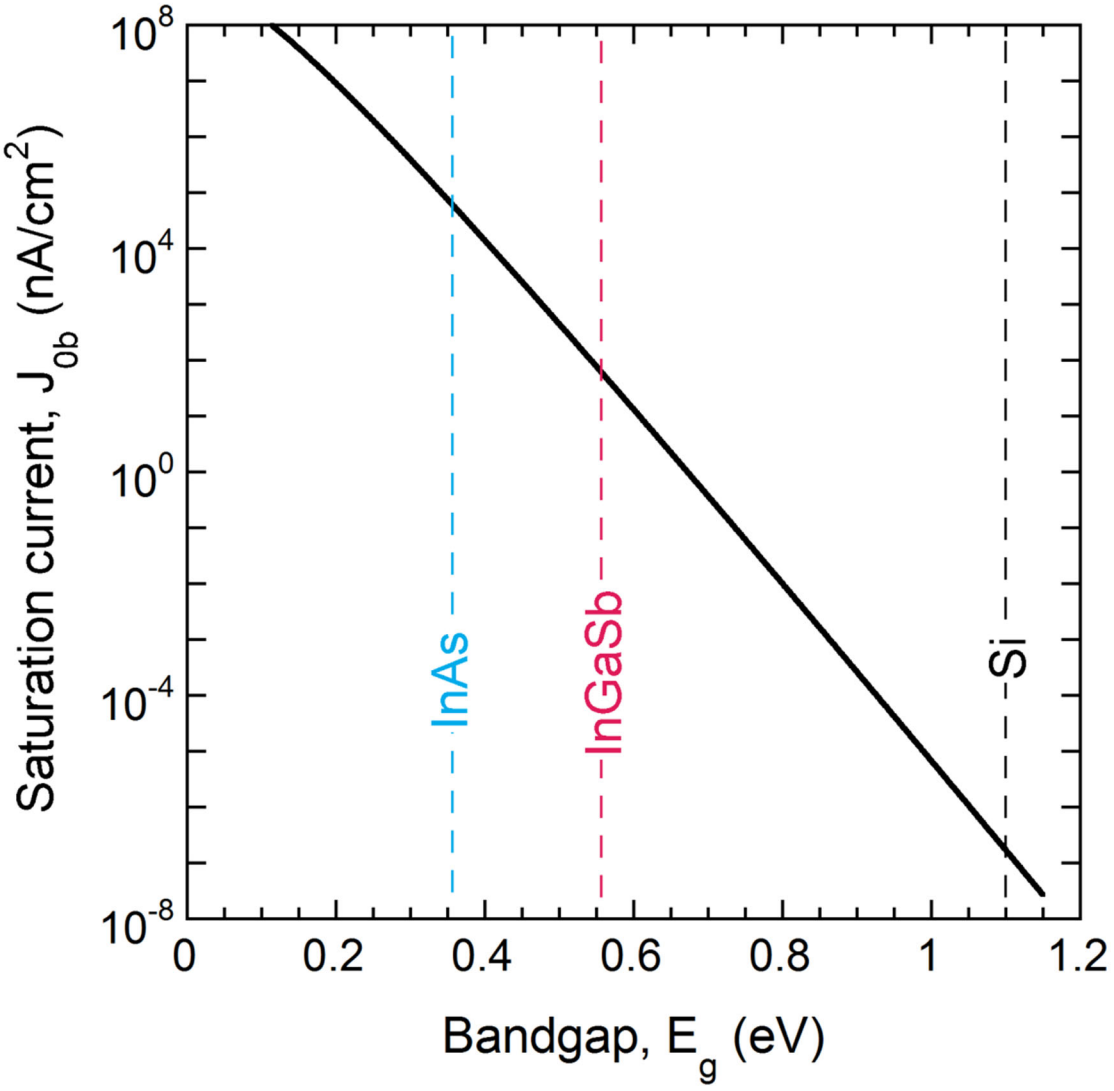

Figure 3.2 Saturation current vs bandgap energy if the emitter and cell are assumed to be blackbodies at 300 K. The three vertical lines indicate the bandgaps for InAs (0.36 eV), $In_{0.18}Ga_{0.82}Sb$ (0.56 eV), and Si (1.1 eV).

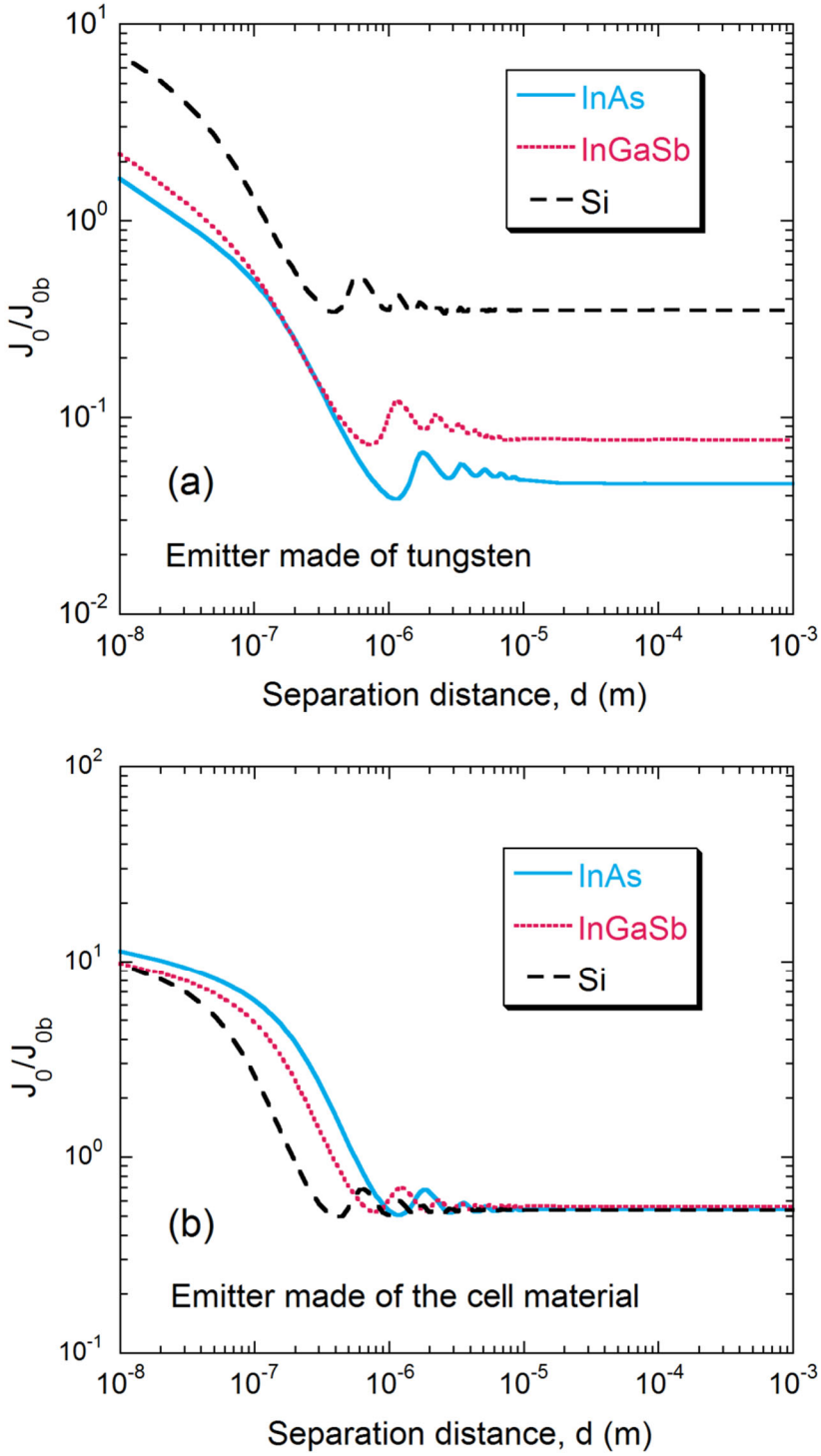

Figure 3.3 Normalized saturation current calculated by the MDM as a function of the separation distance for (a) a tungsten emitter and (b) an emitter made of same material as the TPV cell.

3.2.2 Dark Current

The effect of evanescent waves on saturation current is calculated using the MDM and shown in Figure 3.3(a) for a tungsten emitter and Figure 3.3(b) for an emitter made of the same material as the TPV cell. The saturation current is normalized to the ideal blackbody case and plotted as a function of the separation distance. In general, the saturation current increases as the separation distance decreases. The highest enhancement ratio of saturation current over the blackbody case is about 30 at a 10 nm separation distance, which demonstrates that using a constant saturation current in the standard method is inappropriate for modeling near-field TPV systems. Note that wave interference effects inside the vacuum gap are manifested as oscillations even after integration when the separation distance is on the order of the dominant wavelengths, resulting in the wavy features between d = 0.1 μm and 10 μm, depending on the bandgap. The near-field enhancement of saturation current is greater for the emitter made of the same material as the cell than when for the emitter made of tungsten. This results from a larger near-field transmission coefficient when the optical properties of the emitter and cell match each other [178].

Figure 3.4 illustrates the effect of the evanescent waves on dark current under forward bias for both types of emitters, which is again computed with the MDM. As a result of the variation of the saturation current, the *J-V* characteristics are also affected by the separation distance. For a given bias voltage, the dark current increases by orders of magnitude when the separation distance is reduced from the far-field regime to the near-field regime. Physically, this arises from the increased radiative recombination associated with photon tunneling when evanescent waves are taken into consideration. Among these

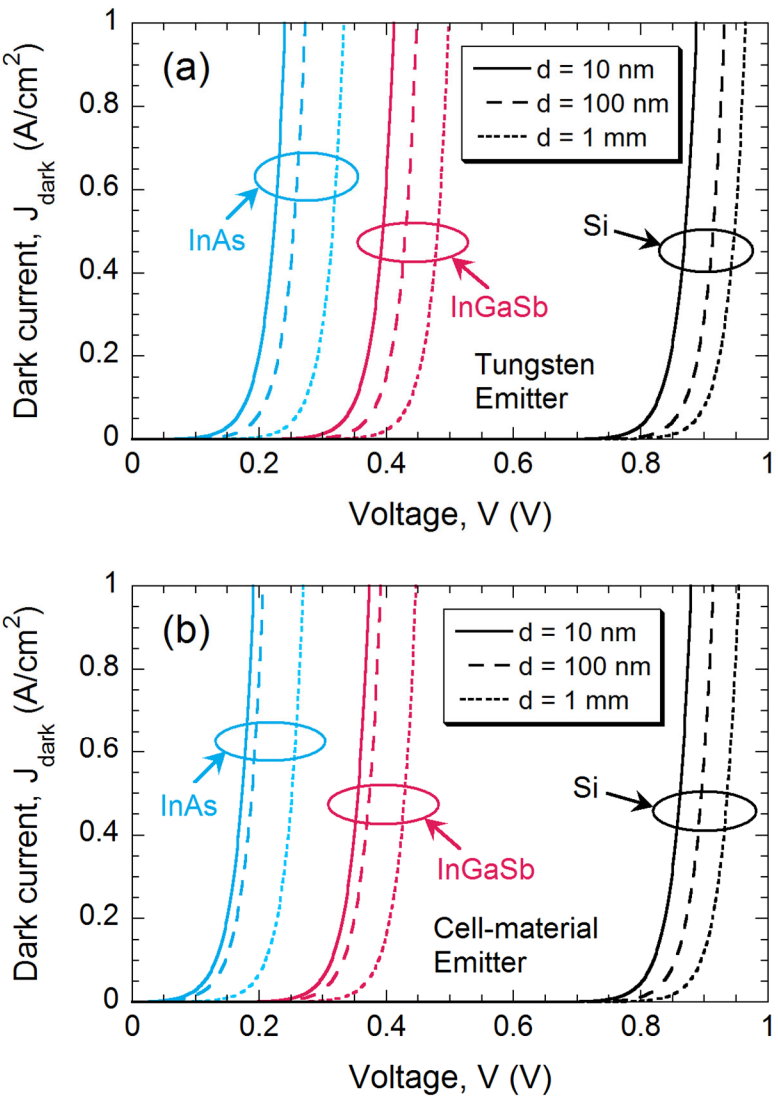

Figure 3.4 Dark current-voltage characteristics of different cell materials and separation distances calculated by the MDM for (a) a tungsten emitter and (b) an emitter made of same material as the TPV cell.

three materials, the dark current for an InAs TPV cell exhibits the largest currents at the lowest voltages because of its relatively low bandgap energy, as discussed previously. The consideration of near-field effects on dark current is crucial to the analysis of a TPV cell when using a superposition method. However, the near-field enhancement on the short-

circuit photocurrent will also influence the performance of a TPV cell. It should be noted that since the chemical potential under zero bias is zero, all three methods are consistent in calculating J_{sc} as long as Wien's approximation is valid.

3.2.3 Current and Voltage under Illumination

Figure 3.5 displays the *J-V* curves under illumination calculated using both the standard method and the MDM at separation distances of 10 nm, 100 nm, and 1 mm (far field), for the three types of TPV cells with either a tungsten emitter or an emitter made of the same material as the cell. It should be noted that here the *J-V* curve is plotted in the first quadrant according to Eq. (3.1), corresponding to the fourth quadrant in Figure 3.1(b). Of the six TPV systems examined, the InAs TPV cells with the lowest bandgap energy give the largest photocurrent, especially when the emitter is made of the same material as the cell. On the other hand, since Si has the highest bandgap, when the emitter is at 1000 K, the photocurrent is the smallest among the three materials studied. Because the contributions from evanescent waves increase the short-circuit photocurrent, the current increases significantly from the far field to the near field, especially as the separation distance is reduced to 10 nm. The difference between the two modeling methods is significant, which quantitatively indicates that the constant saturation current assumption used in the standard method is inappropriate in the near field. Moreover, with the W-InAs TPV system shown in Figure 3.5(a), the open-circuit voltage predicted by the standard method in the near-field cases exceeds 0.36 eV, the bandgap of InAs; this suggests that neglecting near-field effects may lead to nonphysical results.

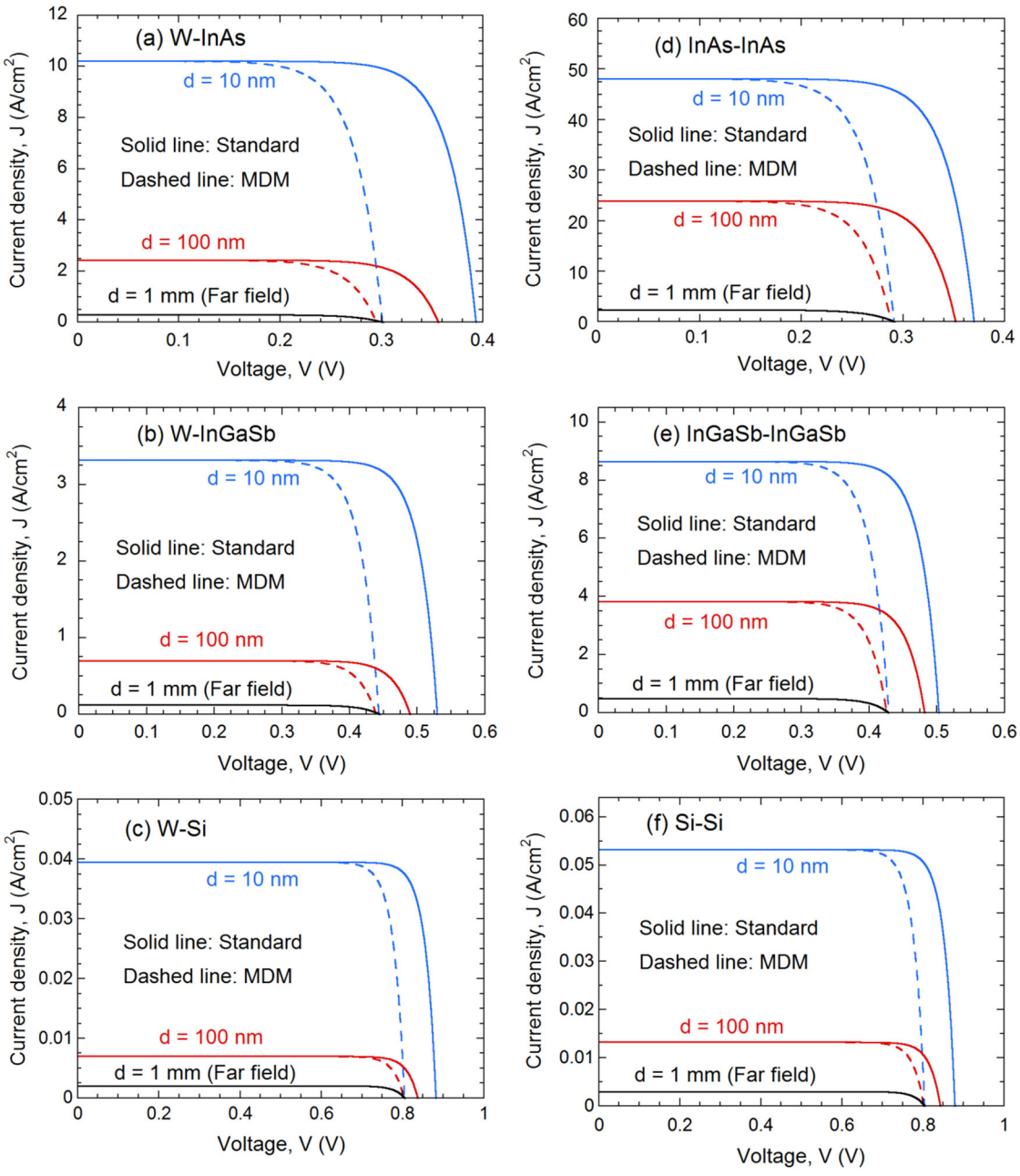

Figure 3.5 Current-voltage characteristics of TPV cells under illumination using the standard method and MDM for the corresponding separation distance. (a,b,c) are for a tungsten emitter, while (d,e,f) are for an emitter made of the same material as the cell.

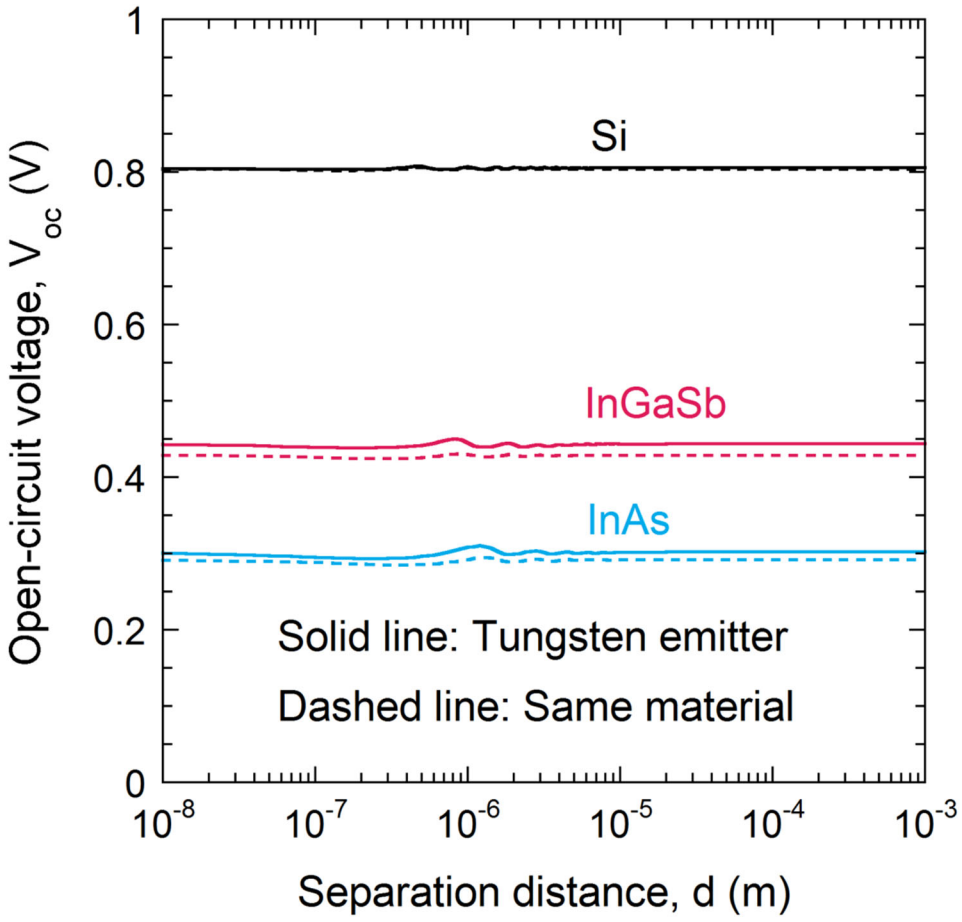

Figure 3.6 Open-circuit voltage vs separation distance calculated by the MDM for the three selected cell materials, when the emitter is made of tungsten (solid lines) or the same material as the cell (dashed lines).

The open-circuit voltage is shown directly as a function of separation distance in Figure 3.6 using the MDM. According to Eq. (3.15), open-circuit voltage is proportional to the ratio of the number of photons emitted from the source to that emitted from the cell. Generally speaking, the open-circuit voltage is not strongly affected by near-field operation, because evanescent waves have a comparable contribution to photon emission from both the emitter and the cell. A tungsten emitter gives a higher open-circuit voltage compared to an emitter made of same material as TPV cell. This phenomenon is more

pronounced for TPV cells made of lower bandgap materials because of the larger ratio of emission from the emitter to the emission from the cell when a lower energy range of the spectrum is considered. Interference effects are also present as observed for the saturation current and discussed in the previous section.

3.2.4 Output Electrical Power, Total Absorbed Energy, and Efficiency

As the *J-V* curves in Figure 3.5 indicate, the standard method may result in an overprediction of the maximum output power, which is the optimal area under the *J-V* curve. The differences in the calculated maximum output power, net radiative power received, and maximum efficiency between the standard method and the MDM are shown in Figure 3.7(a), (b), and (c), respectively, as functions of the separation distance. This TPV system uses a tungsten emitter at 1000 K and an $In_{0.18}Ga_{0.82}Sb$ cell at 300 K. It should be mentioned that the error of using the MDM compared with the exact calculation using the direct method is negligibly small. At large separation distances or in the far field, the standard method agrees with the MDM in terms of the maximum output power as shown in Figure 3.7(a). The difference becomes larger as the distance is reduced to the near-field regime, especially towards the nanoscale. As discussed previously, the use of a constant far-field saturation current with the standard method is inaccurate in the near field. For example, at $d < 25$ nm, the standard method may significantly overpredict the maximum output power by more than 20%.

There is a difference in the calculation of net radiant power received by the TPV cell between the standard method and the direct method. Note that the MDM uses exactly the same equation as the direct method in calculating the radiative heat transfer. Because the standard method does not consider the effect of the photon chemical potential for the

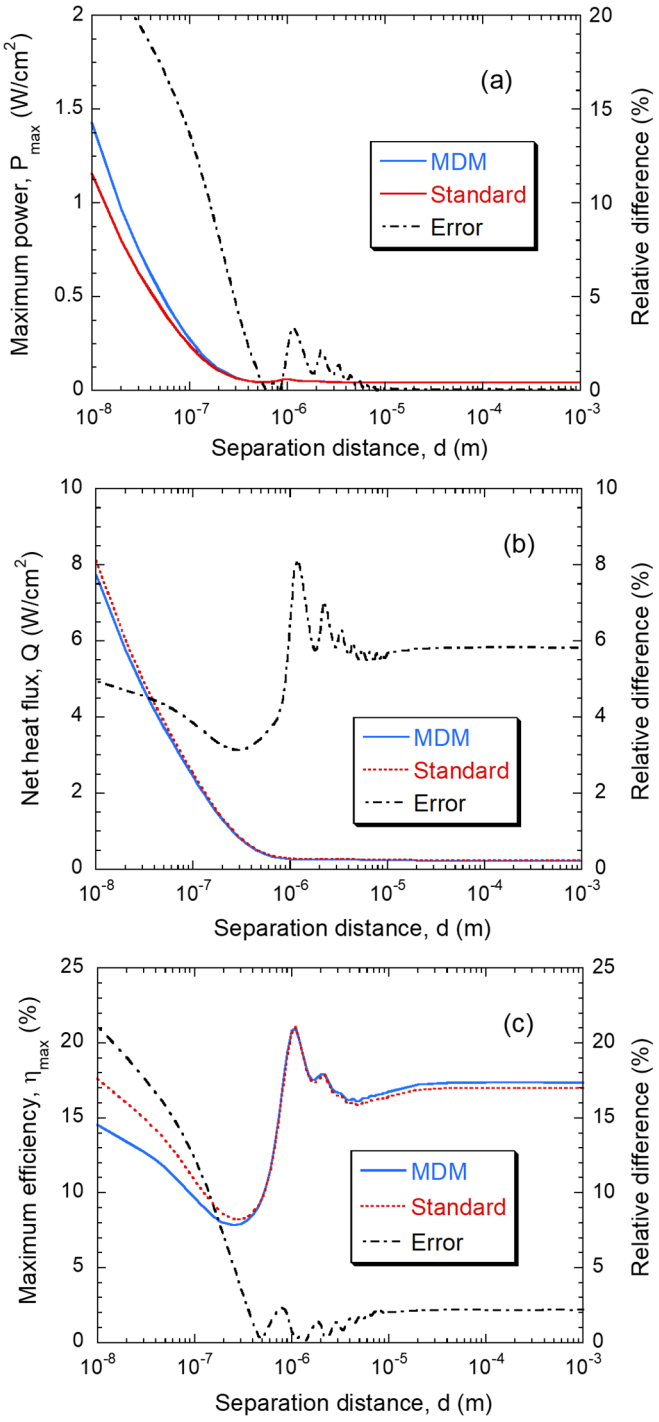

Figure 3.7 Comparison of the standard method and MDM for a tungsten emitter and $In_{0.18}Ga_{0.82}Sb$ TPV cell, where the error indicates the relative difference (absolute value) between the standard method and MDM: (a) maximum output power; (b) net heat flux; (c) maximum conversion efficiency.

cell, this could cause an error even in the far-field calculations as shown in Figure 3.7(b) for the operating voltage corresponding to the maximum output power. Since the operating voltage is comparable to the bandgap energy (0.56 eV), nonequilibrium effects factor strongly into the modified Bose-Einstein distribution given by Eq. (11), which influences the term $\Psi(\omega, T_2, \mu)$ in Eq. (13). For both the near- and far-field regimes, a 1-3% modeling error can exist when the TPV cell operates at its maximum output power. However, when the emitter is at a relatively low temperature and the cell has a relatively low bandgap (e.g., InAs cell), this error could be much larger. Therefore, taking photon chemical potential into consideration may be necessary to accurately predict the radiative heat flux and thereby the efficiency.

The maximum efficiency, which is calculated based on the maximum power output, is plotted in Figure 3.7(c) for both methods along with the relative error of the standard method. In the far-field regime, the difference is approximately 2.3% due to the error caused by the net heat flux calculation without considering chemical potential effect. In the near-field regime, the difference in efficiency between the two methods is dominated by the difference in maximum output power. Obviously, the standard method with a constant saturation current is not appropriate in the near field, since it has more than 20% error at d = 10 nm.

When TPV cells are operated at nanoscale distances from a thermal emitter, the constant saturation current approximation in the standard method is no longer valid. The MDM connects the direct method with the standard method and provides a more generalized method to model TPV systems for both near- and far-field operation. Using the MDM, we have demonstrated the effect of evanescent waves on the saturation current

by radiative recombination for ideal photoconverters with different bandgaps. The *J-V* curves under dark and illumination conditions, as well as the maximum output power and efficiency, are also affected by evanescent waves in the near-field regime. The standard method using a distance independent saturation current may yield considerable error when modeling near-field TPV systems. Our results improve the fundamental understanding and should aid in the design of near-field TPV systems

CHAPTER 4. SPATIAL PROFILE OF PHOTON CHEMICAL POTENTIAL IN NEAR-FIELD THERMOPHOTOVOLTAIC CELLS

This Chapter describes an iterative method that combines fluctuational electrodynamics (FE) with the full drift-diffusion model to solve the coupled charge and photon transport equations. The focus is on the determination of the impact of the photon chemical potential on the performance of the TPV devices. By comparison of the solution using the iterative method with that using the detailed balance approach based on a constant (or zero) photon chemical potential, the error caused by these assumptions can be quantified for different TPV devices. Two InAs near-field TPV cells with different thicknesses are selected as examples to illustrate the profile of photon chemical potential and when the assumption of a constant value may break down. The effects of injection level and surface recombination on the width and band structure of the depletion region are examined. For both the thin and thick TPV devices, the current density and conversion efficiency are calculated as functions of the bias voltage using the iterative method as well as the detailed balance approach (with or without a constant photon chemical potential) to demonstrate the significance of photon chemical potential on the performance of near-field TPV devices.

4.1 Iterative Solver of the Photon-Charge Coupled Models

Near-field TPV systems hold promise for energy harvesting due to the greatly enhanced power throughput with a potential improvement in conversion efficiency [22].

Most early studies on TPV devices did not consider the effect of luminescence from the TPV cell [73, 75, 184], or used simplified models for the radiative recombination [74] as well as reabsorption (also called photon recycling) [76]. The consideration of radiative recombination and reabsorption is an approximate approach of treating luminescence and photon recycling effects without explicitly using photon chemical potential in the Bose-Einstein statistics [79, 185]. External luminescence also affects the net radiative transfer rate between the emitter and the cell, especially when the emitter is at moderate temperatures [86, 88, 89, 123]. These studies used a direct modeling method for photon exchange between the emitter and the cell by assuming a spatially uniform photon chemical potential that is equal to the elementary charge (e) times the operating voltage (V); furthermore, the detailed balance approach was applied to calculate the carrier concentrations and thus the recombination rates. Feng *et al.* [81] illustrated the near-field effect on the dark current due to the modified saturation current in the near-field regime under the same assumptions. When the photogeneration rate is very high, the injected concentration could be comparable to or higher than the doping concentration. As shown by Blandre *et al*. [80] based on the full drift-diffusion model, the quasi-Fermi levels split nonuniformly within the active region of the cell. However, their study used a radiative recombination model to treat the luminescence effect without considering photon recycling and the effect of photon chemical potential on the net radiative heat transfer.

Following the modeling methods of the photon transport and charge transport in a radiative energy converter in Chapter 2, an iterative solver of the photon-charge coupled models is developed with a calculation example of a near-field InAs TPV device. A typical near-field TPV device consists of an emitter and a cell with an electric circuit, as shown in

Figure 4.1 for a 1D multilayer structure. There are $L + 1$ layers: $m = 0, 1, \ldots L$, and the end regions are assumed to be semi-infinite. A nanoscale vacuum gap (d) separates the emitter and the cell. While the method presented here is general, an InAs p-n junction is chosen as the active region due to its narrow bandgap ($E_g = 0.354$ eV at room temperature) and high quantum efficiency [186, 187]. The p-doped and n-doped InAs layers with thicknesses d_p and d_n are subdivided by a nonuniform mesh to determine the local photogeneration rate and to solve the charge transport equations. Both sides of the p-n junction are partially or completely coated with metal films acting as electrodes. The backside Au coating thickness d_{Au} is chosen to be 100 nm to improve the efficiency through reflection of sub-bandgap

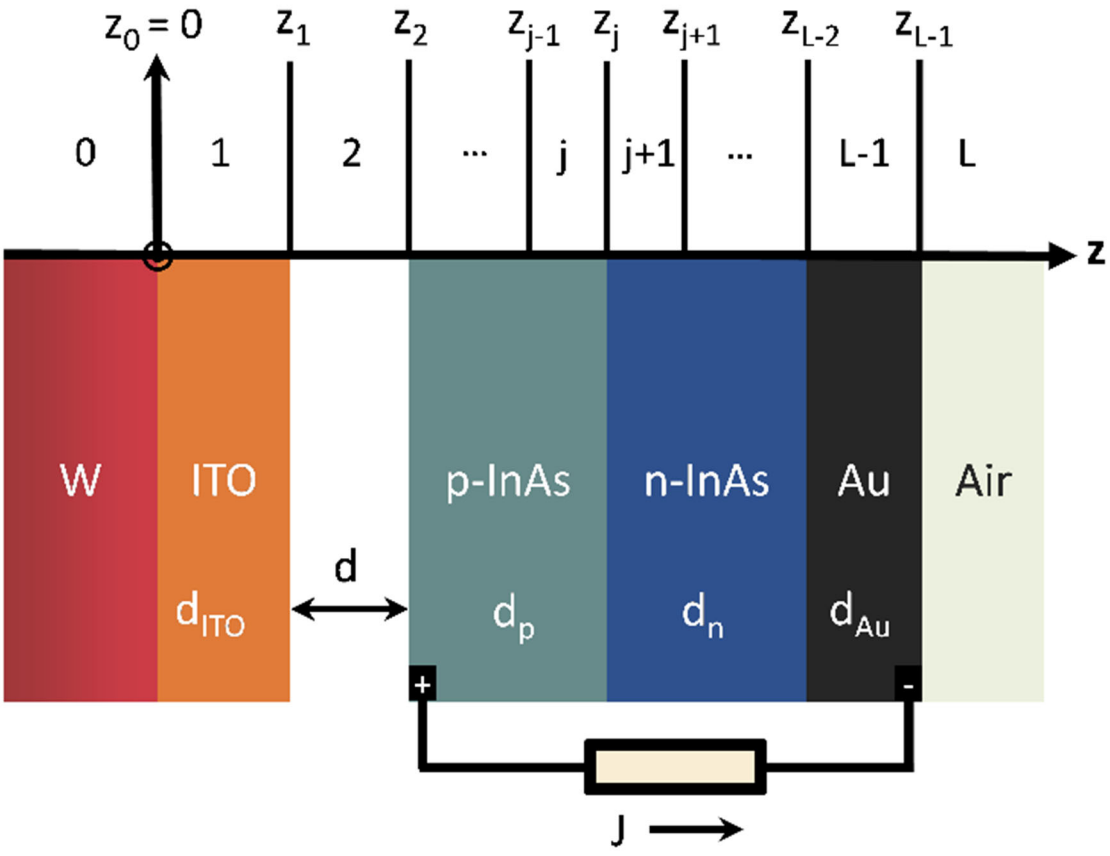

Figure 4.1 Schematic of an InAs TPV cell with an ITO coated tungsten emitter.

photons while serving as the back electrode [112]. The front metal grid is ignored in the model due to low shading area. An ITO thin film is coated on a semi-infinite bulk tungsten as a frequency-tunable Drude emitter, which can be optimized to match the bandgap of InAs to enhance the photogeneration rate [88]. The thickness of the ITO film is fixed to $d_{\mathrm{ITO}} = 30$ nm for optimized performance according to [8].

Since the profile of photon chemical potential is an input in Eqs. (2.25) and (2.27), the photon and charge transport equations are coupled. A general iterative solution algorithm is outlined here. To begin with, an assumed profile of photon chemical potential is used to calculate the photogeneration profile in the cell according to FE. Then, the quasi-Fermi level split is found by solving the semiconductor charge transport equations with the calculated photogeneration profile. This process yields an updated profile of the photon chemical potential. These steps are repeated until the specified convergence criteria are met. In the present modeling, it is assumed that the emitter and the cell are each at thermal equilibrium with specified temperatures T_{e} and T_{c}. This iterative solution method was also introduced and validated by Callahan *et al.* [82] using an open-source solver [172] of the charge transport equations and extended further to the study of other radiative energy converters.

The general procedure of this iterative solver is described in the following.

1. Initialization. Specify the device parameters, such as geometry, vacuum gap, the emitter and cell materials and their electrical and optical properties. The intrinsic, donor, and acceptor concentrations and recombination coefficients are also needed for the charge transport calculations. A suitable mesh size must be chosen especially for the cell regions.

2. Specification. Specify a bias voltage, V as the boundary condition. As a default, set $V = 0$ (short-circuit case) to begin.

3. Trial input. Set the photon chemical potential $\mu(z) = 0$ everywhere. This serves as the algorithm's initial input of the chemical potential profile.

4. Photogeneration calculation. Obtain the photogeneration profile based on Eq. (2.25) using the recursive transfer approach under the framework of FE for specified chemical potential profile $\mu(z)$. Note that the obtained generation rate is assumed to be uniform within each layer Δz_j $(j = 3,...L-2)$. This is exactly what is needed in the numerical solution of the charge transport equations.

5. Charge transport solution. Solve the charge transport equations using the photogeneration profile obtained from the previous step to obtain the steady-state solution. Doing so will yield values $E_{\mathrm{f,e}}$ and $E_{\mathrm{f,h}}$ and thus an updated $\mu(z)$ according to Eq. (2.41).

6. Iteration. Repeat steps 4 and 5 until the convergence criteria are met. In the present study, an upper limit (10^{-5}) in the relative difference between the photogeneration rate and an upper limit (10^{-7} eV) in the absolute difference between the photon chemical potential are used in combination to yield satisfactory convergence within reasonable computational time.

7. Current and power outputs: The current density in the circuit for the given bias voltage can be calculated using $J = J_{\mathrm{e}} + J_{\mathrm{h}}$ in the junction since the current density is the same around the circuit at steady state.

The above procedure yields the complete solution that can be used to evaluate the performance of the TPV device at a certain forward bias voltage. The *J-V* curve are produced by repeating steps 2-7 with appropriate increment in V from the short-circuit

condition ($V = 0$) to the open-circuit condition when $J = 0$. Some trial-and-error are needed to determine the open-circuit voltage (V_{oc}) by refining the step size. It takes about 2-3 days to run a *J-V* curve for a given case with a dual eight core XEON E5-2687W 3.1GHz workstation using parallel computing. It should be noted that the inclusion of chemical potential in the photogeneration and radiative heat transfer based on fluctuating electrodyanmics has taken into account the luminescence and photon recycling effects [79].

4.2 Analysis of Two Near-Field InAs TPV Devices

A simple analysis is given first to illustrate the effect of photon chemical potential without using the iterative solution or the detailed balance approach. Then, two InAs cells with different thicknesses are modeled with the iterative method and compared with the detailed balance analysis under either a constant or zero photon chemical potential assumption.

4.2.1 Simple Analysis of the Luminescence Effect in TPV Cells

The photon chemical potential is the characteristic parameter for the luminescence effect in TPV cells operating in either the far field or the near field. This can be evaluated by comparing the difference in net radiation exchange between the emitter and cell with and without a constant chemical potential applied to the cell. The most important photons for semiconductor materials are those close to the bandgap energy. For a simple analysis, one may consider photons at the frequency ω_g. A relative error χ_g in the net radiation exchange for photons at the bandgap energy is introduced to estimate the significance of photon chemical potential on the radiative energy exchange:

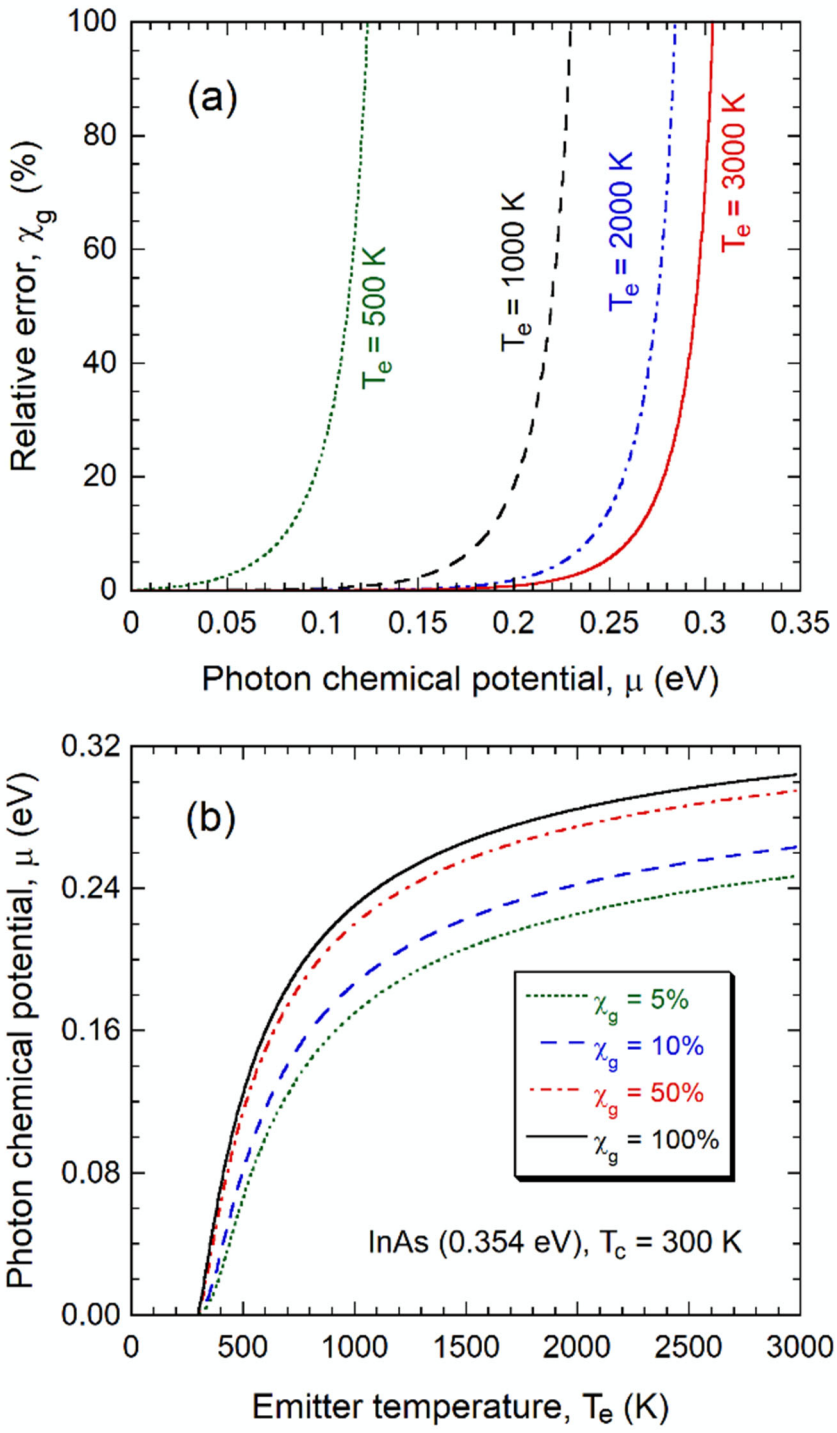

Figure 4.2 (a) The error due to neglecting photon chemical potential in radiation exchange as a function of photon chemical potential for various emitter temperatures; (b) the contour plot of the relative error in a μ-T_e plane.

$$\chi_g(\omega_g, T_e, T_c, \mu_c) = \left| \frac{Q_g(T_e, T_c, \mu_c) - Q_g(T_e, T_c, 0)}{Q_g(T_e, T_c, \mu_c)} \right| = \frac{\Psi(\omega_g, T_c, \mu_c) - \Psi(\omega_g, T_c, 0)}{\Psi(\omega_g, T_e, 0) - \Psi(\omega_g, T_c, \mu_c)} \tag{4.1}$$

where T_e and T_c are the temperatures of the emitter and cell, respectively, Q_g is the spectral radiation exchange between the emitter and cell at ω_g, and μ_c ($< E_g$) is the photon chemical potential of the cell and is taken as a constant. Note that Eq. (3.1) is applicable to both the far-field and the near-field regimes. For a cell with given temperature and bandgap, the relative error will increase if the emitter temperature T_e decreases or if the photon chemical potential μ_c increases.

Taking InAs as the cell with E_g = 0.354 eV at T_c = 300 K, the effect of photon chemical potential is shown in Figure 4.2(a) for various emitter temperatures. The error in the radiation exchange between the emitter and cell due to neglecting the photon chemical potential exponentially increases as the photon chemical potential increases. On the other hand, if the emitter temperature is higher, a larger photon chemical potential may be tolerable with the same error bound. This can be seen clearly in Figure 4.2(b) which plots the constant χ_g curves. For a given emitter temperature, the photon chemical potential must be small enough such that the error due to neglecting the photon chemical potential is below the error bound indicated by each curve. It should be noted that in a real TPV cell, the error in the total radiation exchange would be somewhat lower than χ_g since the effect of μ_c decreases as the frequency increases.

This simple analysis can be applied to semiconductors with different bandgaps. In Figure 4.3, the 10% error curves are displayed for five common semiconductor materials

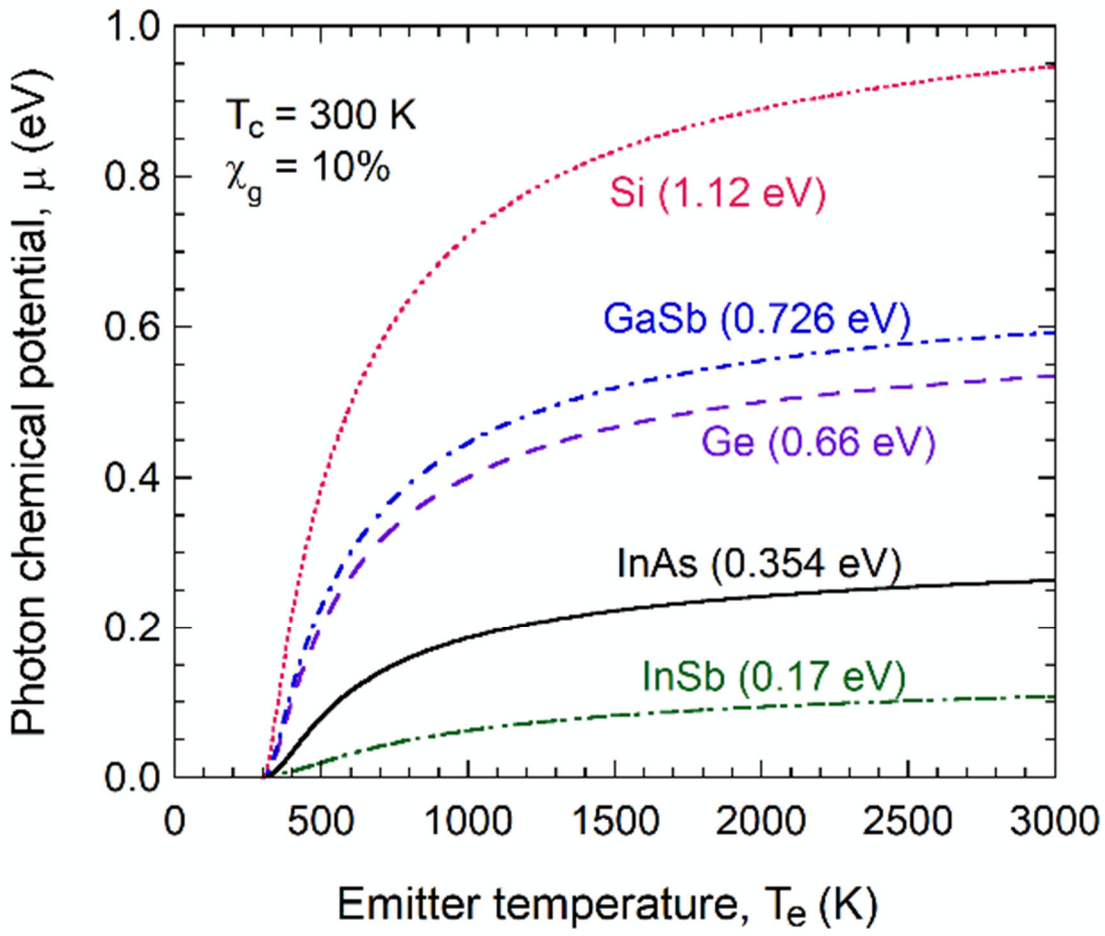

Figure 4.3 The 10% error criterion for various semiconductor materials whose bandgap values are shown in parentheses.

(whose bandgap values are indicated in the figure) at T_c = 300 K. In order to maintain an error smaller than 10%, the photon chemical potential must not exceed certain values for a given E_g. Clearly, the photon chemical potential plays an important role, especially when the emitter is at moderate temperatures and the cell's bandgap is relatively small. While this simple analysis provides an intuitive suggestion about whether the iterative solution is necessary, it cannot quantify the actual luminescence effect. It will be shown in Sec. III.C that sometimes even though the photon chemical potential varies little throughout the *p*-*n* junction regions, its value may deviate from the product *Ve*.

4.2.2 Parametrization of the Near-Field InAs Devices

Two near-field InAs TPV devices with different geometric structures are considered in this work. In the following, the emitter (layers $m = 0$ and 1) is assumed to be at a uniform temperature $T_e = 900$ K; the active region of the cell (layers m from 3 to $L - 2$), the Au coating (layer $m = L - 1$), and air (layer $m = L$) are assumed to be at $T_c = 300$ K. The vacuum spacing is set to be $d = 10$ nm, which is sufficiently small to establish a high-injection level in the *n*-region. The dielectric function of tungsten is taken from the room temperature values [181] without considering temperature dependence. The dielectric function of InAs is obtained from Ref. [181] without considering the free-carrier contributions. Free-carrier contributions were included by Milovich *et al.* [187] using a Drude term, but this is not the main focus of the present study. The dielectric functions of ITO and Au are modeled by a Drude model $\varepsilon(\omega) = \varepsilon_\infty - \omega_p^2 / (\omega^2 + i\gamma\omega)$ to account for free-electron contributions [2]. For ITO: $\varepsilon_\infty = 4$, $\omega_p = 1.52 \times 10^{15}$ rad/s, and $\gamma = 1.52 \times 10^{14}$ rad/s [8]; for Au: $\varepsilon_\infty = 1$, $\omega_p = 1.37 \times 10^{16}$ rad/s, and $\gamma = 5.31 \times 10^{13}$ rad/s [112]. The effects of temperature and lattice vibration on the dielectric function of ITO are neglected.

To model the InAs cell, the acceptor and donor concentrations are set to $N_A = 8 \times 10^{17}$ cm^{-3} and $N_D = 2 \times 10^{16}$ cm^{-3} in this study. The intrinsic concentration is $n_i = 6.06 \times 10^{14}$ cm^{-3} for InAs at room temperature. For the bulk recombination, the following parameters are used: $C_e = C_h = 2.26 \times 10^{-27}$ cm^6 s^{-1} and $\tau_e = \tau_h = 100$ ns [188].

A Caughey-Thomas-like model is used to describe the electron and hole mobilities depending on temperature and doping concentration [189]. This low-field mobility model is expressed as

$$\upsilon\left(N_{(\mathrm{A,D})},T\right)=\upsilon_{\min}+\frac{\upsilon_{\max}\left(300/T\right)^{\theta_1}-\upsilon_{\min}}{1+\left\{N_{(\mathrm{A,D})}\Big/\left[N_{\mathrm{ref}}\left(T/300\right)^{\theta_2}\right]\right\}^{\zeta}} \tag{4.2}$$

Table 4.1. Parameters of InAs cells used in the present study. Note that the band gap is 0.354 eV at 300 K and the equilibrium concentration is $n_{\mathrm{i}}=6.06\times10^{14}$ cm^{-3}.

	p-region		*n*-region	
Thicknesses of the thin cell (nm)	200		200	
Thicknesses of the thick cell (nm)	400		5000	
	Electron	Hole	Electron	Hole
N (cm^{-3})	--	$N_{\mathrm{A}}=8\times10^{17}$	$N_{\mathrm{D}}=2\times10^{16}$	--
υ (cm^{-2} V^{-1} s^{-1})	$\upsilon_{\mathrm{e}}=18300$	$\upsilon_{\mathrm{h}}=166$	$\upsilon_{\mathrm{e}}=26800$	$\upsilon_{\mathrm{h}}=370$
τ (ns)	$\tau_{\mathrm{n}}=100$	$\tau_{\mathrm{p}}=100$	$\tau_{\mathrm{n}}=100$	$\tau_{\mathrm{p}}=100$
C (cm^{6} s^{-1})	$C_{\mathrm{e}}=C_{\mathrm{h}}=2.26\times10^{-27}$		$C_{\mathrm{e}}=C_{\mathrm{h}}=2.26\times10^{-27}$	
S (cm s^{-1}) (Thin cell)	$S_{\mathrm{e,p}}=100$	$S_{\mathrm{h,p}}=10000$	$S_{\mathrm{e,n}}=10000$	$S_{\mathrm{h,n}}=100$
S (cm s^{-1}) (Thick cell)	$S_{\mathrm{e,p}}=100000$	$S_{\mathrm{h,p}}=100000$	$S_{\mathrm{e,n}}=100000$	$S_{\mathrm{h,n}}=100000$

The parameter values for InAs are taken from [189]. For electrons, $\upsilon_{\min} = 1000\ \mathrm{cm^2V^{-1}s^{-1}}$, $\upsilon_{\max} = 34000\ \mathrm{cm^2V^{-1}s^{-1}}$, $N_{\mathrm{ref}} = 1.1\times10^{18}\ \mathrm{cm^{-3}}$, $\theta_1 = 1.57$, $\theta_2 = 3.0$, and $\zeta = 0.32$; for holes, $\upsilon_{\min} = 20\ \mathrm{cm^2V^{-1}s^{-1}}$, $\upsilon_{\max} = 530\ \mathrm{cm^2V^{-1}s^{-1}}$, $N_{\mathrm{ref}} = 1.1\times10^{17}\ \mathrm{cm^{-3}}$, $\theta_1 = 2.3$, $\theta_2 = 3.0$, and $\zeta = 0.46$. In the following, a thin *p-n* junction and a thick *p-n* junction are taken as examples to demonstrate the nonuniform photon chemical potential and its effect on the performance of near-field TPV devices. For the thin cell, $d_p = d_n = 200$ nm, and the surface recombination velocities are set to be $S_{\mathrm{e},p} = S_{\mathrm{h},n} = 100$ cm/s and $S_{\mathrm{e},n} = S_{\mathrm{h},p} = 10,000$ cm/s to distinguish the minority carries and majority carriers. These values are within the range of high-quality films [187, 188]. For the thick cell, d_p = 400 nm and d_n = 5 μm, while all the surface recombination velocities are taken as 10^5 cm/s, which is reasonable for typical semiconductor cells [188]. The key parameters used in this work are listed in Table 4.1.

4.2.3 Modeling Results of a Thin Near-Field InAs TPV Device

For a conventional solar PV cell made of a *p-n* junction, the quasi-Fermi level split across the depletion region of the cell is assumed to be equal to the product of the forward bias voltage and elementary charge [163, 164, 174]. This is a widely recognized argument for PV cells with two hidden assumptions: the PV cells are under low-injection condition and the PV cells are thick. In most cases, the first assumption is likely to be valid for regular doped-silicon PV cells, because the injection level due to the spectral intensity from one or even several suns would still be moderate. For the second assumption, the widths of *p*- and

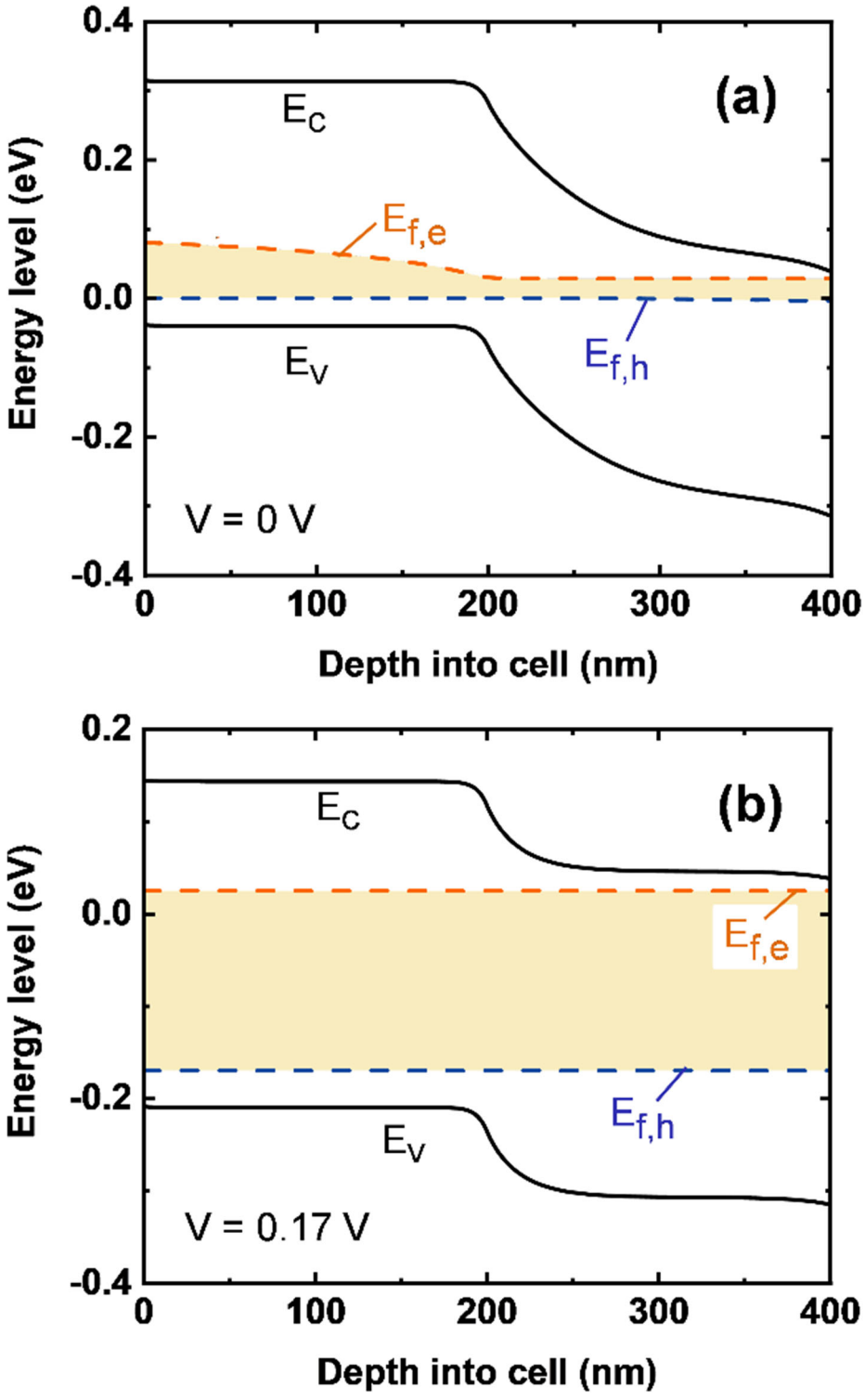

Figure 4.4 The energy band diagrams of the thin near-field InAs TPV cell under (a) short-circuit (V = 0 V) and (b) maximum-efficiency (V = 0.17 V) conditions.

n-regions in the PV cells are typically much larger than the depletion region. However, this may not be the case for thin-film near-field TPV devices.

The band diagrams of the thin TPV cell (d_p = d_n = 200 nm) with a vacuum gap distance of d = 10 nm are calculated at the short circuit and maximum efficiency (corresponding to V = 0.17 V) conditions, which are shown in Figure 4.4(a) and 4.4(b), respectively. The height of the shaded region represents the differences between the quasi-Fermi levels, which is nothing but the photon chemical potential profile $\mu(z)$. The depletion region (sloped conduction and valence bands) is broadened and extended throughout the *n*-region, especially for the short circuit case. The end of depletion region (sloped conduction and valence bands) in the n-region is close to the back surface, especially for the short circuit case. Surface recombination also plays a role on the depletion region

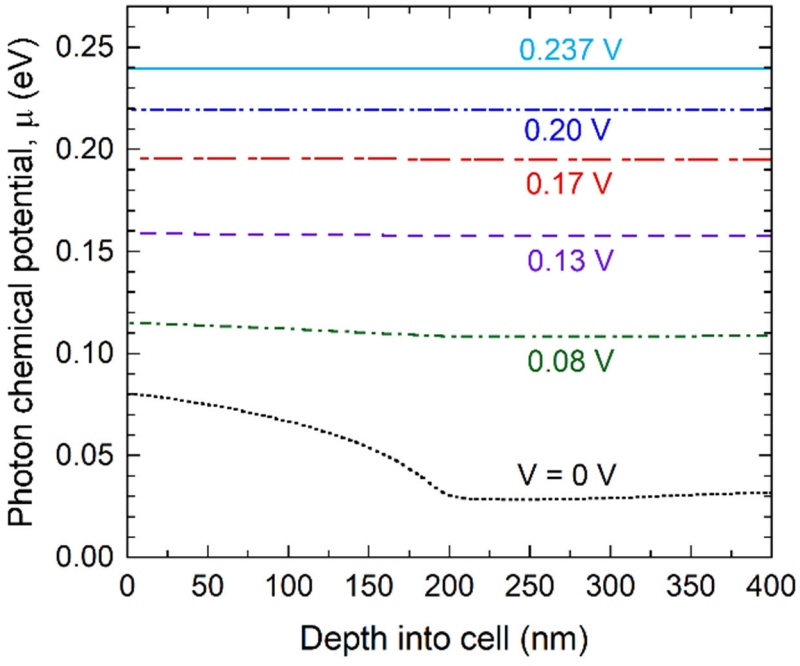

Figure 4.5 The profile of photon chemical potential in the *p*-*n* junction of the thin cell for various forward voltages.

because the distribution of free carriers inside the *n*-region is affected by the electric field generated by the well-passivated surface. This is evidenced in Figure 4.4(a) and 4.4(b) by the nonzero slope in the conduction and valence bands near 400 nm. Note that high-injection condition exists in the *n*-region. Figure 4.4(a) shows that $\mu(z)$ is not zero but a strong function of z. High-quality surfaces with less surface defects for both hole and electron, as used here, trap the free carriers inside the *p*-*n* junction, giving rise to a non-zero quasi-Fermi level difference in the depletion region even with $V = 0$. When $V = 0.17$ V, as can be seen from Figure 4.4(b), $\mu(z)$ is approximately a constant which is 0.195 eV, which is about 15% greater than the product Ve.

The profile of photon chemical potential is calculated for different voltages and shown in Figure 4.5. For small bias voltages, $\mu(z)$ decreases as z increases. When V increases to above 0.13 V, the variation of $\mu(z)$ becomes negligibly small. Nevertheless, the calculated $\mu(z)$ from the iterative method is always greater than Ve. The difference in the photon chemical potential calculated from the iterative solution and by assuming a constant value based on the detailed balance analysis is expected to impact the characteristics of the TPV cell.

The luminescence effect is demonstrated in Figure 4.6(a) and 4.6(b) by plotting the net photogeneration rate and the net absorbed energy rate (per unit area) of the cell versus the bias voltage. As V increases, the luminescence effect reduces both G_{cell} and Q, as compared to the case with $\mu = 0$, when luminescence effect is completely neglected. Since the iterative solution gives $\mu(z)$ greater than Ve, the curve with $\mu = \mu(z)$ is always the lowest. As shown in Figure 4.2(b), when $\mu < 0.15$ eV, χ_g is within 5% and the impacts of chemical potential on the photogeneration and heat transfer are relatively small. The differences

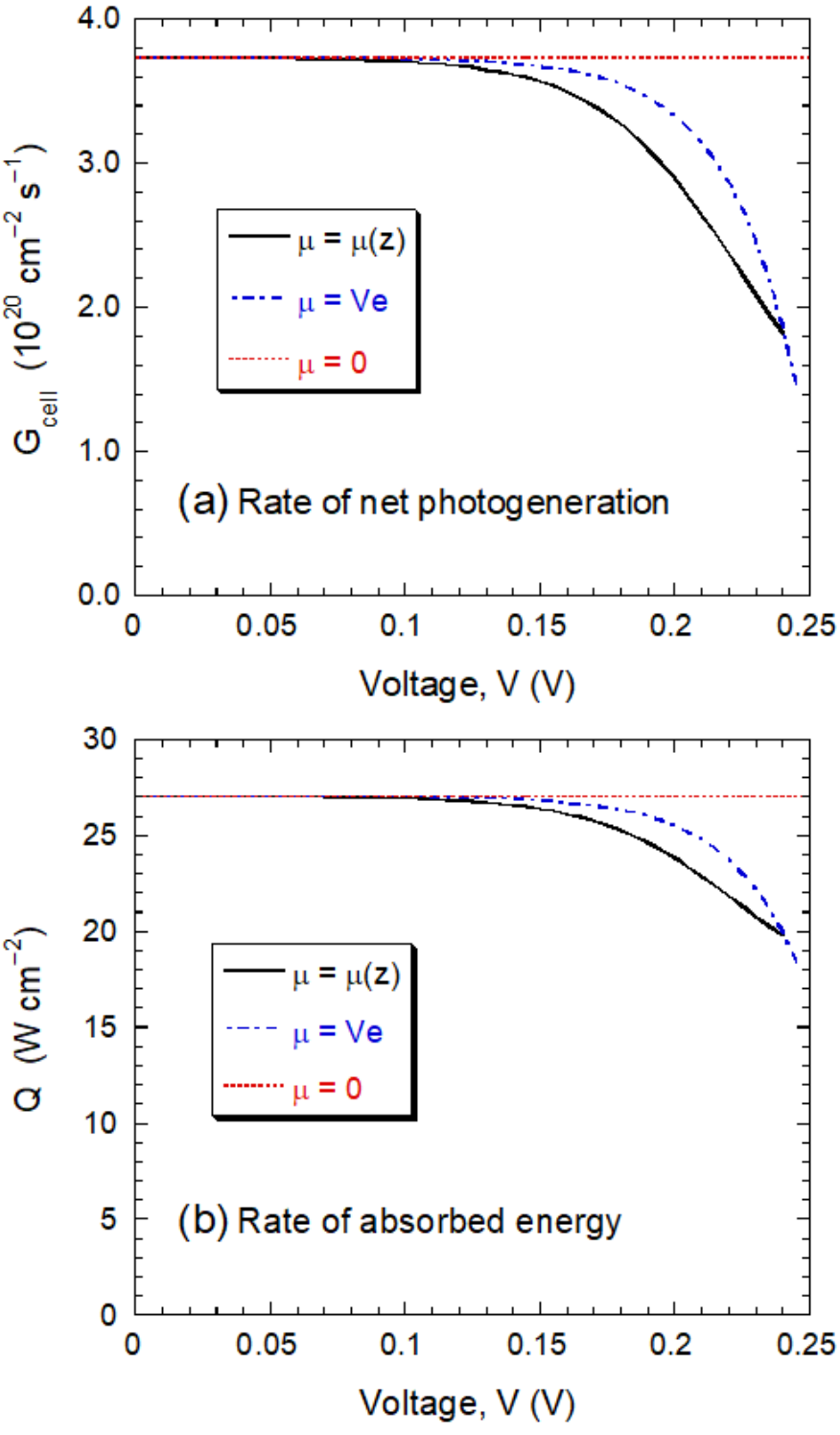

Figure 4.6 (a) Net photogeneration rate and (b) net absorbed energy rate vs forward bias voltage under three different treatments of the photon chemical potential profile for a thin InAs TPV cell.

become larger as V increases to above 0.12 V. The maximum relative error in G_{cell} for $\mu = Ve$ is 21% taking the iterative method as the reference, which occurs at $V = 0.22$ V. At $V = 0.17$ V when the maximum efficiency occurs according to the iterative method, the relative error is 6.1% with $\mu = Ve$ and 9.7% with $\mu = 0$. Note that χ_g based on $\mu = 0.17$ eV is 6.3%, suggesting that χ_g gives a good indication when the profile of photon chemical potential should be considered. In terms of the net absorbed energy, the error for using $\mu = Ve$ is 3.1% and that for $\mu = 0$ is 4.9% at the maximum efficiency condition, $V = 0.17$ V. The smaller error in Q is because sub-bandgap photons that contribute more than 50% of the heat transfer rate are not altered by the photon chemical potential, as suggested in Eq. (2.10).

The current density and efficiency are calculated as functions of the voltage as shown in Figure 4.7 with the iterative method, $\mu = \mu(z)$, and compared with these obtained from the detailed balance analysis for $\mu = Ve$ and $\mu = 0$. The detailed balance approach overpredicts the current density in particular as V increases to beyond 0.13 V. The difference between the current densities with $\mu = Ve$ and $\mu = 0$ is purely due to the net photogeneration rate as the recombination rates are the same according to the detailed balance analysis. Since the recombination rate increases with V, the current density drops to zero as V increases to the open circuit voltage V_{oc}. The open circuit voltage for $\mu = Ve$ is slightly larger than that for $\mu = \mu(z)$ but much smaller than that for $\mu = 0$ as can be seen from Figure 4.7(a). As shown in Figure 4.7(b), the maximum efficiencies are 39.8% at $V = 0.205$ V for $\mu = 0$, 37.4% at $V = 0.19$ V for $\mu = Ve$, and 32.7% at $V = 0.17$ V for $\mu = \mu(z)$. These differences are due to the combination of effects caused by the profile of photon chemical potential and the underlying charge transport. The comparisons of the major

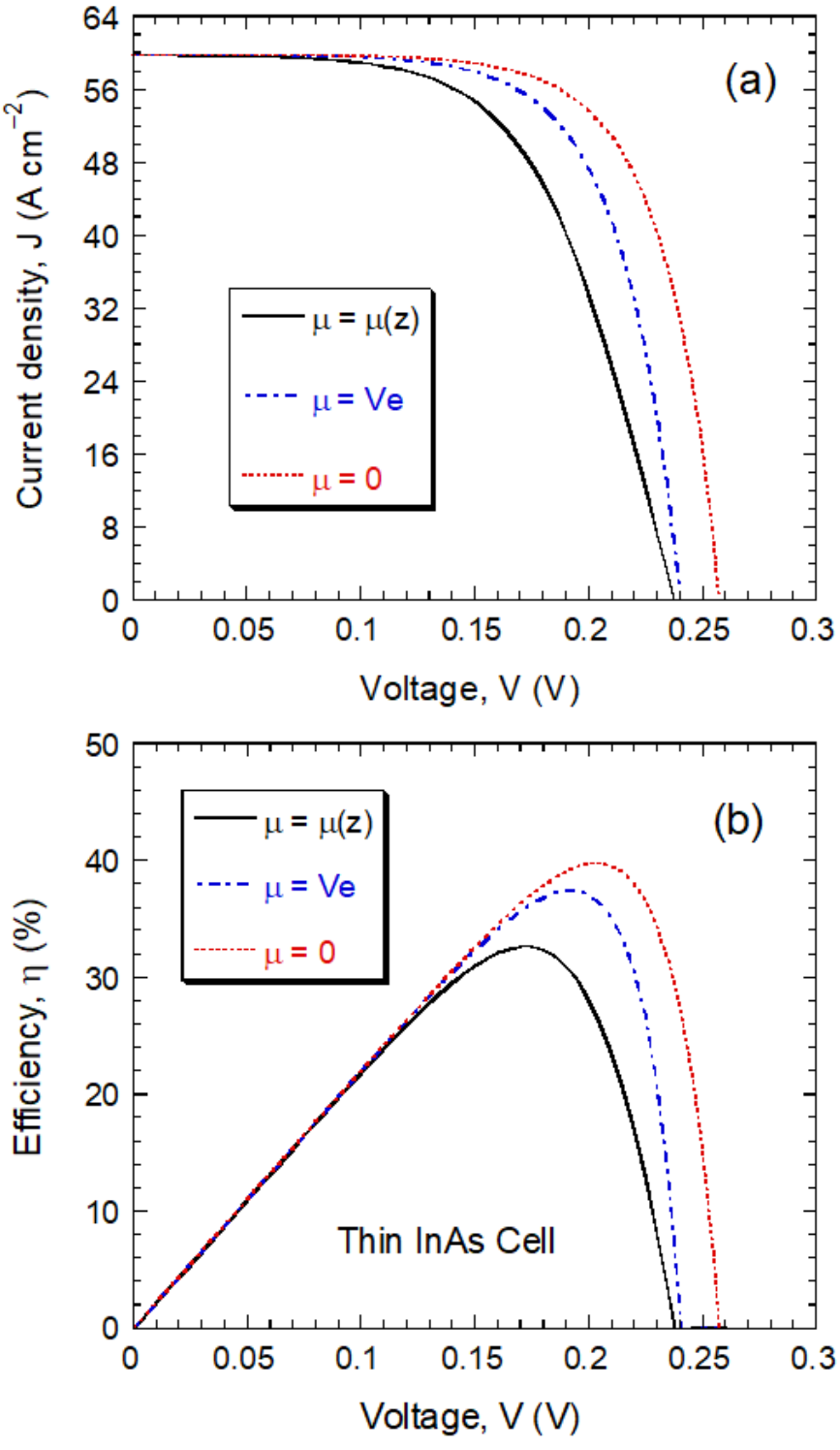

Figure 4.7 (a) Current density and voltage characteristics and (b) efficiency and voltage characteristics using three different treatments of the photon chemical potential profile for a thin InAs TPV cell.

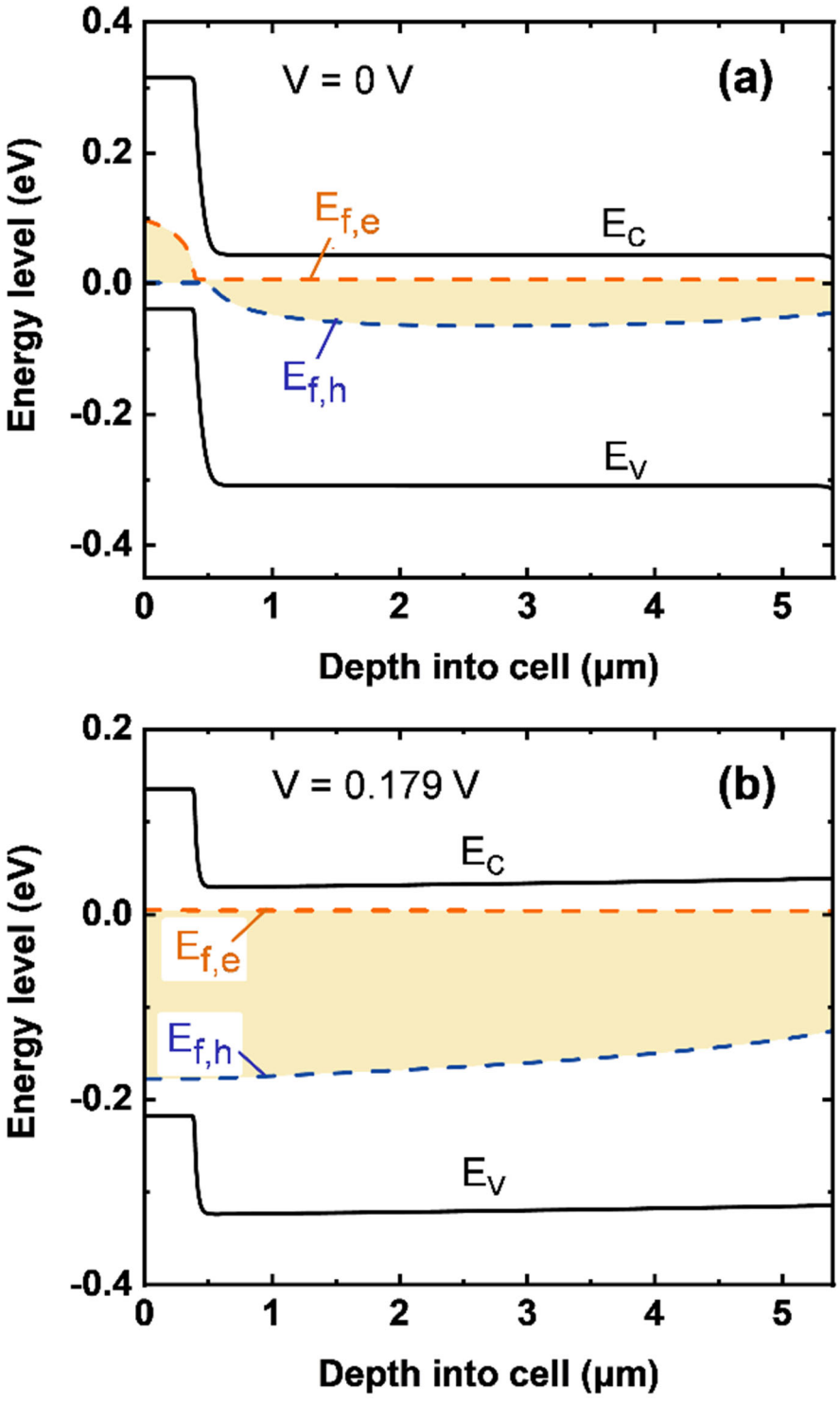

Figure 4.8 The energy band diagrams of the thick InAs TPV cell under (a) short-circuit and (b) open-circuit ($V = V_{oc} = 0.179$ V) conditions.

parameters reveal that the accurate modeling of the photon chemical potential and the charge transport are critical to the prediction of the performance near-field TPV devices.

It should be noted that with even higher level of injection, the Boltzmann distribution used to approximate the Fermi-Dirac distribution of electron and hole systems may be questionable; hence, more comprehensive models considering degenerate semiconductors may be necessary to accurately describe the band diagrams. Such a situation does not occur for the cases studied in this work and therefore will not be further discussed.

4.2.4 Modeling Results of a Thick Near-Field InAs TPV Device

A thick near-field InAs TPV cell with high surface recombination velocities is modeled to examine the spatial variation of $\mu(z)$ and the accuracy of the detailed balance analysis. The band diagrams of the thick cell with the same prescribed emitter and cell temperatures (T_e = 900 K and T_c = 300 K) and separation distance (d = 10 nm) at short-circuit and open-circuit conditions are shown in Figure 4.8(a) and 4.8(b), respectively. Note that the width of the *p*-region is 400 nm and that of the *n*-region is 5 μm. A narrow depletion region is observed between the *n*- and *p*- regions, since the injection level is moderate in this case. Furthermore, the quasi-Fermi level split across the depletion region is close to Ve. However, the height of the shaded region varies greatly since photogeneration is highly nonuniform in the near-field regime [75, 78].

The spatial variation of the photon chemical potential is shown in Figure 4.9 at different forward voltages. When the voltage is below 0.13 V, $\mu(z)$ decreases and reaches a minimum ($\approx Ve$) in the depletion region. In the *n*-region, $\mu(z)$ gradually increases to reach

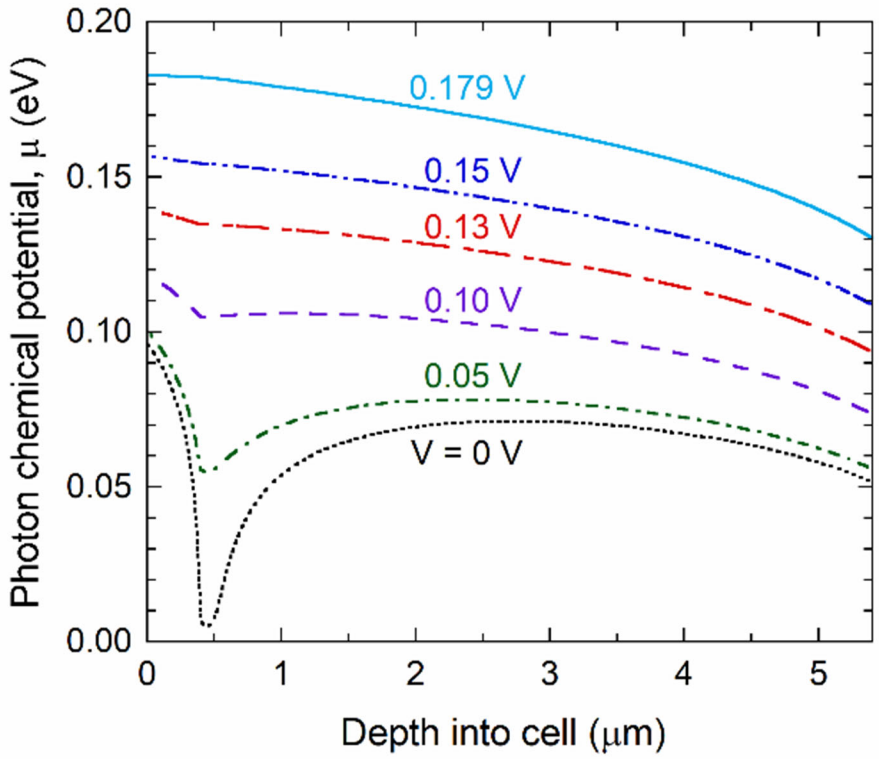

Figure 4.9 The profile of photon chemical potential of the thick cell with various forward bias voltages.

a maximum and then decreases toward the end. For the open-circuit case, $\mu(z)$ varies monotonically from 0.18 eV to 0.13 eV. Clearly, a constant μ assumption is not valid for near-field TPV devices even for moderate injection level.

The current density and efficiency are plotted in Figure 4.10 against the voltage for the thick-cell TPV device. The open-circuit voltage is V_{oc} = 0.145 V with the detailed balance analysis and V_{oc} = 0.179 V with the iterative method. The difference between $\mu = Ve$ and 0 is less than 5% for $V < 0.14$ V and hence the two curves almost overlap with each other. In this case, the luminescence effect is negligibly small due to the small chemical potential. The detailed balance analysis underpredicts both J and η when $V > 0.075$ V. As shown in Figure 4.10(b), the maximum efficiency of 22.2% (at $V = 0.13$ V) calculated by

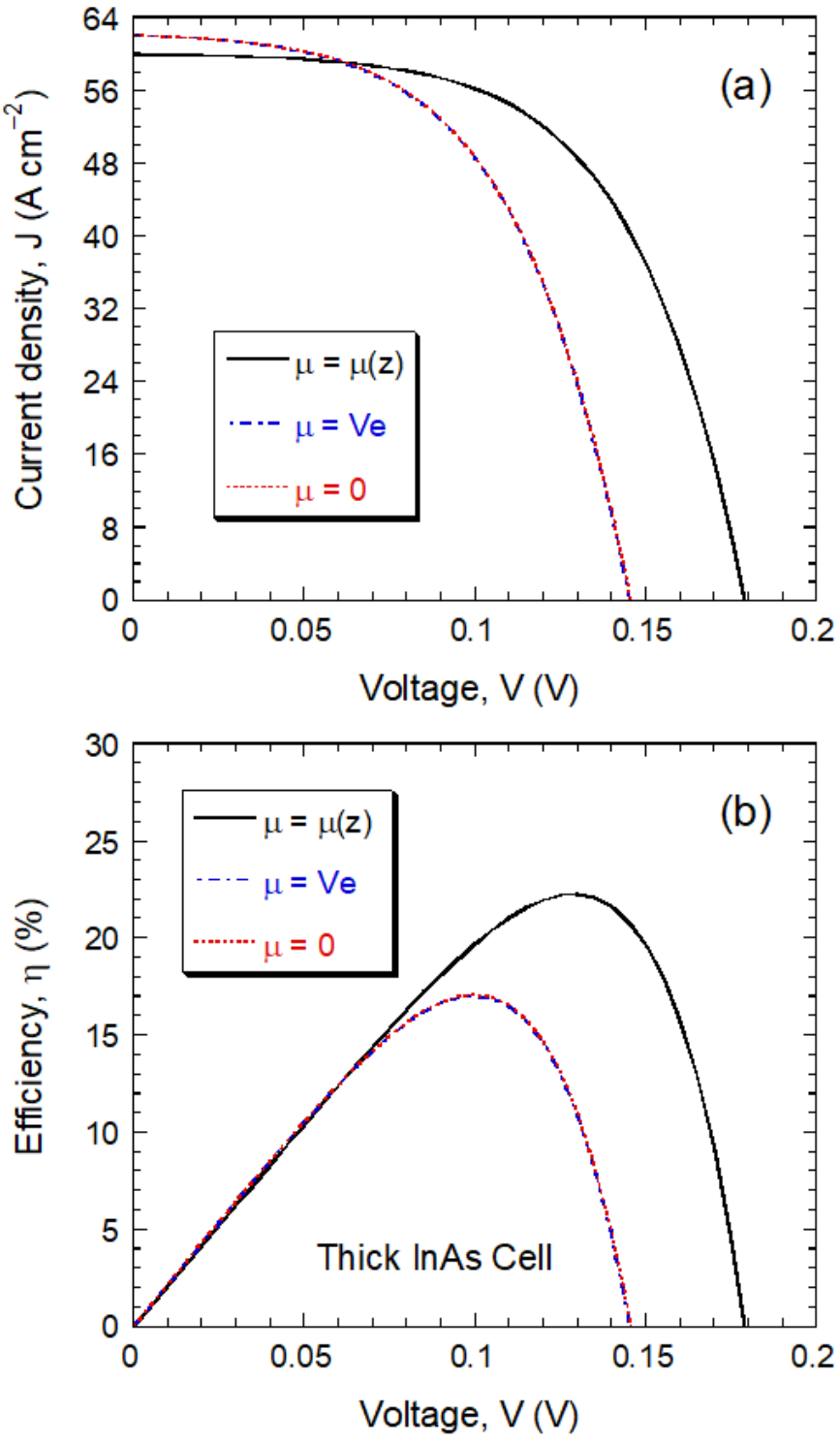

Figure 4.10 (a) Current density and voltage characteristics and (b) efficiency and voltage characteristics using three different treatments of the photon chemical potential profile for a thick InAs TPV cell.

the iterative method is much greater than 17.1% (at V = 0.1 V) obtained from detailed balance. The detailed balance analysis inherently assumes infinite charge diffusion coefficients and cannot capture the spatial variation of the charge concentration. Hence, the charge concentration at the surface is overpredicted, resulting in a higher surface recombination rate and a lower efficiency. It is important to consider the full charge transport processes in order to accurately predict the performance of near-field TPV devices.

For the thick cells under the short-circuit condition, $G_{cell} = 3.87 \times 10^{20}$ cm^{-2} s^{-1}, which is 3% higher than that for the thin cell and $Q = 28.5$ W cm^{-2}, which is 5% more than that for the thin cell. These values are comparable between the thin and thick TPV devices. The lower J and η with increased bias for the thick TPV device is due to the higher recombination rate in the thicker InAs cell. The enhancement of performance using thin-film TPVs has been suggested by Tong et al. [96].

It should be noted that all above results are presented for d = 10 nm cases only where the near-field effects on the photogeneration and radiation heat transport are very strong. Calculations have also been performed for larger gap distances. The effect of photon chemical potential can still be observed for d = 100 nm. However, the injection level decreases due to larger vacuum spacing. The influence of photon chemical potential diminishes as the vacuum spacing increases as expected. The error in the performance parameters becomes negligibly small (<5%) for larger (d > 100 nm) vacuum spacing. However, the exact criteria depend on the emitter temperature and materials used. The effects of photon chemical potential on thermophotovoltaic and thermoradiative cells have been recently studied in both near- and far-field regimes by Callahan et al. [82].

This work presents an iterative method to study near-field TPV devices that takes account of the luminescence effect based on FE with a modified Bose-Einstein distribution along with the full drift-diffusion model of the charge transport in the *p*-*n* junction. The spatial variation of the photon chemical potential is illustrated with two near-field InAs TPV cells operating at a vacuum gap distance of 10 nm. The results show that the detailed balance approach by ignoring the luminescence effect ($\mu = 0$) or by using a constant photon chemical potential ($\mu = Ve$) cannot properly describe the characteristics of both the thin and thick TPV devices and could cause 10-30% error in efficiency and output power when compared to the iterative solutions. This study demonstrates that the photon chemical potential is an important parameter in near-field semiconductor radiative energy converters and need to be carefully considered when the emitter is at a moderate temperature. A simple criterion is also introduced based on the percentage error of the emitted photons at the bandgap frequency that may give an initial estimate of the influence of μ for different semiconductor materials, with various bandgaps, at prescribed emitter and cell temperatures. The accurate modeling of the spatial profile of photon chemical potential provides researchers with a better understanding of photon-charge interactions in semiconductor *p*-*n* junctions, and moreover, it will benefit the design and development of TPV devices operating at nanoscale separation distances.

CHAPTER 5. PERFORMANCE ANALYSIS OF A NEAR-FIELD THERMOPHOTOVOLTAIC CELL WITH A BACK GAPPED REFLECTOR

In this Chapter, a thin-film InAs TPV device with a back gapped reflector (BGR) is investigated using a newly proposed photon-charge coupled iterative model from last Chapter. By comparing to a conventional metal back surface reflector (BSR) with different surface passivation conditions, the performance enhancement potential of this BGR is investigated for both far- and near-field regimes. The radiation exchange carried by propagating waves and evanescent waves are separately discussed for different vacuum spacings. The back gap thickness of the BGR is varied to optimize the efficiency of the InAs TPV device. The efficiency reduction, due to imperfect reflections at the semiconductor-metal interface, and output power loss, due to external luminescence and surface recombination, are also analyzed. Note, the loss mechanisms also depend on the back gap thickness of the BGR, which can potentially guide the design and optimization of TPV devices with higher efficiency and larger output power.

5.1 Overview of the Back Reflectors Structure within a TPV device

A back reflector is a common way to improve the performance of a TPV device by increasing the interband absorption while recycling photons below the bandgap energy [112, 190]. Two different BSRs were investigated for a far-field Ge TPV cell by Fernandez *et al*. [191]. The proposed dielectric BSR can feature high infrared reflection and excellent surface passivation of the backside of Ge TPV cells; however, the effect of the absorption

of BSRs on the TPV performance has not been discussed. A parametric study on the effects of a BSR and surface recombination on a near-field InGaSb TPV device was performed by Bright *et al.* [112]. This parametric study used a combined model that neglected the near-field effects on the dark current and internal luminescence, which might be important for certain TPV devices [81, 83]. Recently, Fan *et al.* [192] proposed a thin-film TPV cell design with a BGR, which can greatly enhance the performance of a far-field InGaAs TPV device by reducing the absorption in the back reflector. Inoue *et al*. investigated the performance improvement of non-contact reflectors on both sides of a Si-based TPV device [193]. Similar structures have not been applied to near-field thin-film TPV devices, which may see even greater improvements in device performance.

5.2 Geometric Structure and device parameters of a InAs Near-Field TPV device

A thin-film InAs TPV device with a BGR (TPV-BGR) is shown in Figure 5.1(a), which is compared with a TPV device with a conventional BSR (TPV-BSR) shown in Figure 5.1(b). A vacuum gap with a variable thickness (d) separates the tungsten emitter and InAs TPV cell. The tungsten emitter is modeled as an infinitely thick bulk with temperature at T_e = 900 K. The p-doped and n-doped InAs layers with thicknesses of $d_p = d_n$ = 200 nm, are respectively subdivided by a 50-layer nonuniform mesh to consider the localization effect on photogeneration and photon chemical potential [83]. Au is used for both BGR and BSR, and the thickness d_{Au} is chosen to be 100 nm to ensure all incident photons are reflected or absorbed. The front metal grid and the back metal grid are ignored in the radiation exchange due to the low shading area (less than 5%). The back metal grid in the BGR structure is used to support the vacuum gap between the cell and the back reflector. Consequently, the series resistance of the grid and the busbar is ignored in the charge

transport model. The temperature of the InAs cell (including BSR or BGR) is assumed to be room temperature, $T_c = 300$ K. Both devices require a vacuum environment to minimize the convection between the emitter and cell.

Since this near-field TPV device is similar to that in Chapter 4 (removing the ITO emitter), the optical and electrical properties can be found in Chapter 4. The iterative solver of the photon-charge coupled modeling method has also been detailed introduced in Chapter 2 and 4. Only the difference and improvement of the modeling method would be emphasized here. The net rate of absorbed energy of layer j from the tungsten emitter can be calculated by

$$Q_j = \sum_{m}^{emitter} \int_0^{\infty} \hbar\omega \left[\Psi\left(\omega, T_m, \mu_m\right) - \Psi\left(\omega, T_j, \mu_j\right) \right] \Upsilon_{mj}(\omega) d\omega \qquad (5.1)$$

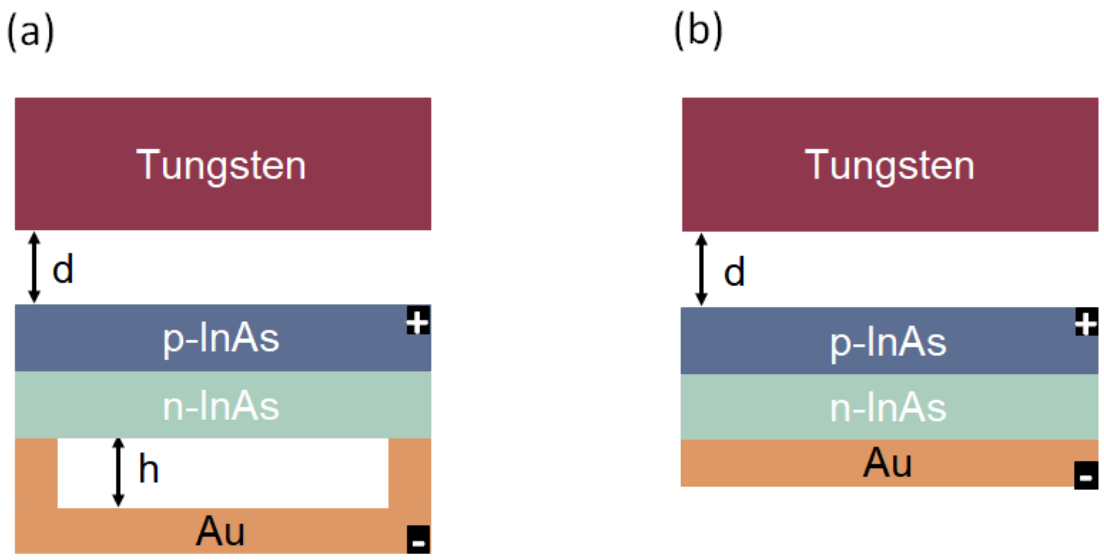

Figure 5.1 Schematic of an InAs TPV device with (a) a BGR and (b) a conventional BSR. Here, d is the vacuum spacing between the emitter and the cell, and h is the back gap thickness. The TPV cell includes the InAs and the back reflector.

The total absorbed power for a practical TPV device should include the absorption by the back reflector, since extra work is required to remove this parasitic heating. Therefore, the conversion efficiency is calculated by

$$\eta(V) = \frac{J(V)V}{Q_{\text{cell}}}, \text{ where } Q_{\text{cell}} = \sum_{j}^{\text{cell}} Q_j \tag{5.2}$$

Here, the summation is over the InAs layers and the back reflectors. Therefore, the absorbed power of the Au layer is taken into account in calculating the efficiencies.

To distinguish the two vacuum gaps in the device, the vacuum spacing represents the distance between the emitter and cells; while the gap thickness refers to the distance between the cell and the back reflector. In the following, the vacuum spacing is chosen as $d = 1$ mm or $d = 10$ nm to investigate the effect of this BGR on the TPV device under either the far- or near-field regime, respectively. The gap thickness of BGR is represented by h, which is parametrically swept between 10 nm to 10 μm. The maximum efficiency and maximum output power are calculated as a function of the gap thickness of BGR for both working regimes. Surface passivation conditions can potentially affect the performance of TPV devices [80, 112, 191, 194]. A well-passivated surface usually has large surface recombination velocity for majority carriers and small surface recombination velocity for minority carriers [163]. The surface recombination velocity for majority carriers is set to be an extremely large number, e.g., 10^9 cm/s. The surface recombination velocity for

Table 5.1. Surface recombination velocities for each TPV cell

TPV cells	$S_{e,p}$ (cm/s)	$S_{h,p}$ (cm/s)	$S_{e,n}$ (cm/s)	$S_{h,n}$ (cm/s)
Passivated BSR/BGR	10^2	10^9	10^9	10^2
Non-passivated BSR/BGR	10^2	10^9	10^9	10^4

minority carriers can vary from 10^2 cm/s to 10^4 cm/s or larger depending on surface passivation conditions [188]. Practically speaking, a well passivated surface usually requires an additional layer, several nanometers in thickness, of the selected dielectrics. For simplicity, this additional passivation layers is neglected when modeling the passivated TPV configurations. In this paper, 10^4 cm/s and 10^2 cm/s are used to represent a non-passivated surface and a passivated surface, respectively. By comparing the BGR with the BSR under the same passivation condition, the effect of the external luminescence loss can be explicitly distinguished from that of surface passivation. The front surfaces of four calculations are all assumed to be well-passivated. The surface recombination velocities for each TPV cell are listed in Table 5.1.

5.3 Performance Improvement by the Back Gapped Reflector

5.3.1 Output Electric Power and Photogeneration Rate

We first investigate a far-field TPV device with a 1 mm vacuum spacing. The effects of the back reflectors and surface passivation on the current density and voltage characteristic curves (i.e., the *J-V* curve) of this TPV cell are shown in Fig. 2a. The passivated TPV devices exhibit better *J-V* curves than those with a non-passivated condition. The generated current recombines at the non-passivated surface; a passivated TPV has a larger generated current than that of the non-passivated TPV. Under the same passivation conditions, the performance of TPV-BGR exceeds that of TPV-BSR. The working voltage of the passivated TPV-BGR is 0.062 V, which is 0.008 V larger than that of the passivated TPV-BSR. Hence, the passivated TPV-BGR can provide a maximum output power of 0.0061 W/cm^2, which is 38% larger than that of the passivated TPV-BSR.

The performance enhancement can be explained by plotting the spectral photogeneration rates of these TPV devices shown in Figure 5.2(b). The spectral photogeneration rate of

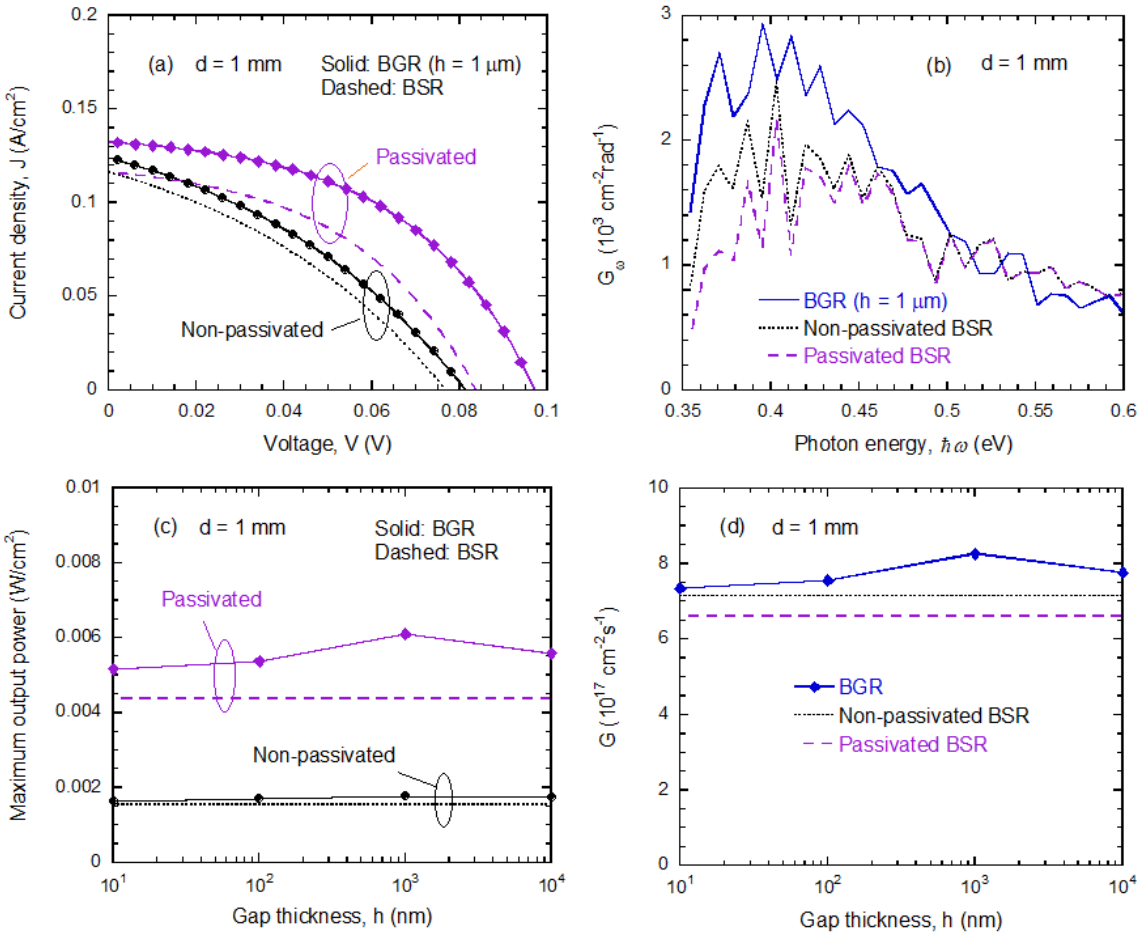

Figure 5.2 (a) Current density and voltage characteristic curve and (b) spectral photogeneration rate of TPV-BSR and TPV-BGR (h = 1 μm) with different passivation conditions when d = 1 mm. (c) Maximum output power and (d) total net photogeneration rate as a function of the gap thickness of a TPV cell with different back reflectors and passivation conditions when d = 1 mm. To be noted for Figure 5.2 and 5.3, the spectral photogeneration rate and total net photogeneration rate are calculated at the maximum output power condition for each TPV device. The BGR curves in Figure 5.2b, 5.2d, 5.3b and 5.3d represent both the passivated and non-passivated TPV-BGR.

TPV-BGR is larger than that of TPV-BSR for both passivated and non-passivated condition. The enhanced spectrum of the photogeneration rates of TPV-BGR compared to that of TPV-BSR is 0.354 eV to 0.5 eV, because the external luminescence losses of TPV-BGR are greatly reduced. Moreover, the reflections at the semiconductor-vacuum interface of TPV-BGR is more efficient than those at the semiconductor-metal interface of TPV-BSR, since fewer photons above the bandgap energy are absorbed by the back metal. Note that the passivation condition has little effect on the photogeneration rate of TPV-BGR since external luminescence is minimized in this structure.

The maximum output power and photogeneration rate of four far-field TPV configurations as a function of the gap thickness are shown in Fig. 2c and 2d. As is clearly shown in Fig. 2c, the maximum output power of TPV-BGR slightly increases to a saturated value as the gap thickness increases. The enhancement effect on the output power of the TPV-BGR is demonstrated by comparison with TPV-BSR. The maximum output power of TPV-BGR is 15%-40% higher, compared to TPV-BSR for the passivated condition. Although the maximum output power of the non-passivated condition is reduced by almost one third of the passivated condition, the maximum output power of TPV-BGR is 5%-15% larger than that of TPV-BSR for the non-passivated condition. Enhanced total net photogeneration rate and a well-passivated surface can greatly improve the maximum output power of a TPV device. Shown in Fig. 2d, the total net photogeneration rate of TPV-BGR exhibits a similar trend as Fig. 2c. As the total net photogeneration rate increases with the gap thickness, more free electrons and holes are generated in the TPV cell, which produces a larger output power than that of TPV-BSR. The total net photogeneration rate of TPV-BGR (passivated/non-passivated) is 10%-25% greater than that of the passivated

TPV-BSR and 3%-15% larger than that of the non-passivated TPV-BSR. The enhancement effect on the total net generation rate of the passivated TPV-BGR is lower than that on the maximum output power, which is due to external luminescence at different photon chemical potentials. The total net photogeneration rate of InAs can be expressed by subtracting external luminescence from the net photogeneration rate between the emitter and the InAs. A good surface passivation would result in a larger photon chemical potential, which can result in a larger external luminescence. Although the total net photogeneration rate of the non-passivated TPV-BSR is larger than that of the passivated TPV-BSR, the generated free carriers in the non-passivated TPV-BSR recombine at the surfaces. Therefore, the passivated TPV-BSR has better performance than the non-passivated case. In summary, TPV-BGR with good passivated surfaces can definitely enhance the maximum output power at the far-field regime for different gap thicknesses.

The *J-V* curves and spectral photogeneration rates of a near-field TPV device with different back reflectors and passivation conditions are shown in Figure 5.3(a) and 5.3(b) Although the difficulty of fabricating a near-field TPV device with two 10 nm vacuum gap is incredible, the back gap thickness of TPV-BGR is chosen to be 10 nm for numerical demonstration purposes. As shown in Figure 5.3(a), the open circuit voltages of the passivated TPVs are larger than that of the non-passivated TPVs. The surface recombination effects become more significant in the near-field case because a larger current density is generated and more free carriers recombine at the non-passivated surfaces. The working voltage of the passivated TPV-BGR is 0.143 V, which is 0.007 V larger than that of the passivated TPV-BSR. Hence, the passivated TPV-BGR exhibit a maximum output power of 0.63 W/cm^2, which 8% larger than that of the passivated TPV-

BSR. Unlike the far-field case, the enhancement of the *J-V* curve by replacing a BSR with a BGR is rather limited, because the photogeneration rate is dominated by the near-field radiation, which is not sensitive to the structure of the back reflectors. As shown in Figure 5.3(a), a well-passivated surface can greatly improve the maximum output power by

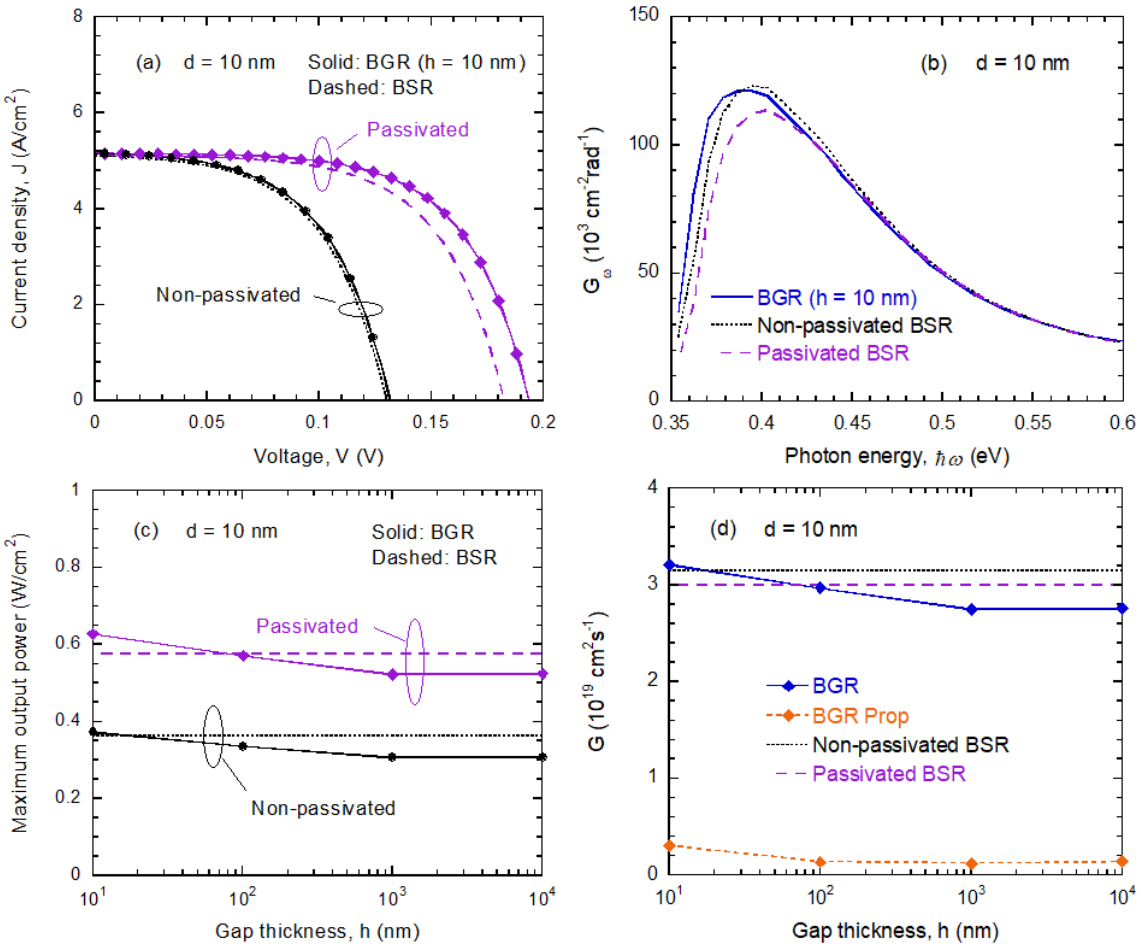

Figure 5.3 (a) Current density and voltage characteristic curve and (b) spectral photogeneration rate of the TPV-BSR and TPV-BGR (h = 10 nm) with different passivation conditions when d = 10 nm. (c) Maximum output power and (d) total net photogeneration rate as a function of the gap thickness of a TPV cell with different back reflectors and passivation conditions when d = 10 nm.

increasing the open-circuit voltage for both the TPV-BGR and TPV-BSR. As shown in Figure 5.3(c), the maximum output power of the TPV-BGR decreases as the gap thickness increases for both passivated and non-passivated conditions. Whether TPV-BGR can provide enhancement on the maximum output power compared to TPV-BSR depends on the gap thickness. The largest enhancement provided by TPV-BGR is when the gap thickness equals 10 nm. The maximum output power generated by TPV-BGR has an 8% enhancement compared to that of the passivated TPV-BSR. In addition, the maximum improvement of TPV-BGR is reduced to 2.5% for the non-passivated condition. The surface passivation effect on the maximum output power is more dominant than the effect brought by the back reflector structure. The trend of the maximum output power of TPV-BGR matches well with the total net photogeneration rate, shown in Figure 5.3(d). Unlike the far-field condition, the reduction of the total net photogeneration rate as the gap thickness increases is not only due to the propagating photons but also the frustrated photons, which is represented by the difference between BGR and BGR Prop in Figure 5.3(d). As the gap thickness increases, the destructive absorption pattern causes a slight decrease in the total net photogeneration for the near-field condition. To summarize the effect of the gap thickness for the near-field condition, a BGR with a small gap thickness (comparable to vacuum spacing) is preferred for larger output power.

5.3.2 Efficiency and Cell Absorbed Power

The improvement of maximum conversion efficiency brought by the BGR structure is clearly shown in Figure 5.4. TPV-BGR exhibits improvement to the maximum conversion efficiency of TPV devices. As seen in Figure 5.4(a), the conversion efficiency using a BGR is 1.05-1.34 times higher than that using a BSR for non-passivated condition.

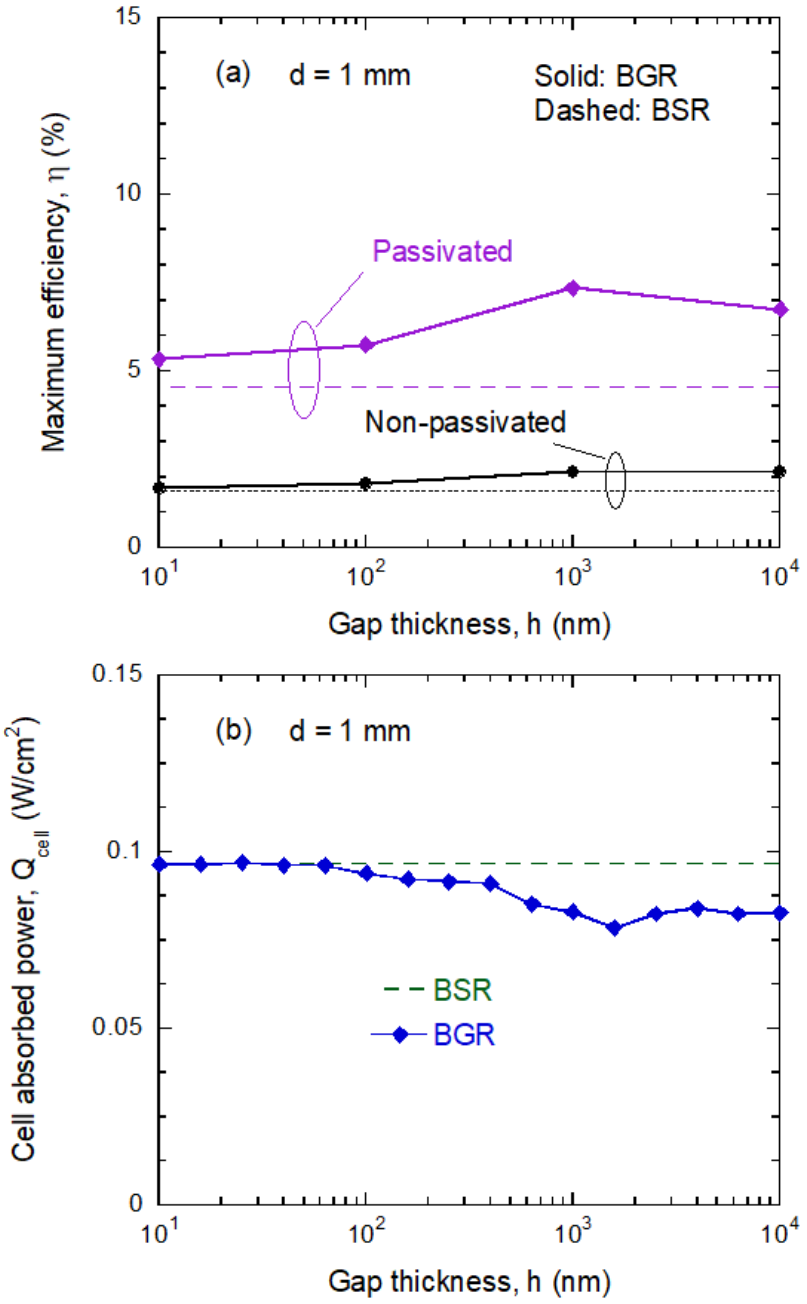

Figure 5.4 (a) Maximum conversion efficiency and (b) cell absorbed power as a function of the gap thickness for TPV devices with different back reflectors and passivation conditions when d = 1 mm. The surface passivation has little effect on the cell absorbed power, therefore, the BGR and the BSR represent both the passivated and non-passivated conditions in Figure 5.4(b) and 5.5(b).

The passivated TPV-BGR maximum efficiency ranges between 5.7%-7.4%, which is a 1.18-1.62 times higher than that of the passivated TPV-BSR when the gap thickness increases. This enhancement in efficiency is higher than that of the output power (15%-40%) indicating that the efficiency improvement is a coupled effect of the output power enhancement and parasitic absorption reduction. As clearly shown in Figure 5.4(b), the cell absorbed power is inversely correlated with the maximum efficiency as the gap thickness increases. The reduction effect on cell absorbed power can be clearly seen by the difference between BGR and BSR. The cell absorbed power is dominated by the emission from the emitter, where the temperature is fixed at 900 K. The external luminescence from the InAs to vacuum at the back is negligible. Therefore, the passivated conditions have little effect on the cell absorbed power for both TPV-BSR and TPV-BGR. The same conclusion can be drawn for the near-field condition.

For the near-field condition shown in Figure 5.5(a), the passivated TPV-BGR has an 18%-21% maximum conversion efficiency when the gap thickness increases, which is higher than the 16.4% for the passivated TPV-BSR. For the non-passivated scenario, TPV-BGR also possesses a 1.08-1.19 times improvement when compared with TPV-BSR. As manifest in Fig. 5a, the maximum efficiency of TPV-BGR increases by increasing the gap thickness. Since the maximum output power of TPV-BGR is not a strong function of the gap thickness, the cell absorbed power of TPV-BGR should be inversely proportional to gap thickness to match the efficiency enhancement, which is exactly the trend of TPV-BGR shown in Figure 5.5(b). Compared to the propagating modes represented by the dashed-diamond curve, the cell absorbed power of TPV-BGR carried by the frustrated modes (the difference between the BGR and BGR Prop) is largely reduced in the near-field

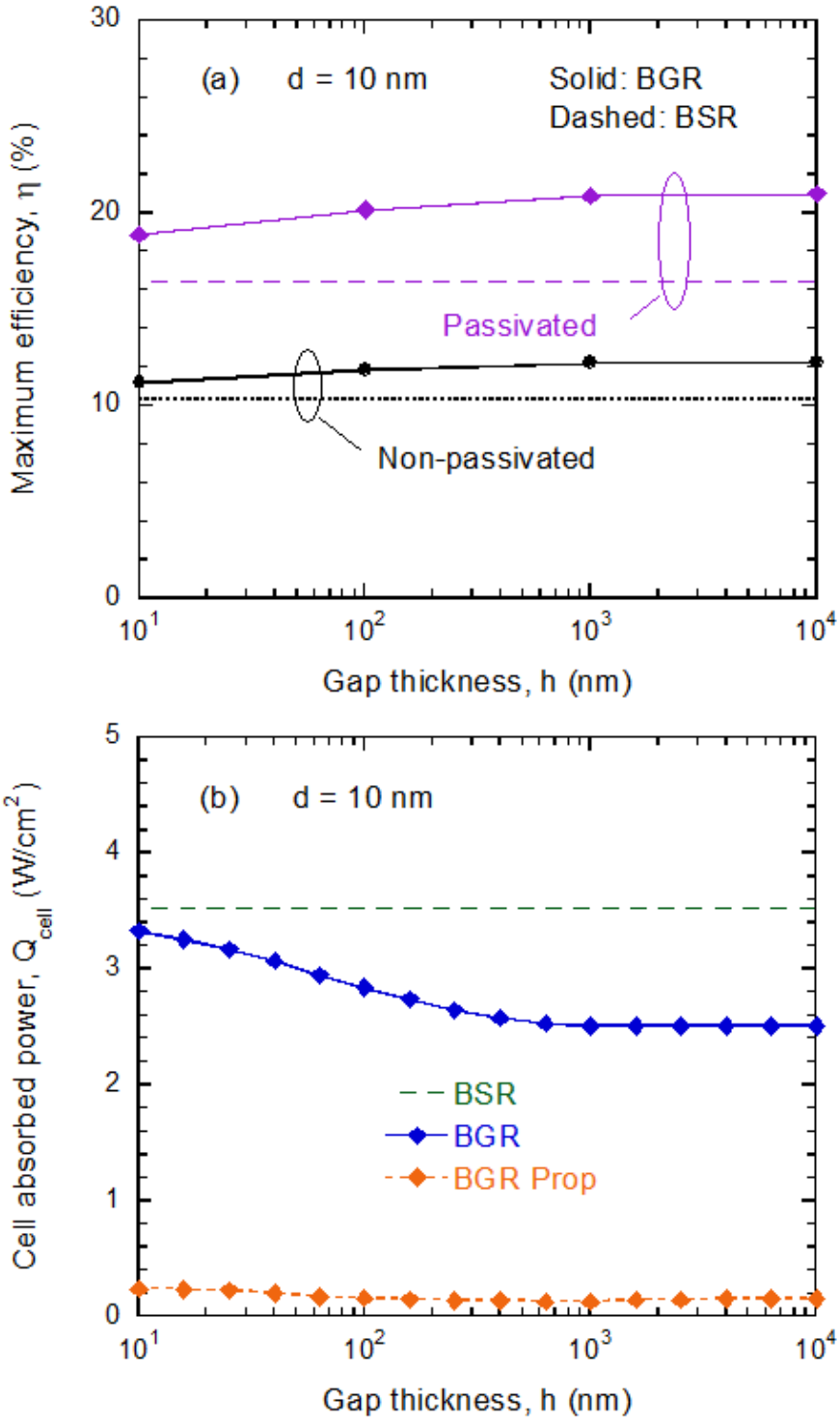

Figure 5.5 (a) Maximum conversion efficiency and (b) cell absorbed power as a function of the gap thickness for TPV devices with different back reflectors and passivation conditions when d = 10 nm.

scenario. Near-field radiation dominates the radiation exchange between the emitter and cell, as the vacuum spacing decreases from Figure 5.4(b) (d = 1 mm) to Figure 5.5(b) (d = 10 nm). The efficiency enhancement brought by the BGR structure is apparently large.

5.3.3 Imperfect Reflections and External Luminescence Loss

The generated power can be enhanced by adding a conventional metal BSR to a TPV cell [75, 112, 191]. An ideal back reflector reflects all incident photons. However, a perfect mirror for photons of all wavelengths does not exist. The absorption of the back reflector occupies a significant amount of the parasitic absorption, which requires extra cooling power to maintain the TPV cells at a comfortable temperature range. Therefore, it is important to minimize the parasitic absorption of TPV cells. When light transmits through the semiconductor-metal interface of a TPV-BSR, the reflection is not perfect because most of the electromagnetic waves can easily transmit from an optically rare medium to an optically dense medium. However, by adding a gap between the semiconductor and the back reflector, most of the propagating photons reflect perfectly at the semiconductor-air interface through total internal reflection. However, if the gap thickness is comparable to or less than the wavelength of transmitted photons, the photon tunneling effect would also be present between the semiconductor and the back metal. Therefore, the gap thickness is required to be larger than the characteristic wavelength to avoid photon tunneling effects and to minimize the absorption of the back reflector. In Figure 5.6(a) and 5.6(b), it is shown that the absorption in the BGR decreases significantly as the gap thickness increases for both far- and near-field regimes. When one compares the absorbed power of the metal in Fig. 6a with the cell absorbed power in Figure 5.4(b) for TPV-BGR, the percentage of the absorbed power of the metal over the cell absorbed power

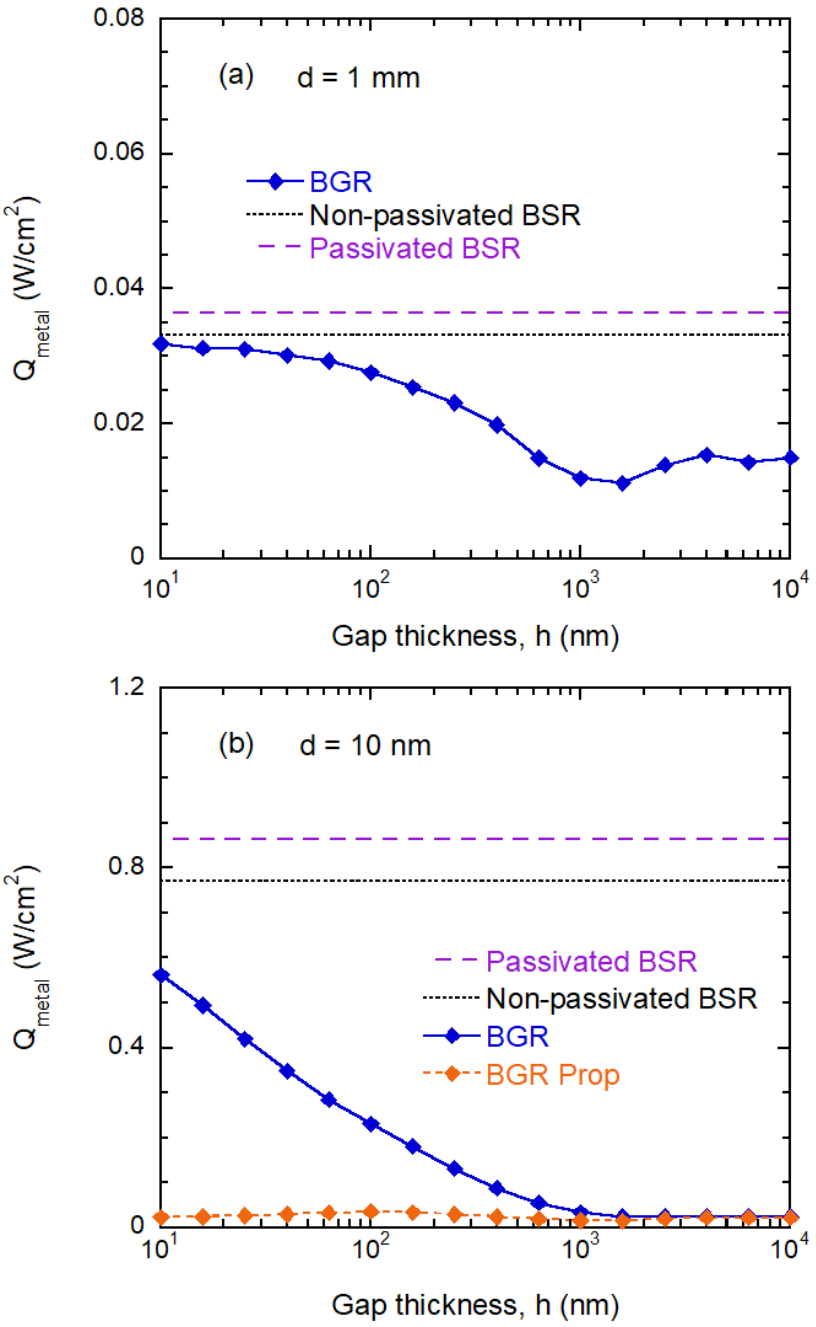

Figure 5.6 The absorbed power of the back metal (Q_{metal}) as a function of the gap thickness for TPV devices with different back reflectors when (a) d = 1 mm and (b) d = 10 nm. To be noted, the BGR and BGR Prop represent both passivated and non-passivated condition since the surface passivation condition has little effect on the absorbed power of the metal.

is reduced from 38% to 14% when the gap thickness is increased from 10 nm to 1 μm. Hence, increasing the gap thickness of the BGR structure can greatly reduce the metal absorption to improve the performance of a far-field TPV device. As the gap thickness increases from 10 nm to 1 μm (or larger) in the near-field TPV-BGR in Figure 5.6(b), the percentage of the absorbed power of the metal over the cell absorbed power is reduced from 17% to 1% and the absorbed power carried by the frustrated modes are almost reduced to zero. This indicates that a TPV-BGR with a larger back gap can effectively reduce the absorption of the metal. Note that thermal radiation from the emitter and external luminescence from the InAs both contribute to the absorption of the back metal. The absorption of the metal in the BGR structure is not affected by the passivation condition because the incoming thermal radiation is dominating the absorption of the metal and external luminescence has been minimized with the TPV-BGR. However, the surface passivation conditions do affect the operating voltages of TPV-BSRs as shown in Figure 5.2(a) and 5.2(b), and external luminescence is exponentially related with the photon chemical potential, which is equal to the operating voltage times the elementary charge at low-level injection condition [83]. Therefore, the metal absorbs more power due to a higher external luminescence in the passivated TPV-BSR than the non-passivated case. This is shown for both far- and near-field condition in Figure 5.6(a) and 5.6(b), respectively.

The spectral absorbed powers of the metal in different TPV configurations provides more information about the reduction of the parasitic absorption, which are shown in Fig. 7a and 7b. For both far-and near-field TPV devices, two key comparisons should be carefully considered: TPV-BSR versus TPV-BGR and passivated TPV-BSR versus non-passivated TPV-BSR. For the far-field condition shown in Figure 5.7(a), the spectral

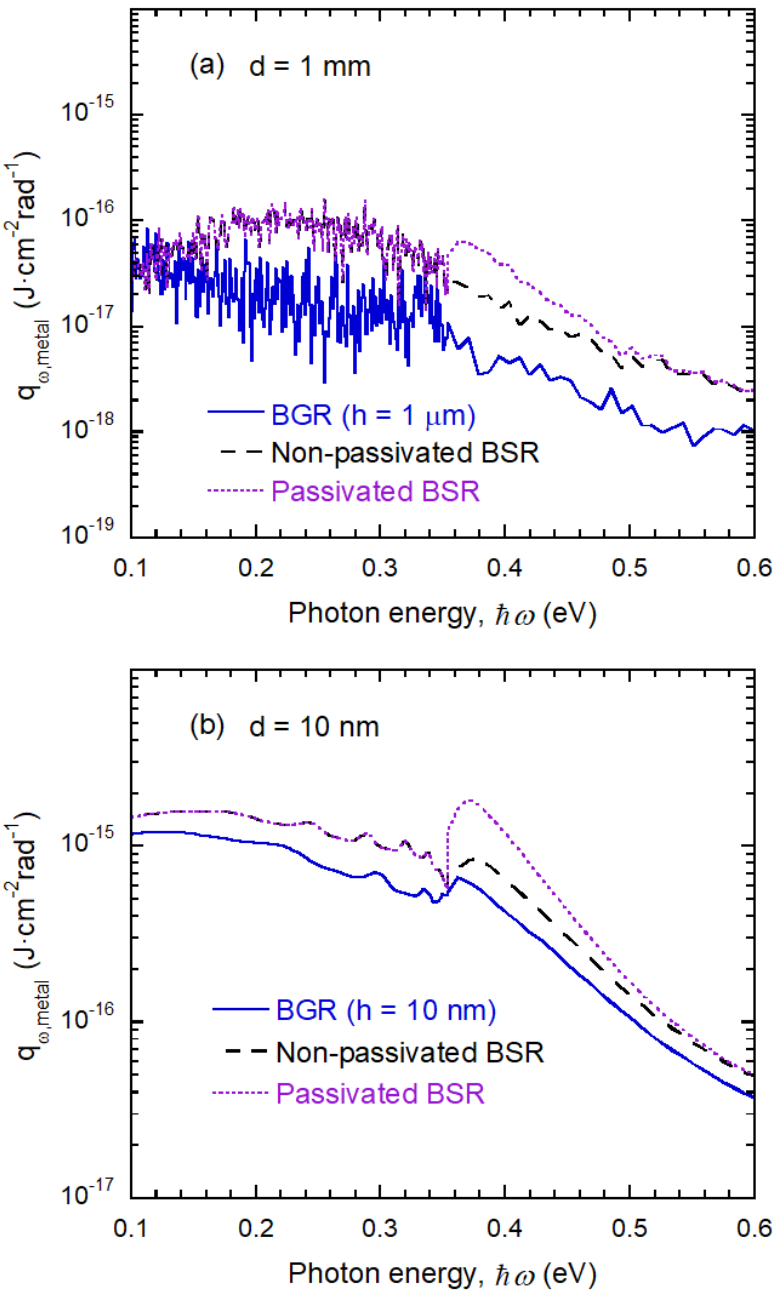

Figure 5.7 (a) Spectral absorbed powers of the metal in the TPV-BGR (h = 1 μm) and TPV-BSR when d = 1 mm. (b) Spectral absorbed powers of the metal in the TPV-BGR (h = 10 nm) and TPV-BSR when d = 10 nm. The passivation condition has little effect on the spectral absorbed power of the TPV-BGR so that the BGR curves in both Fig. 7a and 7b represent the passivation and non-passivated conditions.

absorbed power of the metal in the non-passivated TPV-BGR is lower than that in the non-passivated TPV-BSR, because the photon tunneling from the InAs region to the metal is suppressed for photons of all wavelengths. The spectral absorbed power of the metal in the non-passivated TPV-BSR overlaps with the passivated TPV-BSR below the bandgap energy, since the absorption of the sub-bandgap photons is not related with surface passivation but the TPV structures. The external luminescence loss happens at the spectrum above the bandgap. The passivated TPV-BSR has greater external luminescence losses than the non-passivated case due to larger operating voltage. Therefore, the spectral absorbed power in the metal is larger for the photons above bandgap energy. The same conclusion can be drawn for the near-field condition shown in Fig. 7b. For both far- and near-field, the TPV-BGR can greatly reduce the absorption of the back reflectors, which is the key mechanism to improve the efficiency of a TPV device.

In a working TPV cell, the more electron and hole pairs are generated, the more likely they will recombine and generate external luminescence, similar to a biased LED [81, 83, 195]. The energies of luminescent photons are larger than bandgap. It is illustrated that the external luminescence intensity from a working TPV cell is exponentially proportional to the photon chemical potential, which is usually assumed to be equal to the product of the working voltage and elementary charge. The luminescent photons from the cell cannot be recycled when they are absorbed by any object other than the emitter and cell; this is called external luminescence loss. As one of the major loss mechanisms that deteriorates the performance of TPV devices working at moderate temperatures, the

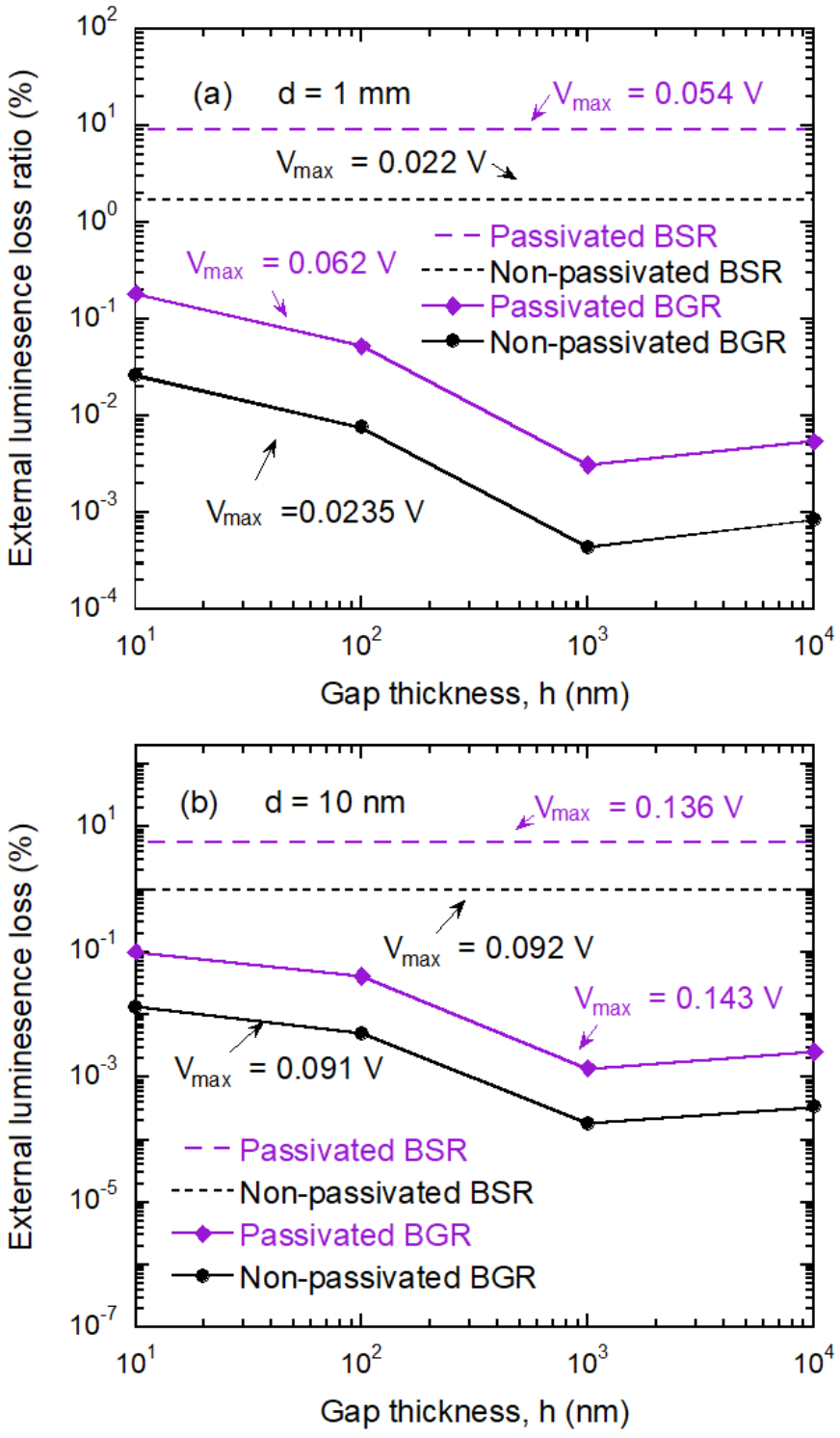

Figure 5.8 External luminescence loss ratio as a function of the gap thickness for TPV devices with different back reflectors when (a) d = 1 mm and (b) d = 10 nm at the maximum output power voltage.

external luminescence loss can also be minimized by the BGR structure. As shown in Figure 5.8(a), at the maximum output power voltage (V_{max}), the passivated TPV-BGR at V_{max} = 0.054 V would emit ~10% photons of the total net photogeneration rate at the same condition. The external luminescent photon rate over the total net photogeneration rate is called external luminescence loss ratio. Due to the dominant effects of surface recombination in the non-passivated TPV-BSR, V_{max} is only 0.022 V, which is much less than that of the passivated TPV-BSR. Nevertheless, a 2% external luminescence loss ratio still exists in the non-passivated TPV-BSR. However, the external luminescence loss can be reduced to 1% of the total net photogeneration rate by introducing a 10 nm gap between the semiconductor and the back reflector. As the gap thickness increases, the external luminescence loss ratio can be reduced to less than 0.01%. Similar trends are exhibited in Figure 5.8(b). The external luminescence loss ratio can be effectively reduced to zero by the BGR structure for both the passivated and non-passivated condition. Although V_{max} increases when the vacuum spacing reduces, the BGR structure can still reduce the external luminescence losses to negligible levels. Moreover, when the emitter temperature increases, the TPV devices will be working at a higher voltage, which means a larger external luminescence would occur. Therefore, minimizing the external luminescence loss become even more critical at high emitter temperatures and the BGR structure is definitely useful in creating a high-performance TPV device.

5.3.4 Effect of the Vacuum Spacing on the Performance of TPV Devices

To study the effect of the vacuum spacing on the TPV with different back reflectors, a parametric analysis on the vacuum spacing is performed for the four TPV devices. To clearly show the effect of the BGR structure on the performance of TPV devices, the back

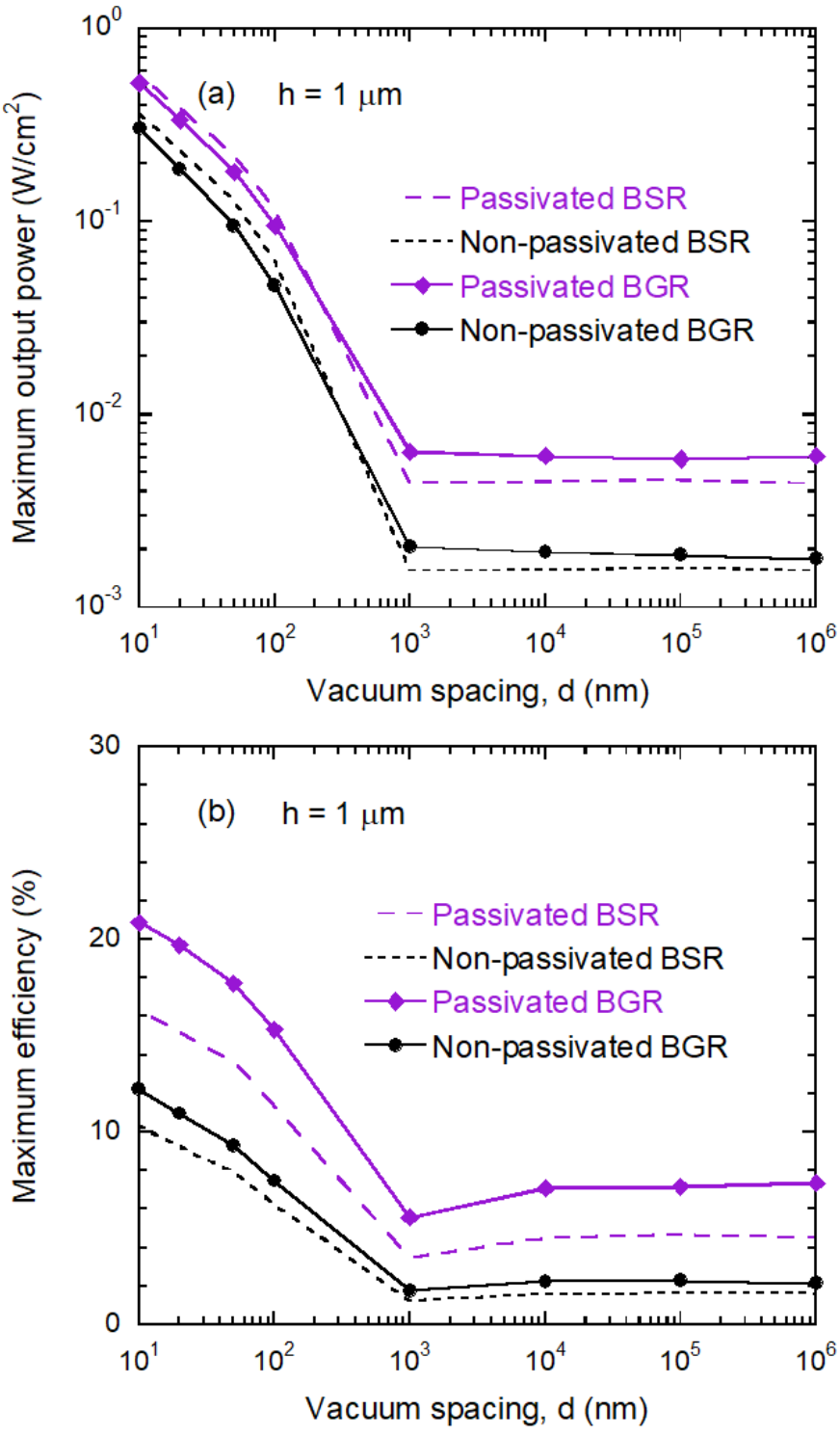

Figure 5.9 (a) Maximum output power and (b) maximum efficiency as a function of the vacuum spacing of a TPV cell with different back reflectors and passivation conditions. The gap thickness of the TPV-BGR is fixed at h = 1 μm.

gap thickness is fixed at 1 μm, which is feasible for current fabrication technologies. In general, the maximum output powers and maximum efficiency of all TPV devices decrease as the vacuum spacing increases shown in Fig. 9a and 9b. The passivated cases exhibit better maximum output powers than the non-passivated cases. The maximum output power of TPV devices can be improved by replacing the BSR with the BGR (h = 1 μm) when the vacuum spacing is larger than hundreds of nanometers. When the vacuum spacing is in the near-field regime (d < 100 nm), TPV-BGR does not provide higher output powers when compared with the TPV-BSR. However, the maximum efficiency of TPV devices can benefit from the BGR structure for both far- and near-field regimes. In summary, the BGR structure can improve the performance of the far-field TPV devices; while in the near-field condition, the back gap thickness should be carefully chosen to simultaneously increase the maximum output power and efficiency of TPV devices.

CHAPTER 6. LOCAL RADIATIVE RECOMBINATION IN THIN-FILM RADIATIVE ENERGY CONVERTERS

In this work, the total external radiative recombination coefficient was calculated by fluctuational electrodynamics (FE) apparently diverges from that by van Roosbroeck-Shockley when the cell thickness is less than 10 μm. A 400 nm InAs cell is configured with different geometric structures to illustrate the spatial effect on the external radiative recombination. The spatial profile of the local external radiative recombination coefficient can be significantly modified due to photon recycling in the far field and photon tunneling in the near field. In addition, the local external radiative recombination coefficient reduces as the local doping level approaches that of a degenerate semiconductor. Intrinsic internal quantum efficiency (IIQE) is newly defined to distinguish the thermal radiation and nonthermal radiation quantitatively. The ideal IIQE assumption leads to an overprediction of the maximum power density and maximum efficiency of a near-field thin-film thermoradiative cell for more than 10% compared to the result by using a real IIQE.

6.1 Overview of the External Luminescence of Radiative Energy Converters

Following the thin-film trend of optoelectronic device industries such as photovoltaic (PV) cells and light emitting diodes (LEDs), near-field radiative energy converters can also benefit from reducing the thickness of active materials in a cell or a refrigerator. Although the volumetric absorption or emission is proportional to the thickness of active materials, the nonradiative losses, such as Auger and Shockley-Read-Hall (SRH) processes, are also reduced by thinning the active materials. Moreover, the near-field effect on the local

absorption and emission due to surface electromagnetic resonance can only penetrate a small skin depth of the active materials [2, 196]. By optimizing the thickness of a cell or a refrigerator, thin-film structures are usually preferred for near-field radiative energy converters [8, 9].

Neglecting the nonradiative processes, the radiative recombination and photon absorption are the main optical processes in radiative energy converters. By applying the principle of detailed balance, radiative recombination of nonequilibrium semiconductor diodes can be depicted by van Roosbroeck-Shockley model [173, 197]. Thereafter, Wurfel proposed a more precise expression, which is using a modified Bose-Einstein distribution derived from Fermi-Dirac distribution of free carriers in nonequilibrium semiconductor [1]. Trupke *et al.* summarized a general expression of external radiative recombination considering the multiple reflections from the front and back interfaces [198]. Although thin-film near-field radiative energy converters possess the same working mechanism as regular PV cells and LEDs, whether the conventional model can be applied required a rigorous investigation. DeSutter *et al.* investigated the external luminescence (external radiative recombination) and photon recycling in a near-field TPV cell using FE [79]. However, the linkage between van Roosbroeck-Shockley model and FE is not explicitly discussed.

In this work, the external radiative recombination coefficient (ERRC) calculated by FE is compared with generalized van Roosbroeck-Shockley model to show the thin-film effect. The local ERRC represents the capability of generating or absorbing a photon at a given location. Geometric effect on the local ERRC is also studied for a thin-film radiative energy converter working at different configurations. The doping effect on the local ERRC due to Moss-Burstein shift is emphasized for the radiative energy converters made of direct

narrow bandgap semiconductors. Wurfel theoretically distinguished the thermal radiation and nonthermal radiation (radiative recombination) by introducing the photon chemical potential [1], and Karalis and Jonannopoulos quantitatively distinguish the thermal and nonthermal contributions of photon absorption and emission to the performance of a near-field TPV using temporal coupled-mode theory [87]. With the newly proposed concept of intrinsic internal quantum efficiency (IIQE), the spectral intensity of thermal radiation and non-thermal radiation for a near-field TR cell is calculated using FE as an example. The performances of the near-field TR cell using two models are compared to indicate the importance of considering all the effect on the radiative recombination, which is a significant contribution on the modeling of thin-film near-field radiative energy converters. For simplicity, the following investigations are mainly performed for TPVs and TRs. However, the results of these configurations can be extended to other radiative energy converters without doubt.

6.2 Calculation of External Radiative Recombination

Combining the fluctuation-dissipation theorem (FDT) with Maxwell's equations, FE establishes the relation between the strength of the random fluctuations of the charges and local equilibrium status at a point source. With the assistance of the dyadic Green's function, the electric and magnetic fields are given by Eqs. (2.5) and (2.6) [2, 32].

Applying the Poynting theorem, the spectral thermal emission at a given z location for a given frequency ω is expressed as [2, 32]:

$$q_\omega(z) = 2\,\mathrm{Re}\left[\begin{array}{l}\dfrac{i\omega^2}{\pi c^2}\int_{\mathrm{V}} d\mathrm{V}'\int_{\mathrm{V}} d\mathrm{V}'' \\ \times\left(G_{xn}^{E}G_{ym}^{H*} - G_{yn}^{E}G_{xm}^{H*}\right)\left\langle J_m(\mathbf{r}',\omega)J_n(\mathbf{r}'',\omega)\right\rangle\end{array}\right] \tag{6.1}$$

where c is the speed of light in vacuum. G_{xn}^{E} and G_{ym}^{H} are the tensor components of the electric and magnetic dyadic Green's function, respectively. and m and n stand for the three orthogonal components ($m, n = x, y, z$). $J_n(\mathbf{r}', \omega)$ and $J_m(\mathbf{r}'', \omega)$ represent the fluctuating current at two different locations $\mathbf{r}'$ and $\mathbf{r}''$ in the emitting medium. $\langle\ \rangle$ and * denote the ensemble average and the complex conjugate operation.

If one can assign the equilibrium status (temperature and photon chemical potential etc.) and the contribution of the imaginary part of the permittivity to each excitation type (interband transition, phonon, and free carriers), the spatial correlation function of the fluctuating current is given by:

$$\left\langle J_m(\mathbf{r}', \omega) J_n^*(\mathbf{r}'', \omega') \right\rangle = \frac{\omega \varepsilon_0 \delta_{mn} \delta(\mathbf{r}' - \mathbf{r}'') W_{J_m, J_n}}{\pi} \tag{6.2}$$

where ε_0 is the permittivity of vacuum. δ_{mn} is the Kronecher function based on the isotropic medium assumption and $\delta(\mathbf{r}' - \mathbf{r}'')$ is the Dirac delta function due to the locality of dielectric function [32]. Assuming $\mathrm{Im}(\varepsilon) = \mathrm{Im}(\varepsilon_{\mathrm{ib}}) + \mathrm{Im}(\varepsilon_{\mathrm{nonrad}})$, the product of imaginary part of dielectric function and modified Bose-Einstein term can be rewritten as [199]:

$$\begin{aligned} W_{J_m, J_n} = {} & \mathrm{Im}\left[\varepsilon_{\mathrm{ib}}(\mathbf{r}'', \omega)\right] \Psi(\omega, T_{\mathrm{ib}}, \mu) \\ & + \mathrm{Im}\left[\varepsilon_{\mathrm{nonrad}}(\mathbf{r}'', \omega)\right] \Psi(\omega, T_{\mathrm{nonrad}}, 0) \end{aligned} \tag{6.3}$$

where $\varepsilon_{\mathrm{ib}}(\mathbf{r}'', \omega)$ and $\varepsilon_{\mathrm{nonrad}}(\mathbf{r}'', \omega)$ are the contribution to the imaginary part of the dielectric function due to interband transition and nonradiative absorption (phonons and free carriers), respectively. T_{ib} and T_{nonrad} are the local equilibrium temperature of where the interband transition and nonradiative absorption happen, respectively.

The modified Bose-Einstein distribution is used to model the emitted spectral photons, which is given by Eq. (2.10). Note that T in Eq. (2.10) is the temperature in local equilibrium condition and $\omega_{\mathrm{g}} = E_{\mathrm{g}}/\hbar$ is the frequency that corresponds to the bandgap energy (E_{g}).

Plug Eq. (6.2) into Eq. (6.1) and extract the component due to interband transition. The external radiative recombination of a thin film to the air can be written as [29]:

$$N_{\omega} = \Psi(\omega, T, \mu)\,\mathrm{IIQE}(\omega, T)\int_0^{k_0} \frac{dk_{\parallel}}{2\pi^2} \sum_{\gamma=s,p} \left(1 - \left|R^{\gamma}\right|^2 - \left|T^{\gamma}\right|^2\right) \tag{6.4}$$

where $\mathrm{IIQE}(\omega, T) = \mathrm{Im}\left[\varepsilon_{\mathrm{ib}}(\omega, T)\right] / \mathrm{Im}\left[\varepsilon(\omega, T)\right]$ is defined as the ratio of the number of photons emitted by interband transition to the number of total emitted photons. From the perspectives of absorption, the IIQE can also be understood as the ratio of the number of local generated electron and hole pairs due to interband transition to the number of total absorbed photon. R^{γ} and T^{γ} are the reflection and transmission coefficients of the thin film when light is incident from air. The superscript γ represents the polarization state of light (s or p). $k_0 = \omega/c$ is the vacuum wavevector. The parallel wavevector $k_{\parallel}$ is defined as $k_{\parallel}^2 = k_x^2 + k_y^2$.

Similarly, the spectral heat flux of thermal emission and nonthermal emission (external luminescence) can be calculated as follows, respectively:

$$q_{\omega,\mathrm{thermal}} = \hbar\omega N_{\omega}\left[1 - 1/\mathrm{IIQE}(\omega, T)\right] \tag{6.5}$$

and

$$q_{\omega,\mathrm{lum}} = \hbar\omega N_{\omega} \tag{6.6}$$

By applying Boltzmann approximation on the modified Bose-Einstein distribution in Eq. (6.4) and dividing Eq. (6.4) by the product of the local free carriers concentrations, the ERRC of a film can be written as:

$$B_{\mathrm{FE}} = \int_{\omega_{\mathrm{g}}}^{\infty} \frac{\mathrm{IIQE}\left(\omega, T\right)\exp\left(-\hbar\omega/k_{\mathrm{B}}T\right)}{n_{\mathrm{i}}\left(T\right)^{2} h} \times \int_{0}^{k_0} \frac{dk_{\|}}{2\pi^{2}} \sum_{\gamma=s,p} \left(1-\left|R^{\gamma}\right|^{2}-\left|T^{\gamma}\right|^{2}\right) d\omega \tag{6.7}$$

where n_{i} is the intrinsic carrier concentration of the semiconductor materials and h is the thickness of the cell. To be noted, the application condition of Boltzmann approximation depends on the injected carrier density and doping level of the semiconductor materials. The error of Boltzmann approximation has been discussed in detail in Ref. [81].

To study the local ERRC, a multilayer FE formalism is applied to a thin-film cell with a nonuniform mesh to calculate photon exchange between any semiconductor layer and external environment. Applying the similar method in Ref [83], the local ERRC is given by:

$$\begin{aligned} B\left(t\right) &= \int_{\omega_{\mathrm{g}}}^{\infty} B_{\omega}\left(t\right) d\omega \\ &= \int_{\omega_{\mathrm{g}}}^{\infty} \frac{\mathrm{IIQE}\left(\omega, T_j\right)\exp\left(-\hbar\omega/k_{\mathrm{B}}T_j\right)}{n_{\mathrm{i}}\left(T_j\right)^{2} h_j} \Upsilon_j(\omega) d\omega \end{aligned} \tag{6.8}$$

where t is the location of layer j in the cell. T_j and h_j are the temperature and thickness of layer j, respectively. Here, layer j is assumed at local equilibrium condition (temperature, dielectric function and photon chemical potential etc.). The function $\Upsilon_j(\omega)$ is the fraction of photon at a given frequency from layer j to external environment, which can be calculated as follows [83].

$$\Upsilon_j(\omega)=\left(\frac{\omega}{c\pi}\right)^2 \mathrm{Re}\left\{ i\,\mathrm{Im}\left(\varepsilon_j\right)\int_0^{\infty} k_{\parallel}dk_{\parallel} \times\int_{t-\Delta z_j/2}^{t+\Delta z_j/2}\left[F(\omega,k_{\parallel},z,z_c^{+})+F(\omega,k_{\parallel},z,z_c^{-})\right]dz\right\} \tag{6.9}$$

where ε_j is the dielectric function of layer j. Δz_j is the thickness of layer j. z_c^{+} and z_c^{-} are the front side and back side location of the cell. The detailed expression of the function F can be found in Ref. [33, 79, 82, 83].

Based on the expression of external radiative recombination provided by Trupke *et al.*, a general expression of the ERRC can be derived by applying Boltzmann approximation on the generalized Planck equation [198]:

$$B_{vrs}=\int_{\omega_g}^{\infty}\frac{\omega^2}{4\pi^2c_0^2n_i^2}\alpha(\omega)\exp\left(-\hbar\omega/k_{\mathrm{B}}T\right)d\omega \tag{6.10}$$

where $\alpha(\omega)$ is the absorptance of the slab, which is derived based on geometric optics neglecting the directional emission of a thin film [198].

6.3 Thin Film Effect on the External Radiative Recombination Coefficient

While the method present above is general, an intrinsic InAs slab is chosen as the example to show the thin film effect on external radiative recombination coefficient. With a direct bandgap of 0.354 eV around room temperature, InAs is a perfect candidate material to transform energy between infrared radiative energy and electrical energy. The dielectric function of InAs is depicted by the summation of absorption due to interband transitions, lattice resonance (optical phonon), and free carrier absorption. Milovich *et al.* developed a comprehensive model to numerically calculate the dielectric function of InAs, which manifests a very good agreement with experimental data at different doping levels and

temperatures [187]. Since the absorption edge of a narrow bandgap semiconductor can be affected under the heavily doped condition, the Moss-Burstein effect is also taken into consideration in this dielectric function model [187, 200, 201]. To be noted, the default temperature of InAs is set at 300 K for the discussion of the ERRCs.

Figure 6.1 exhibits the ERRC of a InAs slab standing in the air (shown in the subplot in Figure 6.1), which is calculated by both FE and Trupke's method using Eq. (6.7) and Eq. (6.10), respectively. The ERRC of the InAs film calculated by FE captures the coherent feature when the film thickness is less than 10 μm; while the result calculated by Trupke's method shows only a monotonical decreasing as the film thickness increases because the geometric optics is used in this method, which neglects the phase information of the propagating electromagnetic waves in the medium [2]. The direction-dependent emission is approximated by normal emission. Clearly, the ERRC calculated by FE can

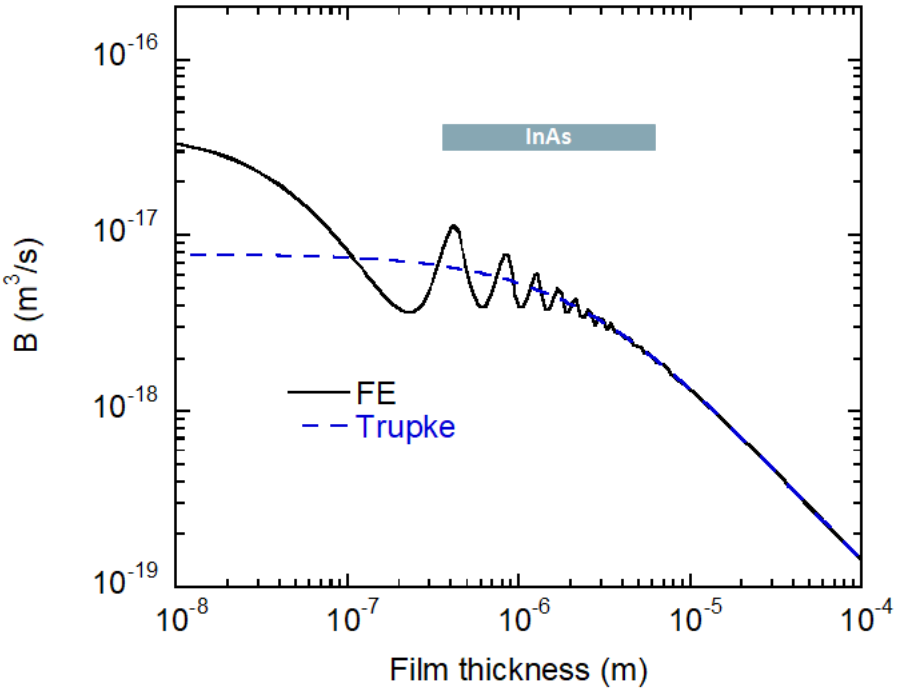

Figure 6.1 The ERRC of a InAs cell as a function of its film thickness.

align quite well with Trupke's method at a thick-film regime (> 10 μm) because the interference effect in the thin-film optics makes no difference for a thick medium and the emission intensity from the surface a thick medium is direction-independent. Therefore, Trupke's model works perfectly for conventional PV cells and LEDs but not for thin-film optoelectronic devices. Moreover, the near-field effect is completely neglected in Trupke's method. Nevertheless, the near-field effect is taken into account by FE, which should be used to model the external luminescence more accurately when the gap thicknesses of near-field radiative energy converters are reduced to the submicron scale.

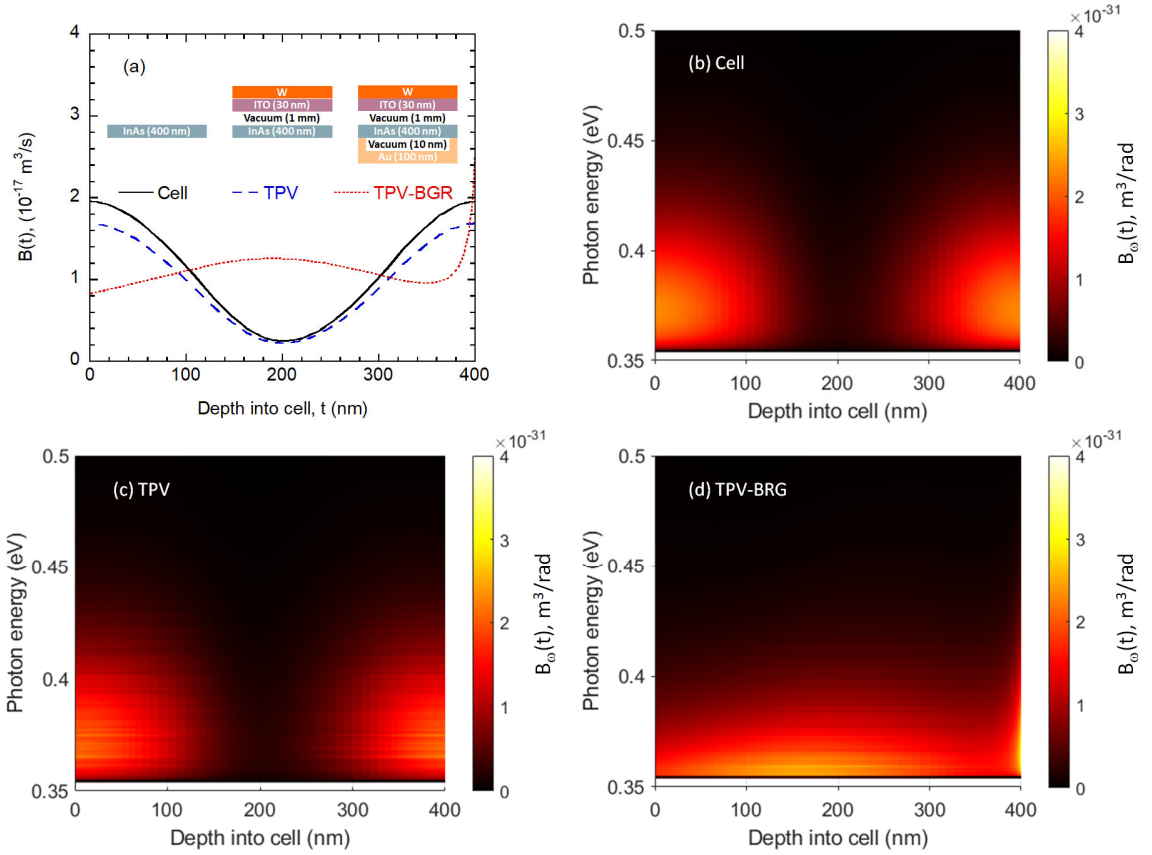

Figure 6.2 (a) Spatial profile of the local ERRC of a cell in three different configurations at far-field regime. Spectral local ERRC of the InAs cell in (b) a cell configuration, (b) a far-field TPV configuration, and (c) a far-field TPV with a BGR configuration.

6.4 Spatial Effect on the Local External Radiative Recombination Coefficient

In the far-field regime, the net radiative heat flux from an object is the difference between the radiosity and irradiation. This irradiation is closely related with the surrounding configurations. Therefore, the net radiative heat flux of an object would be affected by its surroundings. Same conclusion can be applied to the external luminescence. Marti *et al.* have investigated the effect of different backside structures on the dark current of a solar cell, which is essentially the external radiative recombination if the charge transport loss and nonradiative processes are neglected [185]. Similar studies are also performed on the external luminescence and dark current of a near-field TPV cell in different configurations [79, 81, 111]. However, the spatial effect on the local ERRC has barely been investigated for thin-film radiative energy converters. In Figure 6.2(a), the spatial profile of the ERRC of a 400 nm intrinsic InAs cell is calculated for three different configurations, which are shown in the subplots. Compared to the cell configuration, the far-field TPV configuration has an optimized plasmonic emitter made of 30 nm indium tin oxide (ITO) and a bulk tungsten [8], which is separated from the InAs cell with a 1 mm vacuum gap. In Figure 6.2(a), the spatial profile of the local ERRC shows a symmetric valley-shape for both cell and TPV configuration, which indicates there is potentially higher emission possibility of recombined photons at two ends of the cell rather than the middle of the cell. The spectral local ERRC of these two configurations are plotted in Figure 6.2(b) and 2c. Most electron and hole pairs recombine and generate photons with energies from 0.354 eV to 0.45 eV due to the dominant contribution from interband transition in the dielectric functions. Owing to multiple reflections by the front and back interface in the cell configuration, these propagating photons formed a spatial coherent

pattern of emission possibility from the cell. When the film thickness is at micro- or nanoscale, this spatial coherent pattern exists for not only local absorption but also local external radiative recombination, which can be explained by applying the local Kirchhoff's law to coherent absorption of a thin film [199, 202]. Compared to the cell configuration, the generated propagating photons in the TPV configuration are more likely recycled by the cell due to the additional multiple reflection by the plasmonic emitter. Therefore, the two red spots in Figure 6.2(c) are lower than those in Figure 6.2(b). In other words, the spatial profile of the local ERRC of the TPV configuration is reduced when compared to the cell configuration. Moreover, a TPV cell with a back gapped reflector (BGR) is also studied as an example because of its potentially better performance compared to the conventional TPV configurations in both far-and near-field regime [111, 192, 193]. This BGR structure is made of a 100 nm gold and a 10 nm vacuum gap between the gold film and the cell. To be noted, the dielectric functions of tungsten, ITO and gold can be found in Ref. [8] and [83]. By adding a BGR structure on the far-field TPV configuration, the spatial profile of the local ERRC is changed as shown in Figure 6.2(a). Figure 6.2(d) illustrates the dominant spectrum of generated photons is still close to the bandgap of InAs. The emission possibility at the middle is higher than that at the front side of the cell in this TPV-BGR configuration. The rise of the spatial profile of the ERRC at the back of the cell is due to the photon tunneling effect between the gold film and the cell, which will be discussed in the next paragraph.

Strong near-field effect can affect the spatial profile of the ERRC of the TPV-BGR configuration. As shown in Figure 6.3, the ERRC increases as the separation distance between the plasmonic emitter and the cell (d) is reduced from 1 mm to 10 nm. At

nanoscale separation distance (d < 100 nm), both the frustrated modes in the InAs cell and the surface plasmon polaritons (SPPs) close to the surface of ITO are excited [176], which results the rise of the local ERRC at the front side of the InAs cell. At large separation distance (d > 100 nm), the frustrated modes in the InAs film dominate the external luminescence, which results a shift-up from the black solid curve (d = 1 mm) to dashed blue curve (d = 100 nm). The SPPs excited on the surface of the gold lead to the rise of the local external radiative recombination coefficient at the back of the cell. Figure 6.4(a) shows the enhancement effect of the BGR structure on the spatial profile of the local ERRC for a near-field TPV cell. Compared to the TPV configuration, adding a BGR with a 10 nm vacuum gap can enhance photon tunneling effect due to the coupling of the SPPs on the

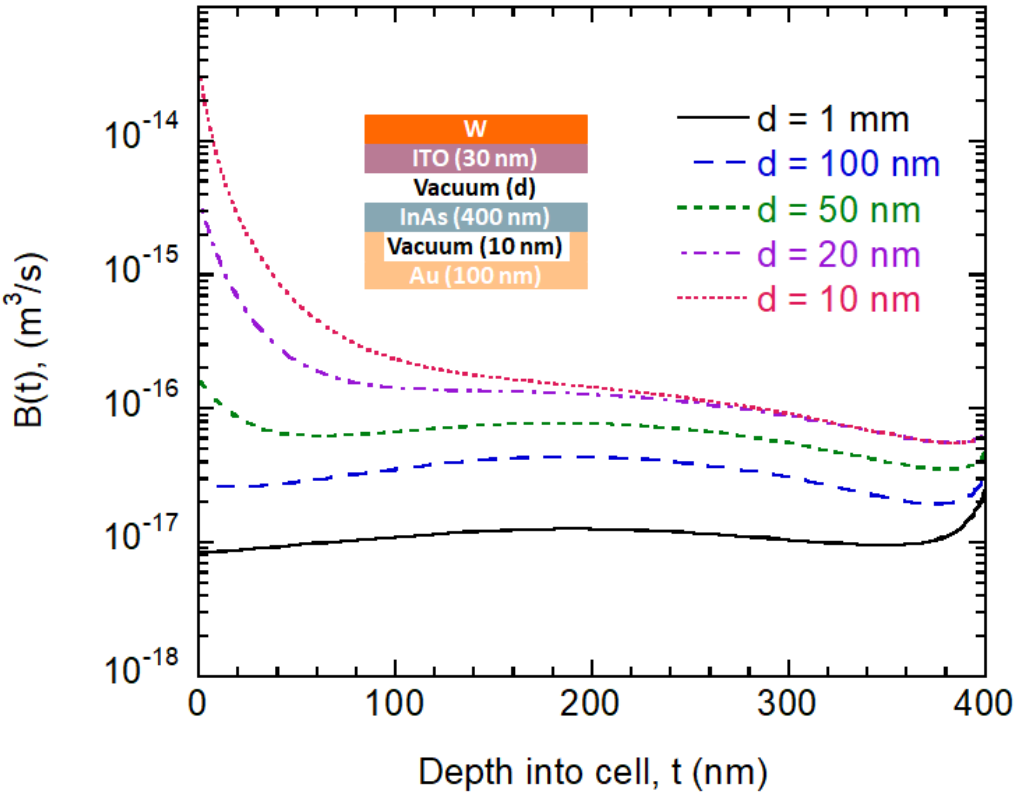

Figure 6.3 Spatial profile of the ERRC as a function of the vacuum gap distance of a near-field TPV cell with a BGR structure.

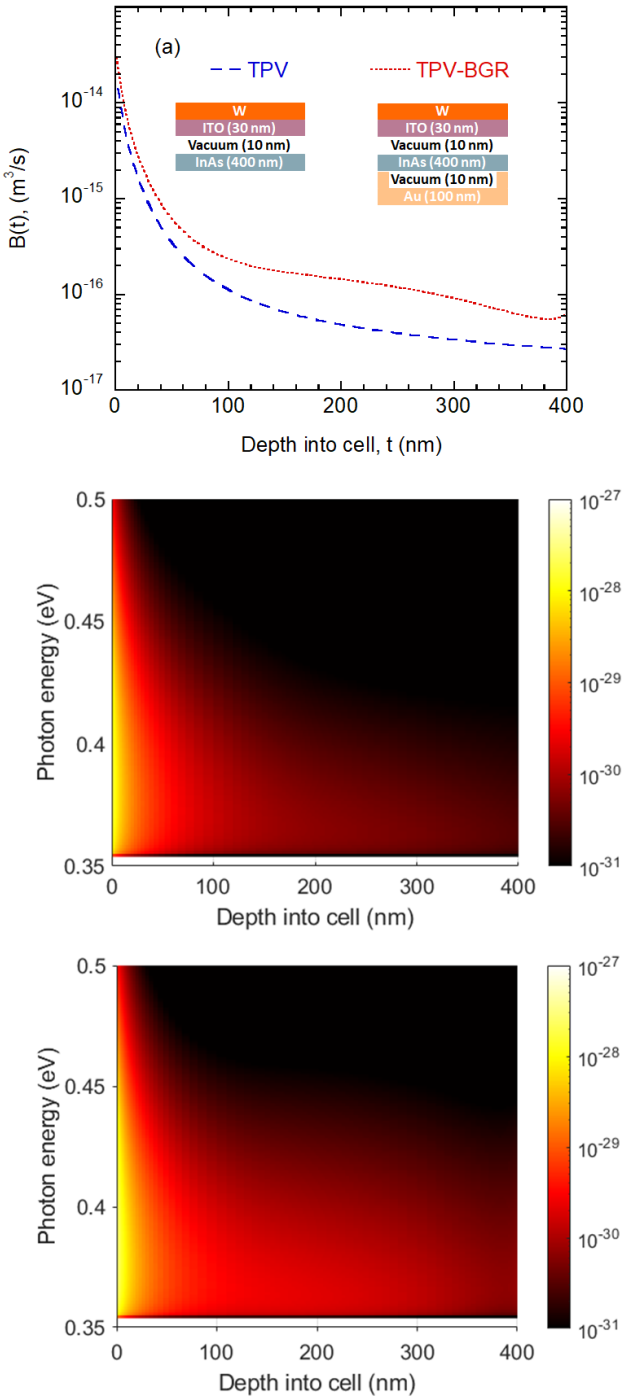

Figure 6.4 (a) Spatial profile of the local ERRC of the cell in a TPV and a TPV with a BGR structure. Spectral local external radiative recombination coefficient of the cell in (b) a cell configuration, (b) a far-field TPV configuration, and (c) a far-field TPV with a BGR configuration.

surface of ITO and frustrated modes in the InAs film. The Fabry-Perot effect brought by the emitter and the BGR modify the spatial coherent pattern of the ERRC and result in an emission boost at the middle part of the InAs cell (t = 150-350 nm). The enhancement of the local ERRC brought by the SPPs of the backside gold film is much smaller than that brought by the SPPs of ITO, since the plasma frequency of ITO is intentionally designed to match with the bandgap of InAs. Also, the skin depth of the coupled SPPs and frustrated modes at the front side is larger than that at the back side of the cell. However, the enhancement due to SPPs on the backside is significant at far-field regime for the TPV-BGR structure, which is shown in Figure 6.2(d). Figure 4b and 4c illustrate the spectral local external radiative recombination coefficients of TPV and TPV-BGR configuration. The strong photon tunnelling phenomenon can be seen at the front side of the cell for both configurations. At every wavelength and location, the TPV-BGR configuration possesses a higher spectral local ERRC representing a better luminescence capability than the TPV configuration.

6.5 Doping Effect of Narrow Bandgap Semiconductors

As a narrow bandgap semiconductor material, the energy states at the bottom of the conduction and valence band are easily populated by free carriers. As the electron or hole concentration increases beyond the effective density of states in the conduction or valence band due to heavy doping effect, the InAs become degenerate, where the Moss-Burstein shift should be taken into consideration in the process of interband transitions.[203, 204] When the lower energy states of the conduction band or higher energy states of the valence band are filled, the interband transitions of the electrons at the valence band require photons with energies larger than bandgap. Therefore, the absorption coefficient due to interband

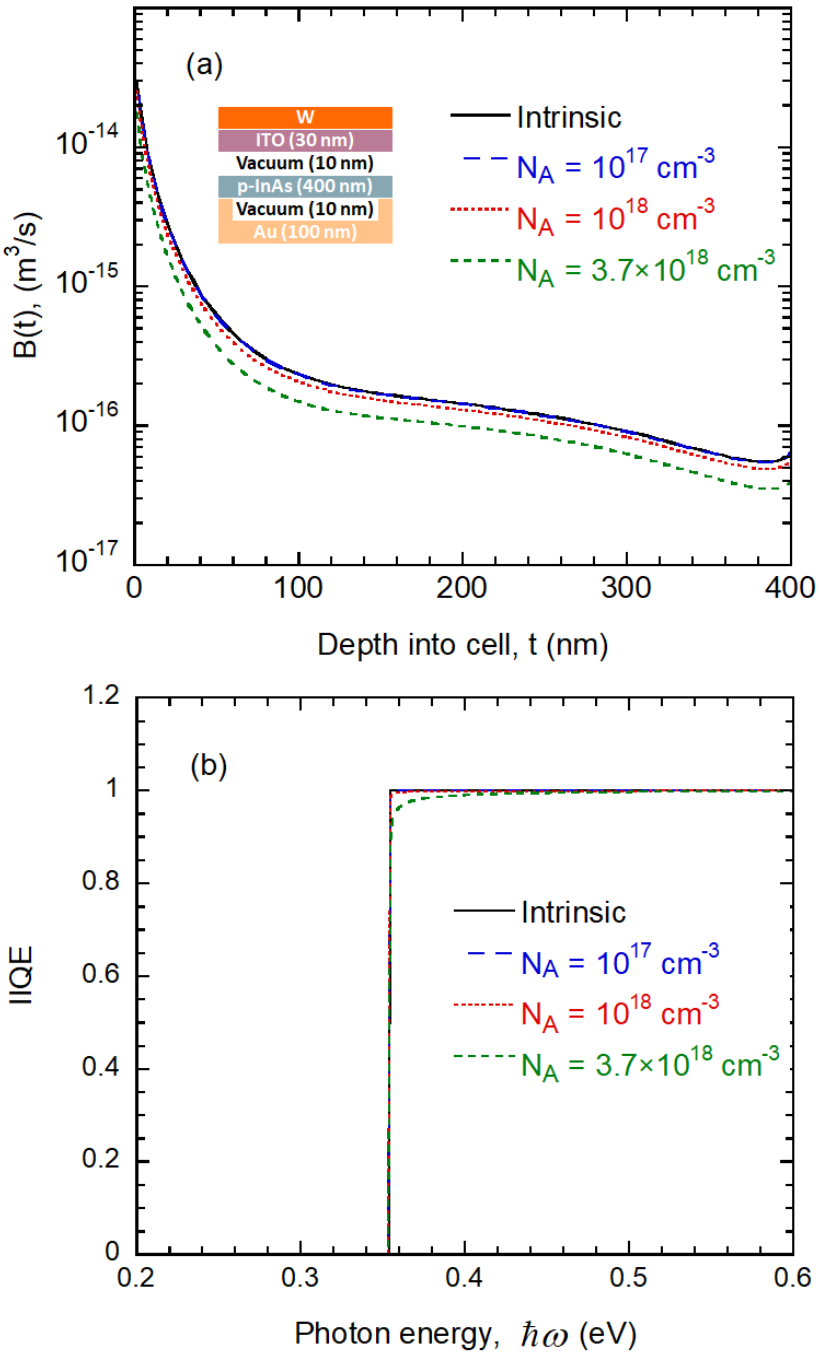

Figure 6.5 (a) Spatial profile of the local ERRC and (b) the IIQE of a near-field TPV cell with a BGR structure at different doping levels. $N_A = 3.7\times10^{18}$ cm^{-3} is the boundary between a nondegenerate semiconductor and degenerate semiconductor for p-doped InAs at 300 K.

transition is reduced when the doping level is increased. As a reverse process of interband absorption, the interband emission (radiative recombination) has the same behavior as the interband absorption coefficient. Shown in Figure 6.5(a), the spatial profile of the ERRC of a *p*-type InAs in the TPV-BGR configuration remains almost unchanged at a lightly doping level ($N_A < 10^{18}$ cm^{-3}). When the doping level increases from $N_A = 10^{18}$ cm^{-3} to $N_A = N_v(300\ K) = 3.7\times10^{18}$ cm^{-3}, which is the effective density of states in the valence band at 300 K, the spatial profile of the local ERRC decreases relatively significant and the ERRC of the cell decreases from 6.9×10^{-16} m^3/s to 4.1×10^{-16} m^3/s. To be noted, the local ERRC is also related with the IIQE based on Eq. (6.8). When the doping level increases, the numerator of the IIQE is reduced due to the Moss-Burstein shift. Based on the sum rule of dielectric function, the nonradiative contribution (mainly the contribution from free carrier at the wavelength above the bandgap) to the dielectric function of InAs further reduce the IIQE. Theoretically speaking, the reduction of the local ERRC is on account of combination effect of the Moss-Burstein shift and free carriers vibration. Nevertheless, as shown in Figure 6.5(b), the IIQE doesn't change significantly even when the doping level is close to the effective density of states in the conduction band. Therefore, the Moss-Burstein shift is dominant effect on the reduction of local external radiative recombination at a heavily doped InAs cell.

6.6 Thermal Radiation and Luminescence of a Near-Field Thermoradiative Cell

Due to low doping condition and low cell working temperature, the IIQE of a InAs cell can be assumed to be zero at the frequency below the bandgap energy and unity at the frequency above the bandgap energy, respectively, which is also referred as the ideal IIQE assumption. It is a common and reasonable assumption for radiative energy converters

made of the direct bandgap semiconductors with low doping levels. However, this assumption can cause substantial error when one is modeling the radiative energy converters made of heavily doped direct semiconductors even not necessary under degenerate conditions. The temperature effect on the IIQE of the heavily doped InAs is clearly illustrated in Figure 6.6. As temperature increases, the bandgap of InAs is shrunk

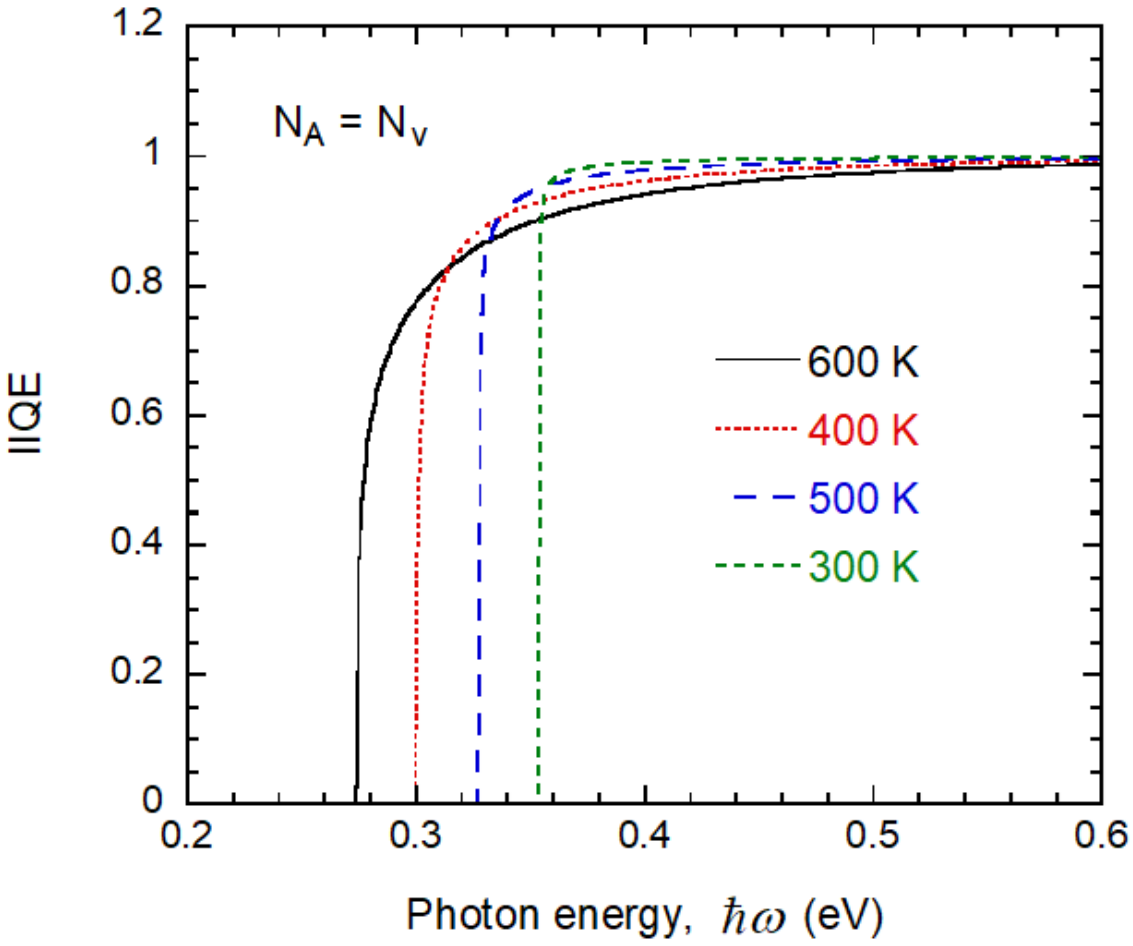

Figure 6.6 Intrinsic internal quantum efficiency of a InAs cell as a function of photon energy at different cell temperatures. The *p*-type InAs is fixed at the same value of effective density of states in the valence band at a given temperature, which is the boundary between a nondegenerate semiconductor and degenerate semiconductor for *p*-type InAs at that temperature.

from 0.354 eV at 300 K to 0.273 eV at 600 K. As the temperature of InAs is increased, the effective density of states in the valence band increases proportional to $T^{3/2}$ [188].

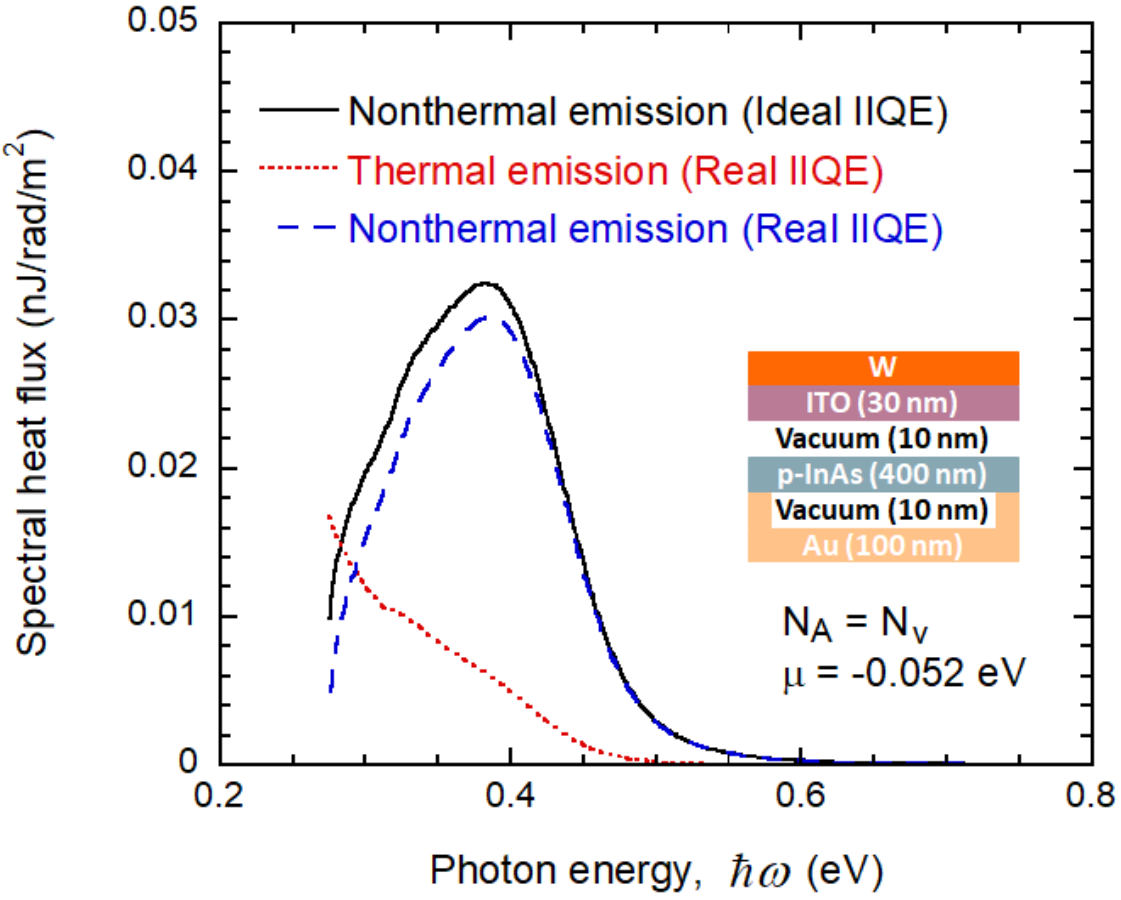

Figure 6.7 Spectral heat flux of the net thermal and nonthermal emission of a p-doped InAs cell in a near-field TR device with a BGR structure. The doping level is intentionally chosen at $N_A = N_V(600\ K)$ to clearly show the contribution of thermal radiation and nonthermal radiation. The InAs cell with the gold BGR is set at 600 K and the cold side is made of a bulk tungsten and ITO film, which are set at 300 K. This near-field TR device is operating at the maximum efficiency with a given photon chemical potential (μ = -0.052 eV). For the ideal IIQE assumption, no thermal radiation is emitted above the bandgap energy.

Therefore, the doping level is also increasing as the temperature increases and the IIQE curves of higher temperatures approximate to 1 slower than that of lower temperatures as the photon frequency increases. For 300 K, the ideal IIQE assumption is rather reasonable. However, potential errors become inevitable if the ideal IIQE assumption is applied to a InAs cell in a near-field TR-BGR configuration, which is shown in the subplot in Figure 6.7. Normally, for a TPV-BGR configuration, the hot emitter made of tungsten and ITO is contacting with hot source with higher temperatures and the cell is supposed to contact with a heat sink to maintain at a lower temperature. By switching the hot side with the cold side, the TPV-BGR configuration is turned into a TR-BGR configuration. The side of *p*-type InAs with a BGR structure is fixed at 600 K, and the side of tungsten and ITO is fixed at 300K as shown in the subplot in Figure 6.7. The photon chemical potential is fixed at -0.052 eV, which is corresponding to the maximum power condition of this TR cell. The ideal IIQE and real IIQE are used in the calculation to indicate that the ideal IIQE assumption can cause the substantial error of the net thermal and nonthermal emission. For a real IIQE, there should be two components of external emission: thermal emission and nonthermal emission. As the photon frequency increases, the IIQE approximates to unity indicating the interband transitions become dominant than the free carriers vibration. Therefore, the net thermal emission is decreasing as the photon frequency increases. When applying the ideal IIQE assumption, no thermal emission or absorption is existing above the bandgap energy of a InAs cell. The thermal contribution to the external emission is mistakenly turned into external luminescence. Hence, the total net nonthermal emission calculated by the ideal IIQE assumption is 7.4 kW/m^2, which is overestimated by 11% compared to that calculated by real IIQE. This overestimation result in a critical difference

when predicting the performance of the TR cell in this near-field TR-BGR configuration. As shown in Figure 6.8, the maximum power predicted by ideal IIQE assumption is 1.04 kW/m^2, while the real maximum power is only 0.923 kW/m^2. Same observation can be made for the maximum efficiency. Note, the efficiency of the above TR-BGR configuration is not practical because this configuration and selected materials are optimized for a near-field TPV, but not for a near-field TR. However, the observations provide evidence to support our conclusion that capturing the spatial effect and

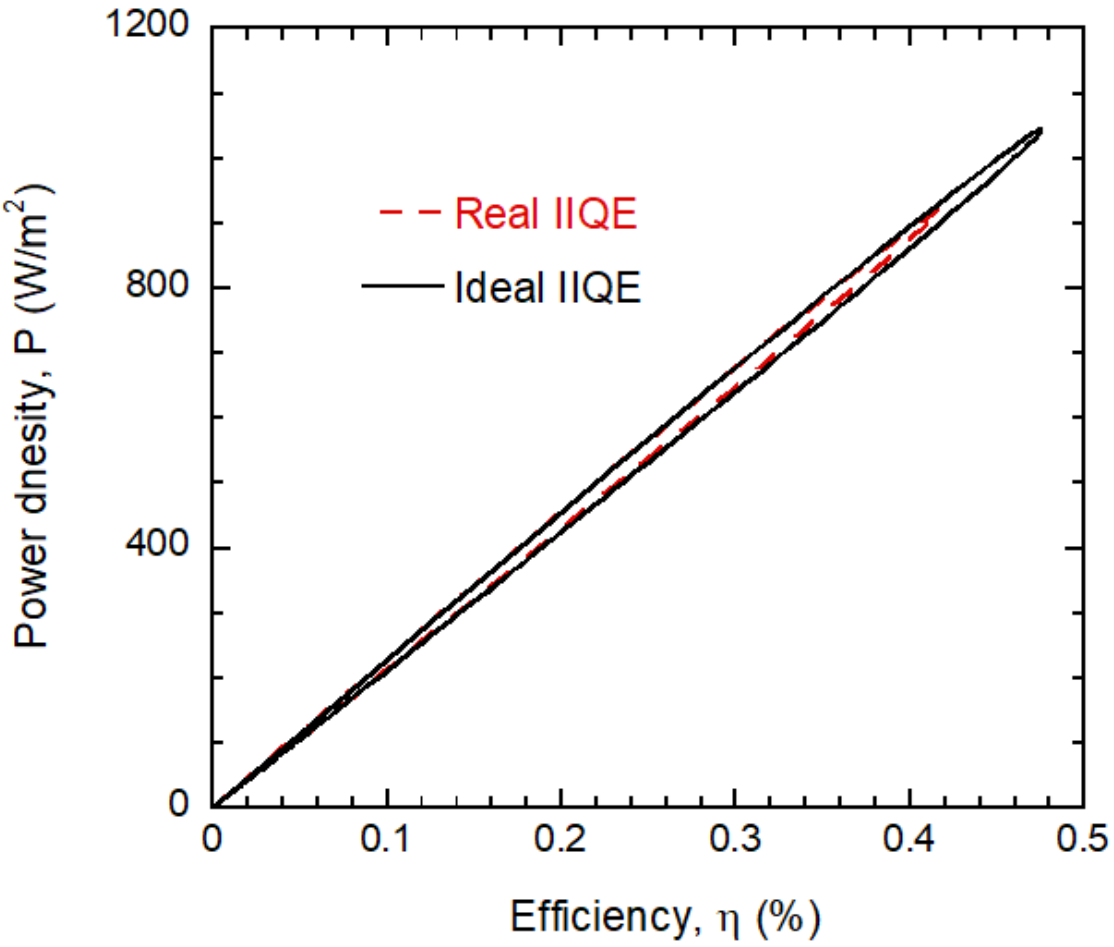

Figure 6.8 The power-efficiency curve of a near-field TR device with a BGR structure. The device parameters are the same as Fig. 7. To be noted, nonradiative generation processes (Auger and SRH) are neglected here.

using the accurate value of IIQE are important parameters to accurately predict the performance of a thin-film near-field energy converter.

Instead of using the generalized van Roosbroeck-Shockley model, this work demonstrates that fluctuational electrodynamics should be applied to fully capture various local effects on the external radiative recombination of thin-film radiative energy converters. Spatial effect due to multiple reflections and near-field radiation can significantly modify the local ERRC and increase the ERRC by several orders of magnitudes. One should consider the doping effect on the external radiative recombination only for a radiative energy converter consisting of heavily doped semiconductor, where the Moss-Burstein shift should also be considered. The thermal and nonthermal contributions to emission and absorption in a thin-film radiative energy converter are quantitively distinguished. By comparing the predicted performance of a near-field TR-BGR configuration using a real IIQE and an ideal IIQE, we concluded that the IIQE is an important parameter to model a thin-film radiative energy converter.

CHAPTER 7. NEAR-FIELD RADIATIVE ENERGY CONVERTERS USING 2D METAMATERIALS

This Chapter introduces a contactless two-terminal structure made of hexagonal boron nitride (hBN) and indium antimonide (InSb) films. A near-field photonic thermal diode is proposed by coupling (or decoupling) the temperature-dependent internband absorption of InSb with the hyperbolic phonon polaritons (HPhP) in hBN. By employing the strong above-bandgap photon flux and the suppressed sub-bandgap heat flux, a near-field thermoradiative device is theoretical demonstrated with a record high performance.

7.1 A Near-Field Photonic Thermal Diode

Analogous to its electronic counterpart, a thermal diode is a two-terminal device with an asymmetric thermal transfer function that depends on the direction of temperature gradient.[18] Photonic thermal diodes based on radiative heat transfer between the two terminals at different temperatures separated by a vacuum gap are enabled by the temperature-dependent dielectric functions (or emissivities in the far field) of the materials used [205-209]. Photonic thermal diodes have advantages over phononic thermal diodes in terms of operating in a noncontact mode and over a relatively large temperature range. The rectification ratio is often used to quantify the performance of a thermal diode, and it is defined as $\mathrm{R} = q_{\mathrm{f}} / q_{\mathrm{r}} - 1$, where q_{f} and q_{r} represent the magnitude of the forward and reverse heat fluxes, respectively. Researchers are seeking thermal diode designs with high rectification ratios for possible applications in energy conversion, electronic thermal management, building thermal regulation, and human thermal comfort. [18, 210]

Radiative heat transfer can be greatly enhanced in the near field (when the separation distance between the two objects is smaller than the thermal radiation wavelengths), especially with micro/nanostructures or metamaterials, and has been extensively investigated in recent years both theoretically and experimentally [2, 51, 72, 162, 211]. Near-field thermal modulation and rectification have also been demonstrated experimentally by several groups [212-215]. Otey *et al*. proposed the first photonic thermal rectification scheme based on the temperature dependence of electromagnetic resonances in different SiC polytypes and predicted a rectification ratio of 0.41 at a 100 nm vacuum gap with a temperature difference of 200 K.[2] Wang and Zhang theoretically investigated thermal rectification between dissimilar materials and predicted R = 9.9 with a 5 nm vacuum gap between Si and SiO_2 at temperatures of 1000 and 300 K, respectively [206]. Thermochromic materials and metal-to-insulator phase change materials (PCMs) such as VO_2 have been extensively studied for use in photonic thermal diodes in both the near field [216, 217] and the far field [218-221]. Graphene-coated structures have also been considered to build photonic thermal diodes [222, 223]. The best estimated rectification ratios with planar or multilayer films are around 10 as summarized by Wen *et al.* [224] Furthermore, asymmetrically patterned photonic nanostructures have been considered to achieve higher rectification ratios (R > 10) [225]. By coupling a PCM (VO_2) with gratings and multilayered nanostructures, Chen *et al.* numerically demonstrated R ≈ 24 at a 50 nm vacuum gap with a temperature difference of 10 K above and below the VO_2 transition temperature of 341 K [226]. High rectification ratios may also be achieved with superconductors but the operating temperatures are limited to below 20 K [227, 228].

In this work, a near-field photonic thermal diode is proposed with a semiconductor InSb film and a hexagonal boron nitride (hBN) sheet. The underlying mechanism is to

couple/decouple the interband absorption of InSb with the hyperbolic phonon polariton (HPhP) of hBN in the mid-infrared region. InSb is a narrowband semiconductor material with a bandgap energy $E_g \approx 0.175$ eV (corresponding to a wavelength of 7.1 μm) and has been considered for near-field thermophotovoltaic applications [88, 121]. The bandgap energy increases as the temperature is lowered, resulting in a shift of the interband absorption edge toward short wavelengths [229, 230]. In recent years, hyperbolic metamaterials have been extensively studied for subwavelength imaging and near-field radiative transfer [2, 51, 162, 231, 232]. Some naturally occurring 2D materials with layered structures (such as hBN) exhibit hyperbolic bands and support HPhPs [233]. Near-field radiative heat transfer can greatly exceed the blackbody limit at nanoscale separation distances when HPhPs are excited in the hBN sheets [234, 235]. The strong temperature dependence of the absorption edge allows the absorption of InSb to couple (or decouple) with the hyperbolic band of hBN, when the temperature of InSb is higher (or lower) than that of hBN. The scheme proposed here may enable a higher rectification ratio without using gratings or nanoparticles.

As shown in Figure 7.1(a), the photonic thermal diode consists of an InSb film, whose thickness is h_1 at temperature T_1 and a hBN sheet whose thickness is h_2 at temperature T_2, separated by a vacuum gap of distance d. The medium behind InSb (or hBN) is assumed to be vacuum that extends to infinity and is at a thermal equilibrium with the adjacent solid. The net heat flux from medium 1 to medium 2 is represented by q_{12}. Each medium includes the infinitely extended vacuum behind the film. FE and a transfer matrix method are used to calculate the near-field radiative heat transfer between two thin films. The net heat flux from 1 to 2 is given by simplifying Eq. (2.21)

$$q_{12} = \frac{1}{4\pi^2}\int_0^\infty \left[\Theta(\omega, T_1) - \Theta(\omega, T_2)\right] d\omega \times \int_0^\infty \sum_{j=s,p} \xi_j\left(\omega, k_{\|}\right) k_{\|} dk_{\|} \tag{7.1}$$

where $\Theta(\omega, T)$ is the mean energy of the Planck oscillator as defined in Chapter 3. $k_{\|} = \sqrt{k_x^2 + k_y^2}$ is the magnitude of the wavevector in the *x*-*y* plane with k_x and k_y being the *x* and *y* components of the wavevector, and $\xi_j\left(\omega, k_{\|}\right)$ is the energy transmission coefficient for either transverse electric (TE) waves (*s*-polarization) or transverse magnetic (TM) waves (*p*-polarization). The energy transmission coefficient is calculated from Eq. (2.21)

$$\xi_j\left(\omega, k_{\|}\right) = \begin{cases} \dfrac{\left(1 - r_{1j} r_{1j}^*\right)\left(1 - r_{2j} r_{2j}^*\right)}{\left|1 - r_{1j} r_{2j} e^{2ik_{z0}d}\right|^2}, & k_{\|} < k_0 \\ \dfrac{4\,\mathrm{Im}\left(r_{1j}\right)\mathrm{Im}\left(r_{2j}\right) e^{-2|k_{z0}|d}}{\left|1 - r_{1j} r_{2j} e^{2ik_{z0}d}\right|^2}, & k_{\|} > k_0 \end{cases} \tag{7.2}$$

where $k_0 = \omega / c$ is the wavevector with c being the speed of light in vacuum, $k_{z0} = \left(k_0^2 - k_{\|}^2\right)^{1/2}$ is the *z*-component wavevector in vacuum, and r_{1j} or r_{2j} is the reflection coefficient of the semi-infinite media including InSb or hBN, respectively. The reflection coefficients are calculated by treating hBN as a uniaxial thin film and InSb as an isotropic medium [2, 162]. The dielectric functions of hBN and InSb are needed for computing the radiative heat flux.

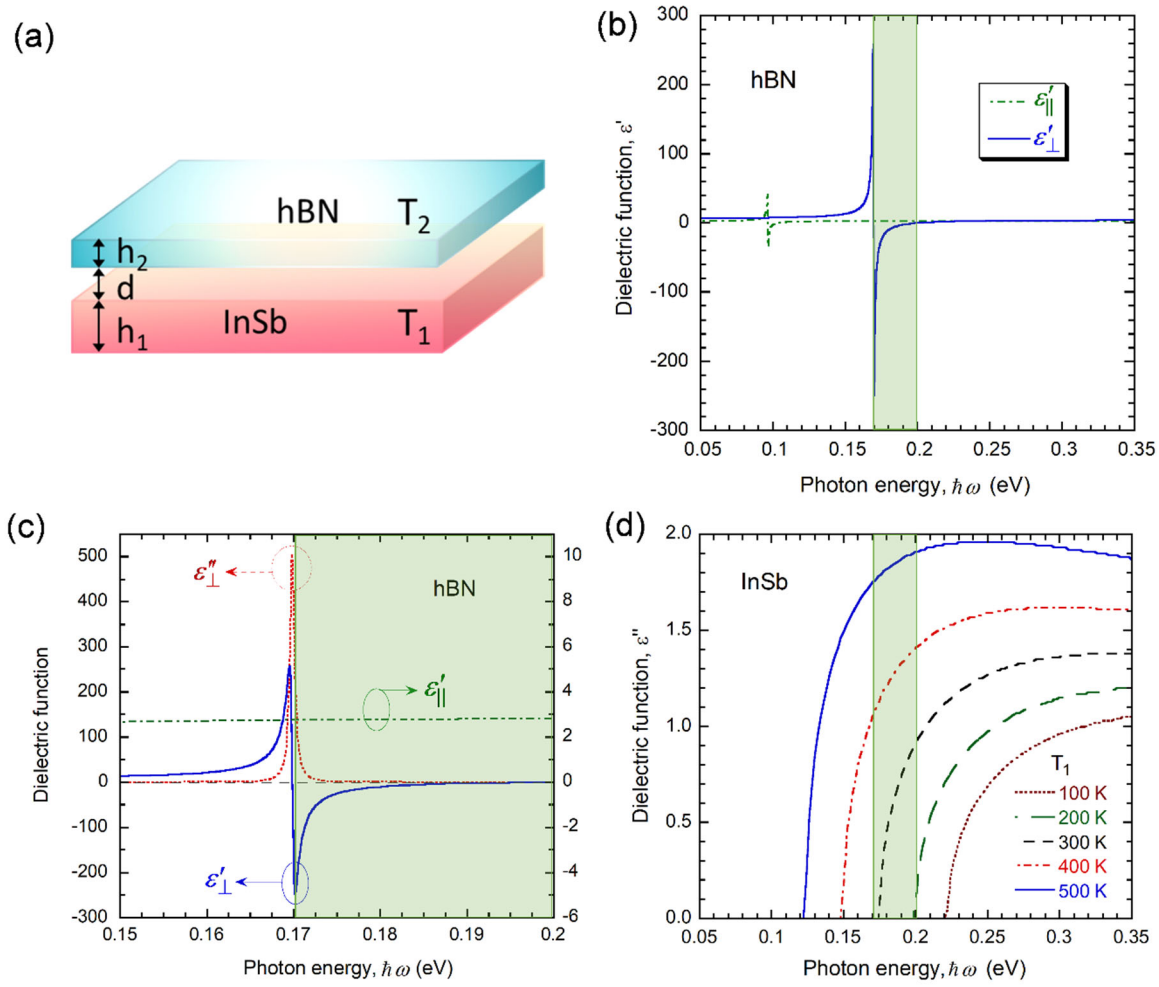

Figure 7.1 (a) Schematic of the near-field radiative thermal diode with an InSb film (thickness h_1) and hBN sheet (thickness h_2) at temperatures of T_1 and T_2, respectively, separated by a vacuum gap of distance d. (b) Ordinary and extraordinary dielectric functions (real part only) of hBN, showing the two hyperbolic bands. (c) Dielectric functions of hBN near type II hyperbolic band, noting that the imaginary part of the extraordinary component is negligibly small in this region. (d) The imaginary part of the dielectric function of InSb at different temperatures.

The hBN sheet is a uniaxial medium due to its layered structures. In the present study, the optical axis of hBN is parallel to the *z*-direction so that its dielectric tensor may be expressed as $\bar{\bar{\varepsilon}}_2 = \mathrm{diag}(\varepsilon_\perp, \varepsilon_\perp, \varepsilon_{||})$, where $\varepsilon_\perp$ is the ordinary dielectric function (when the electric field is in the *x*-*y* plane) and $\varepsilon_{||}$ is the extraordinary dielectric function (when the electric field is parallel to the optical axis or *z*-axis). Lattice vibrations in either the in-plane or out-of-plane direction result in a mid-infrared Reststrahlen band in the ordinary or extraordinary dielectric function, respectively. Therefore, the dielectric functions of hBN can be modeled as [233, 234]

$$\varepsilon_m(\omega) = \varepsilon_{\infty,m}\left(1 + \frac{\omega_{\mathrm{LO},m}^2 - \omega_{\mathrm{TO},m}^2}{\omega_{\mathrm{TO},m}^2 - i\gamma_m\omega - \omega^2}\right) \tag{7.3}$$

where ω is the angular frequency, $m = \perp$ or $||$, ε_∞ is a high-frequency constant, TO and LO represent transverse optical phonon and longitudinal optical phonon modes, respectively, and γ is the damping coefficient. These parameters are taken from Kumar *et al.* [233] and assumed to be independent of temperature. The real parts of dielectric functions of hBN are shown in Figure 7.1(b). There are two hyperbolic bands in which $\varepsilon'_\perp \varepsilon'_{||} < 0$. Type II hyperbolic band with $\varepsilon'_\perp < 0$ in the region $0.17\ \mathrm{eV} < \hbar\omega < 0.20\ \mathrm{eV}$ is shaded, because it plays a key role in the proposed thermal diode. As shown in Figure 7.1(c), a large spike occurs in the imaginary part of the ordinary dielectric function ($\varepsilon''_\perp$) near 0.17 eV, and $\varepsilon''_\perp$ decays quickly toward higher and lower photon energies; this suggests a strong resonance at $\omega = \omega_{\mathrm{TO},\perp}$. The real part of the extraordinary dielectric function ($\varepsilon'_{||}$) is nearly a constant (≈ 2.8), while the imaginary part ($\varepsilon''_{||}$) is negiligibly small for $\hbar\omega > 0.15\ \mathrm{eV}$ and thus not plotted.

As a widely used narrow bandgap semiconductor, the interband absorption coefficient of InSb is strongly temperature dependent [229, 230]. The dielectric function of intrinsic (undoped) InSb can be approximately modeled as [88]

$$\varepsilon_1(\omega,T)=\left[n_1+\mathrm{i}\frac{\alpha(\omega,T)}{2k_0}\right]^2 \tag{7.4}$$

Here, n_1 is the refractive index, and α is the absorption coefficient due to interband absorption given by

$$\alpha\left(\omega,T\right)=\begin{cases}0, & \omega<\omega_{\mathrm{g}}(T)\\ \alpha_0\left[\dfrac{\omega-\omega_{\mathrm{g}}(T)}{\omega_{\mathrm{g}}(T)}\right]^{1/2}, & \omega>\omega_{\mathrm{g}}\left(T\right)\end{cases} \tag{7.5}$$

where $\omega_{\mathrm{g}}\left(T\right)=E_{\mathrm{g}}\left(T\right)/\hbar$ is the angular frequency corresponding to the bandgap energy E_{g} with $\hbar$ being the reduced Planck constant. It is reasonable to use the fitting value of $\alpha_0\approx 7000\ \mathrm{cm}^{-1}$ for all temperatures [88, 232]. It should be noted that Eq. (5) did not consider the effects of lattice vibration, free-carrier absorption, and the Ürbach tail [236]. These effects will be discussed later. The temperature-dependent bandgap energy of InSb was fitted to the Varshni relation as follows: $E_{\mathrm{g}}\left(T\right)=0.235-2.7\times10^{-4}T^2/(T+106)$, where T is in (K) and E_{g} is in (eV) [230]. This relation has been experimentally validated from about 10 to 600 K [230, 237]. As shown in Figure 7.1(d), the bandgap energy (the rising point of the curve) shifts to smaller values as the temperature increases. For InSb, the imaginary part of the dielectric function is proportional to the absorption coefficient if the refractive index is taken as a constant ($n_1=3.96$) [238]. As the temperature increases, the interband absorption spectrum of InSb approaches and then overlaps with the

hyperbolic band of hBN, i.e., shaded region in Figure 7.1(d). Coupled with the HPhPs of hBN, photon tunneling can occur through the nanoscale vacuum gap in a narrow band when the InSb film is at a relatively higher temperature.

Consider h_1 = 100 μm (InSb), h_2 = 5 nm (hBN), and a vacuum gap of d = 10 nm. Though maintaining such a small vacuum gap between two thin films poses practical challenges, the purpose here is to demonstrate the promising performance of the proposed device. The heat flux q_{12} is calculated with an average temperature $T_{\text{avg}} = (T_1 + T_2)/2 = 300$ K and plotted in Figure 7.2 as a function of the temperature difference $\Delta T = T_1 - T_2$ for both the forward and reverse bias cases. For the structure considered here, the forward bias is when $T_1 > T_2$ so that $q_{\text{f}} = q_{12}$. For the reverse bias, $q_{\text{r}} = -q_{12}$ because q_{12} is negative. The nanometer thickness of hBN is chosen to obtain strong resonance with sharp peaks in the heat flux spectrum at nanometer distances [235]. The curve resembles the current-voltage curve of a diode (dark current curve) with an exponential growth of the heat flux in the forward direction and a much smaller magnitude in the reverse direction. In contrast, for thermal diode made of VO_2, the heat flux changes linearly with temperature difference (though the slope is different between the forward and reverse biases) [226]. In the reverse direction, the heat flux does not change significantly with the proposed design. Therefore, increasing the temperature difference results in an increase in the rectification ratio. The rectification ratio is also shown in Figure 7.2 as a function of $|\Delta T|$ using the double y-axis plot. When $|\Delta T| = 200$ K, R = 17.1, which surpasses previously reported figures in the similar temperature range for planar or multilayered structures at $d \geq 10$ nm. The heat flux with $T_1 = 400$ K and $T_2 = 200$ K is

about 9.7 times that between two blackbodies at these temperatures. The near-field heat flux enhancement between InSb and hBN is not as strong as that between two hBN sheets [234, 235]. When the heat flow direction is reversed (i.e., $T_1 = 200$ K, $T_2 = 400$ K), the heat flux is about 53% that between two blackbodies. The reduction is presumably due to multiple reflections with the InSb and hBN layers. Even with a smaller $|\Delta T|$, relatively

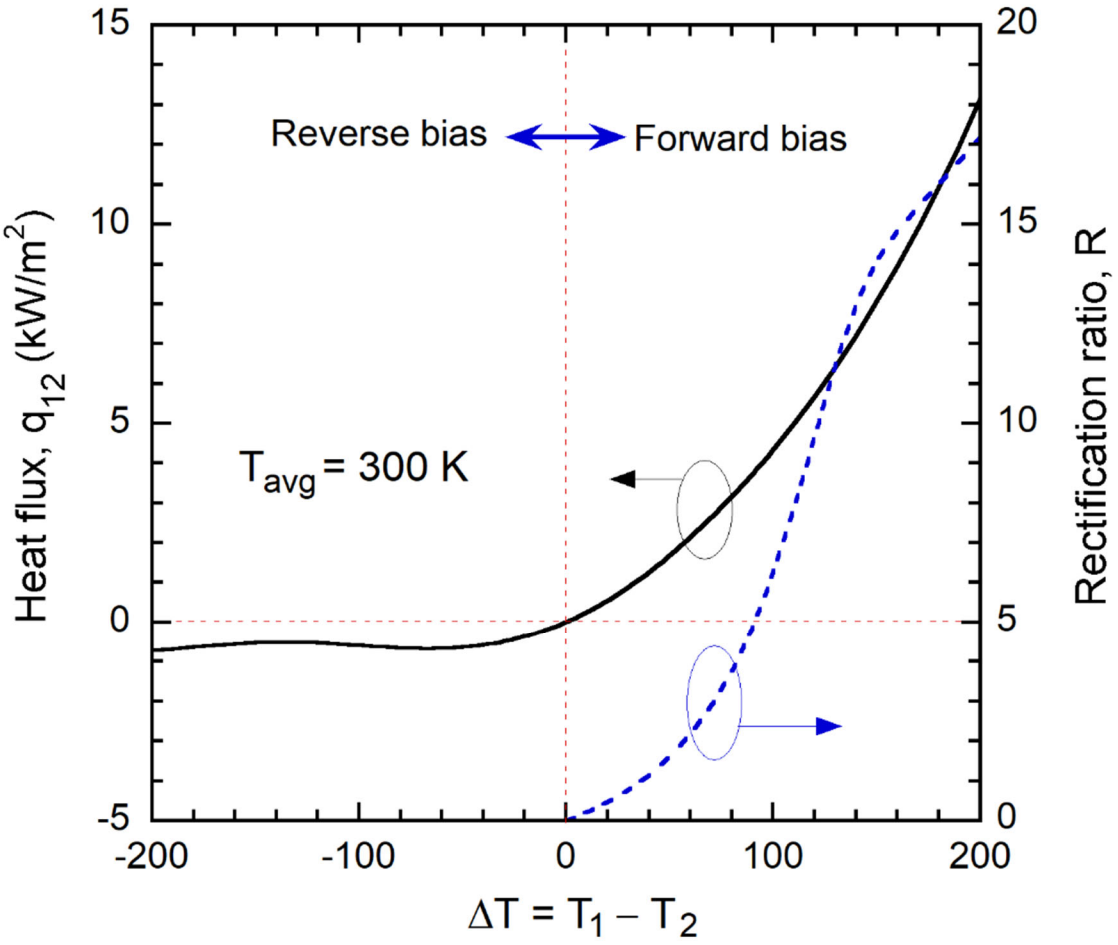

Figure 7.2 The net heat flux and rectification ratio vs the temperature difference for the proposed near-field photonic thermal diode calculated at an average temperature of 300 K for $h_1 = 100$ μm, $h_2 = 5$ nm, and $d = 10$ nm.

large R values can still be achieved: for example, R = 2.17, 5.13 and 9.67, when $|\Delta T|$ = 60, 92 and 120 K, respectively. Note that another way to characterize the thermal performance is to use a rectification efficiency defined as $\sigma = 1 - q_r / q_f$. A rectification ratio of 9.67 or 17.1 corresponds to σ = 0.906 and 0.945, respectively.

The spectral heat flux $q(\omega)$ for both the forward and reverse scenarios is shown in Figure 7.3(a) when ΔT = 200 K and the other conditions are the same as for Figure 7.2. The spectral heat flux between two blackbodies at 400 K and 200 K is also shown for comparison. The forward $q(\omega)$ is significantly higher than that for the reverse case heat flux near the hyperbolic region. Since $E_g(400\text{ K}) \approx 0.15$ eV, $q(\omega)$ for the forward bias starts to increase at $\hbar\omega > 0.15$ eV due to frustrated modes [213], which increases sharply at 0.17 eV where $\varepsilon_\perp''$ reaches a peak. As $\hbar\omega$ increases beyond 0.17 eV, it falls in the hyperbolic band of hBN where $q(\omega)$ continues to increase and reaches a peak near 0.182 eV and then decreases as $\hbar\omega$ further increases. Interference within the InSb film causes oscillations in the heat flux spectra for $\hbar\omega < E_g$. When $\hbar\omega < 0.15$ eV, the dielectric function of InSb is the same at 200 K and 400 K, and the forward and backward spectra overlap with each other. Because InSb is treated as nonabsorbing in this region, only propagating waves in vacuum can be supported. Furthermore, surface reflection results in a reduction of the heat transfer that is even smaller than that between two blackbodies. The oscillations continue for the reverse bias $E_g(200\text{ K}) \approx$ 0.2 eV. A small peak occurs at 0.17 eV in the reverse scenario due to the spike in $\varepsilon_\perp''$. For the reverse bias, there is a quick rise in $q(\omega)$ near 0.2 eV; however, the magnitude is relatively small since it is beyond the hBN hyperbolic band and only propagating waves in vacuum can be supported. For $\hbar\omega > 0.23$ eV, the difference between the forward and reverse scenarios is

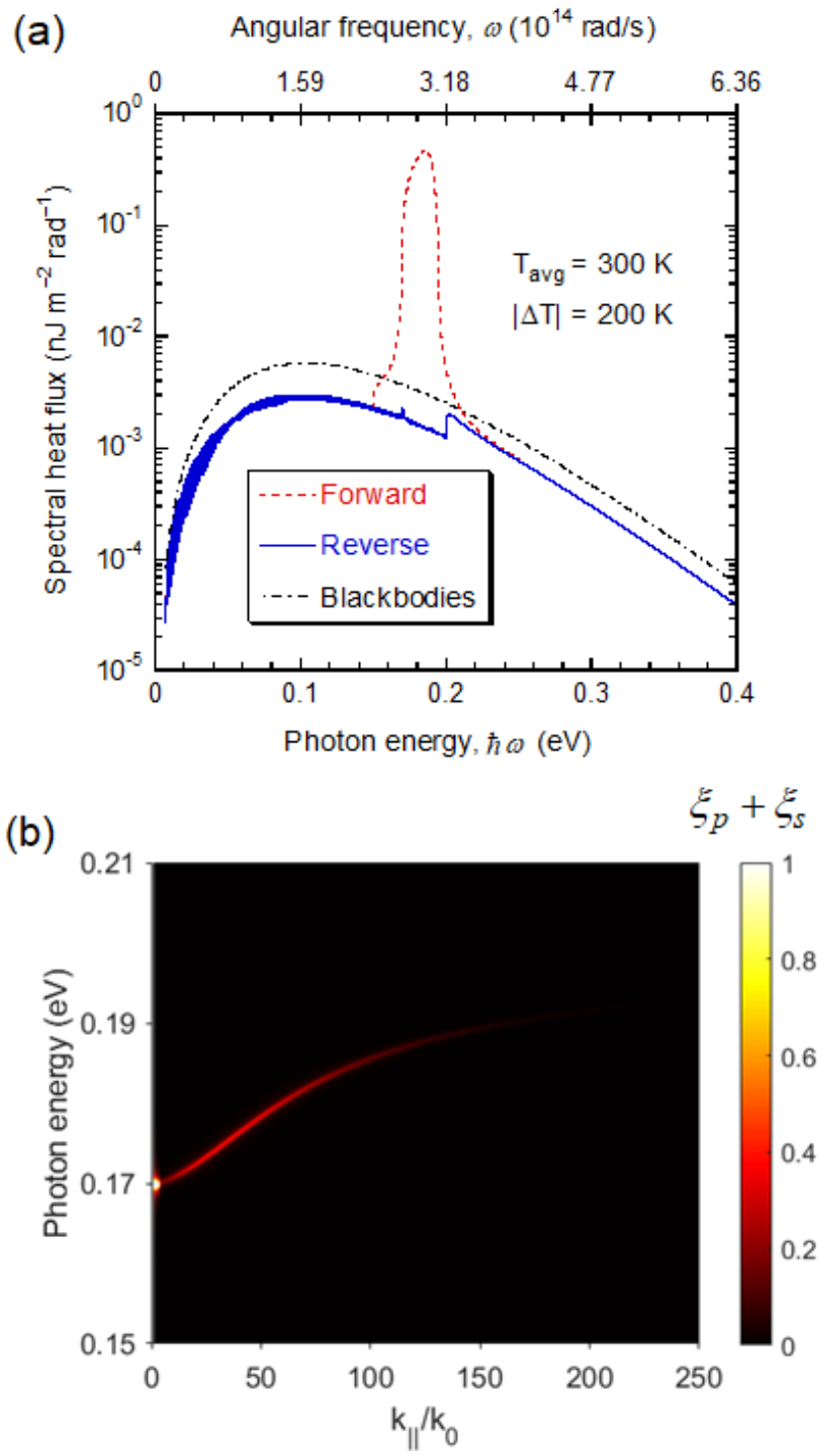

Figure 7.3 (a) Spectral heat flux for both the forward and reverse scenarios and between two blackbodies for $\Delta T = 200$ K and $T_{avg} = 300$ K, and the other conditions are the same as for Figure 7.2(b) Contour plot of the transmission coefficient under the forward bias.

negligibly small. In this region, the absorption by the thin hBN sheet is negligible so that only propagating waves in vacuum are supported. No interference effects are expected at $\hbar\omega > 0.20$ eV, since the InSb film is essentially opaque in this region. In this case, the surface reflection between vacuum and InSb is dominated by the refractive index rather than the absorption coefficient. Hence, the forward and backward $q(\omega)$ almost overlap with each other.

The contour plot of the transmission coefficient is shown in Figure 7.3(b) for the forward bias to gain a better insight of the hyperbolic modes. The hyperbolic dispersion curve is observed in the region from 0.17 eV to 0.19 eV (though it extends to about 0.2 eV) where HPhPs are excited. At small $k_{||}$ values, there is a bright spot near 0.17 eV which is attributed to frustrated modes in InSb. As mentioned previously, these modes give photon tunneling for $\hbar\omega$ from 0.15 eV to 0.17 eV, although with a lower transmission coefficient away from 0.17 eV. There exist propagating waves in InSb that can be tunneled through the vacuum gap at $k_{||} < n_1 k_0$ due to frustrated total internal reflection [2]. The hyperbolic modes support photon tunneling at high $k_{||}$ values, resulting in greater enhancement of the near-field heat flux [162]. Due to the shift of the bandgap, HPhPs cannot be excited in the reverse biased scenario.

Parametric sweeps were conducted to help understand the role of thicknesses and vacuum gap on the performance of the proposed photonic thermal diode. The calculation results show that the effect of the InSb thickness is small. When $h_1 > 10$ μm, the heat fluxes and rectification ratio are almost constant. Therefore, $h_1 = 100$ μm is used in all calculations without further discussion. The effects of d and h_2 on the rectification ratio are shown in Figure 7.4 for the two terminal temperatures of 400 K and 200 K. In general, reducing d gives rise to the forward heat flux, resulting in a higher rectification ratio. From practical consideration,

the smallest d value is taken to be 10 nm. When d is increased to 50 nm, the rectification ratio reduces to less than 2. As h_2 increases, R increases and reaches a plateau for small d values. For d = 10 nm, R reaches a maximum at h_2 = 5 nm and decreases slightly as h_2 increases. Even when h_2 = 1000 nm, the rectification ratio is greater than 15.4. For d = 20 nm, the R = 4.54 (or rectification efficiency η = 0.82) at h_2 = 10 nm.

It can be seen from Figure 7.2 that the rectification ratio increases with the temperature difference. Furthermore, the average temperature may also affect the photonic thermal diode performance. In Figure 7.5, the forward and reverse heat fluxes and the rectification ratio are plotted as a function of the absolute temperature difference for T_{avg} =

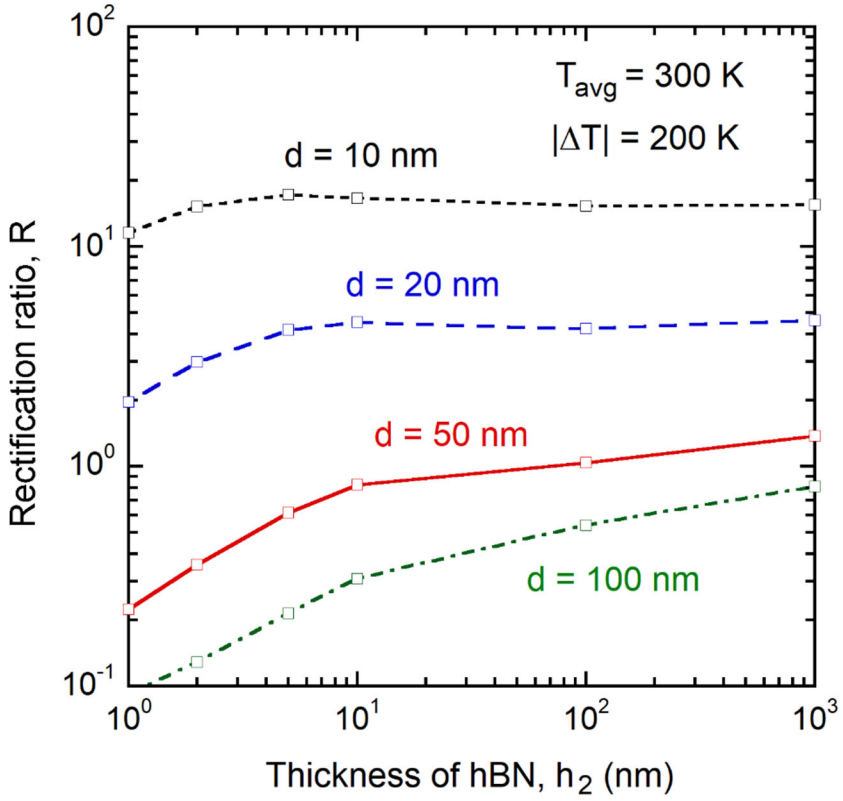

Figure 7.4 Rectification ratio vs the thickness of hBN films at different vacuum gap distances, when the thickness of InSb is fixed at 100 μm for ΔT = 200 K and T_{avg} = 300 K.

300 K, 350 K and 400 K. The lower and upper temperature limits are set as 50 and 600 K, respectively. Therefore, the maximum $|\Delta T|$ is set to 500 K for T_{avg} = 300 and 350 K, and 400 K for T_{avg} = 400 K. As shown in Figure 7.1(c), as the temperature increases, the band edge of InSb moves toward lower frequencies and starts to overlap with the hBN hyperbolic band. The coupling becomes stronger when the temperature of InSb increases to beyond 300 K where $E_g \approx 0.175$ eV. For T_{avg} = 300 K, the rectification ratio exceeds 10 when the lower temperature terminal is below about 240 K at which $E_g \approx 0.19$ eV is near the peak of the spectral heat flux as shown in Figure 7.3(a). This explains why the rectification ratio is smaller for higher T_{avg} when $|\Delta T|$ is relatively small. Crossovers occur as $|\Delta T|$ increases, and the highest rectification ratio for $|\Delta T| = 400$ K occurs at T_{avg} = 400 K where R = 36.7 and $q_f = 1.57 \times 10^5$ W/m^2, which is 21.6 times that between two blackbodies at 600 and 200 K. For T_{avg} = 350 K and $|\Delta T| = 500$ K, the rectification ratio is close to 38. When T_1 is increased from 400 and 600 K, the absorption coefficient of InSb increases, which subsequently enhances the coupling with the hBN hyperbolic band. The rectification ratios obtained from this study exceed the literature values between planar as well as grating structures in the similar temperature range. Compared to the photonic thermal diode employing PCMs, the proposed device can afford a wider range of working temperatures with higher rectification ratios when operated at nanoscale vacuum gaps.

The model given in Eq. (5) neglects the absorption of InSb completely below the bandgap. There are three absorption mechanisms that should be considered in practice. The optical phonon of InSb is in the far infrared at $\hbar\omega \approx$ 0.024 eV. It does not overlap with the hBN absorption bands and hence should be negligible. Free carriers contribute to sub-

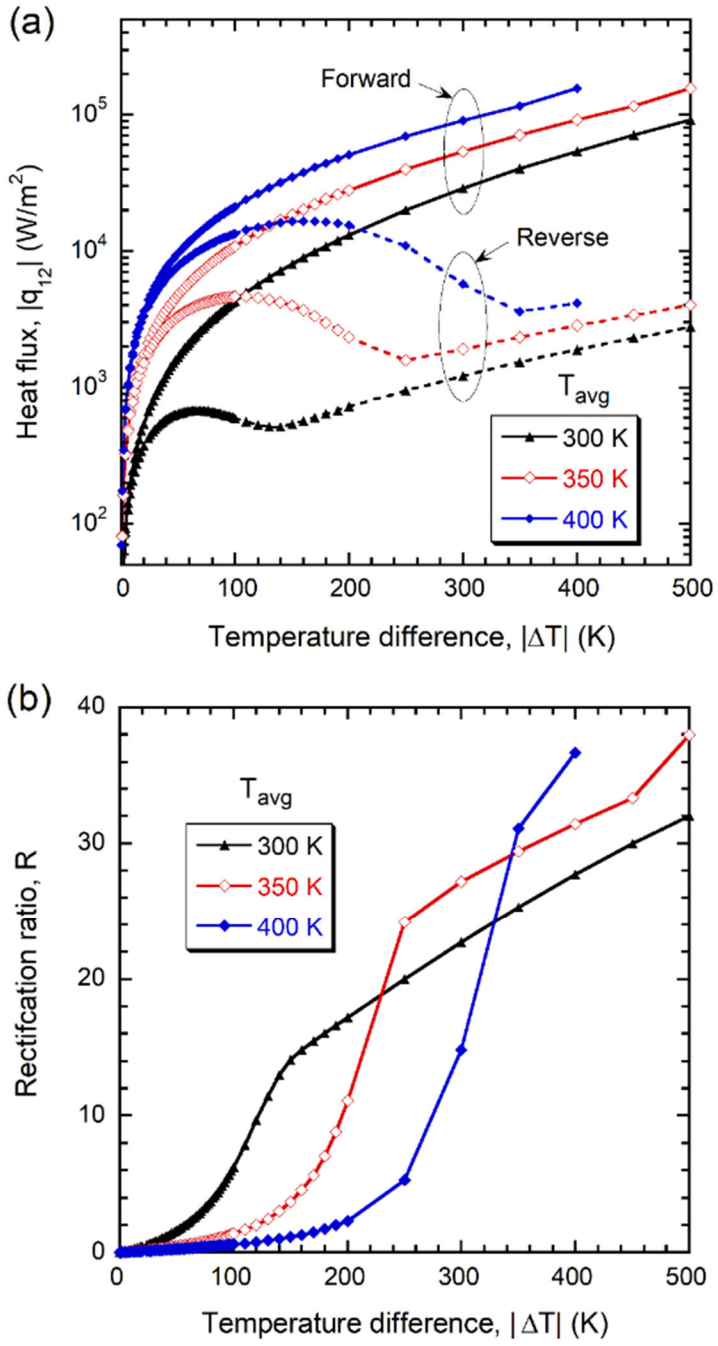

Figure 7.5 (a) The net heat flux and (b) rectification ratios verse the temperature difference of the near-field photonic thermal diode at T_{avg} of 300, 350, and 400 K, the other conditions are the same as in Figure 7.2.

bandgap absorption, especially above room temperature [229]. By setting $\alpha = 5$ cm^{-1} and 10 cm^{-1} at $\omega < \omega_g$, the rectification ratios for $T_{avg} = 300$ K and $\Delta T = 200$ K reduce by 11% and 17%, respectively; this is mainly due to the increase in the reverse heat flux. It should be noted that for the reverse bias, InSb is at the lower temperature side, and therefore, the effect of free carriers should be smaller than 10%. Another effect is the Ürbach tail, since the absorption coefficient does not drop suddenly to zero right below the bandgap. This issue is complicated because of inconsistencies in the measurements.[42] According to Kurnick and Powell [239], the absorption coefficient drops from 100 to 1 cm^{-1} within 0.01 eV at 78 K. Therefore, including a Ürbach tail should not significantly impact the performance. Further improvement could be made by using a more realistic model that fits the temperature-dependent absorption coefficients of InSb.

In summary, a near-field photonic thermal diode is proposed by coupling the interband absorption of an InSb film with the HPhPs in a hBN sheet. The temperature dependence of the band edge absorption of InSb enables the thermal diode behavior. A high rectification ratio of more than 17 is predicted at a 200 K temperature difference with an average temperature of 300 K. When the average temperature is increased to 350 K for a temperature difference of 500 K, calculations show that the rectification ratio is near 38. This work theoretically demonstrates a promising mechanism to achieve photonic thermal rectification with large rectification ratios without patterning.

7.2 A Near-Field Thermoradiative Device

A TR cell generate electricity by emitting out photons above bandgap energy. Similar to an ideal TPV or PV cell, an ideal TR cell can exhibit a high performance when the sub-

bandgap emission is suppressed and above-bandgap photon emission concentrates in a spectrum close to bandgap energy. If we investigated the spectral heat flux of the forward bias case of the photonic thermal diode shown in Figure 7.3(a), most of the radiative heat flux are carried by the photons with energies larger than and close to the bandgap of InSb [240]. Because of this spectral matching of interband transition of InSb and hyperbolic band of hBN, this structure is a well-designed near-field TR device. However, to improve the photon fraction above bandgap energy and reduce the nonradiative processes, a thin-film InSb is usually preferred for a TR device [10, 125, 241]. Therefore, a 50 nm InSb thin-film is selected as the

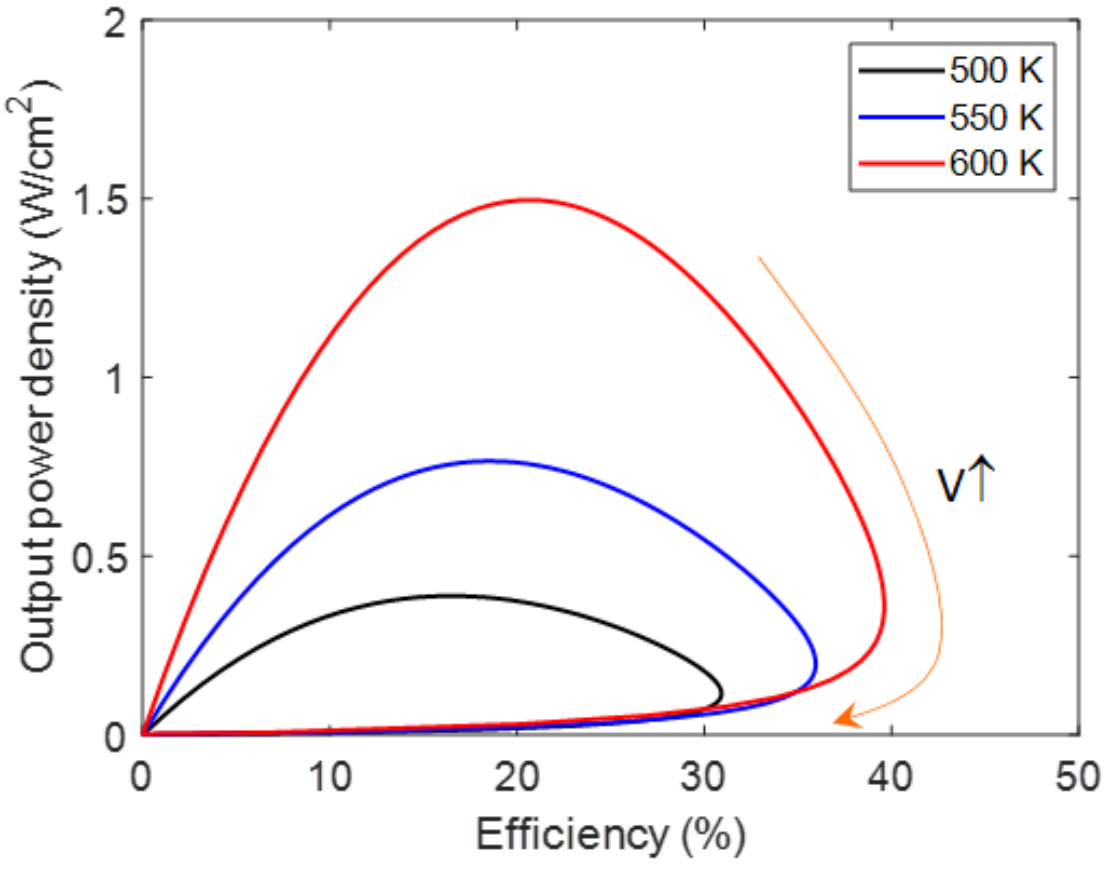

Figure 7.6 The η-P curves of the near-field thermoradiative device at different working temperatures (T_1 = 500 K, 550 K, and 600 K).

TR cell, while the thickness of hBN and vacuum spacing is fixed at 5 nm and 10 nm, respectively. A multilayer FE for a uniaxial anisroptic stratified medium is applied to calculate the film absorption [242]. The device performance is calculated by detailed balance analysis without considering the nonradiative processes. The efficiency-power density characteristic (i.e., the η-P curves) are shown for different working temperatures in Figure 7.6. The optimal efficiency of this near-field TR cell can reach 40% when the temperature of the hot side is 600 K. While the optimal output power density can achieve as large as 1.5 W/cm^2, which exceeds any TR devices in the literatures. A parametric study is required to further demonstrate the performance of this near-field thermoradiative device with the consideration of spatial effect on the ERRC [243].

CHAPTER 8. CONCLUSIONS AND FUTURE WORK

This dissertation studies the unique phenomena of the photon and charge transport in semiconductor radiative energy converters at micro/nanoscales. A photon-charge coupled model is summarized as a promising and comprehensive modeling method to characterize the performance of different kinds of radiative energy converters for both far- and near-field operation conditions. The significance of the photon chemical potential on the performance of radiative energy converters working at near-field regimes is theoretically demonstrated, especially for near-field TPV devices. The application of the fluctuational electrodynamics (FE) in the modeling of radiative energy converters are critical, since conventional assumptions and modeling methods are demonstrated invalid at micro/nanoscales. The employment of 2D materials in the radiative energy converters and photonic thermal diodes can greatly enhance the performance of these near-field optoelectronic devices.

The photon-charge coupled transport phenomenon of near-field radiative energy converters can be detailed characterized by the iterative modeling method combining the drift-diffusion equations and FE for electrical and optical processes modeling, respectively. The spatial profile of the photon chemical potential is calculated for two near-field TPV cells, which illustrates zero or constant photon chemical potential are not valid to capture the effect of charge distribution inside the semiconductor devices. The difference between the results obtained by the iterative solver and detailed balance analysis with the two conventional assumptions demonstrates the limitation of the conventional modeling approaches. At high-level injection for a thin-film near-field TPV cell, the photon chemical

potential is higher than the value of the working bias. The criterion of noticeable effect brought by photon chemical potential is discussed for different semiconductor materials and emitter temperatures.

The effect of evanescent waves on the dark current of a near-field TPV cell is essentially the near-field effect on the external luminescence, which is a common phenomenon existing in a working radiative energy converter. When the cell thickness is less than 1 μm, van Roosbroeck-Shockley model could possibly underestimate the total external radiative recombination rate, which is only fifth of the result calculated by FE for thin-film radiative energy converters. The calculation of the local ERRC can guide the design and optimization of thin-film radiative energy converters. By introduction of IIQE, the thermal and nonthermal radiation are quantitatively distinguished at the spectrum larger than the bandgap energy. The importance of IIQE is illustrated by investigating the doping effect on the local ERRC.

A near-field photonic thermal diode using hBN and InSb is demonstrated a high rectification ratio. This work makes a major contribution in thermal circuit and thermal management community by providing a novel mechanism to achieve thermal diodes. A preliminary calculation is also presented to demonstrate the realization of a near-field TR device using the same structure and materials. It is intriguing to further improve the performance of existing radiative energy converters or even develop new optoelectronic devices enabled by the coupling between 2D materials and semiconductors.

REFERENCES

[1] P. Wurfel, The Chemical Potential of Radiation, *Journal of Physics C: Solid State Physics*, Vol. 15, pp. 3967-3985, 1982.

[2] Z. M. Zhang, Nano/Microscale Heat Transfer, Springer Cham, 2020.

[3] M. Planck, The Theory of Heat Radiation, Courier Corporation, 2013.

[4] S. V. Boriskina, J. K. Tong, W.-C. Hsu, B. Liao, Y. Huang, V. Chiloyan, and G. Chen, Heat Meets Light on the Nanoscale, *Nanophotonics*, Vol. 5, p. 134, 2016.

[5] E. Tervo, E. Bagherisereshki, and Z. Zhang, Near-Field Radiative Thermoelectric Energy Converters: A Review, *Frontiers in Energy*, Vol. 12, pp. 5-21, 2018.

[6] P. Würfel and U. Würfel, Physics of Solar Cells: From Basic Principles to Advanced Concepts, John Wiley & Sons, 2016.

[7] B. Zhao and S. Fan, Chemical Potential of Photons and Its Implications for Controlling Radiative Heat Transfer, *Annual Review of Heat Transfer*, Vol. 23, 2020.

[8] B. Zhao, K. Chen, S. Buddhiraju, G. Bhatt, M. Lipson, and S. Fan, High-Performance Near-Field Thermophotovoltaics for Waste Heat Recovery, *Nano Energy*, Vol. 41, pp. 344-350, 2017.

[9] X. Liu and Z. M. Zhang, High-Performance Electroluminescent Refrigeration Enabled by Photon Tunneling, *Nano Energy*, Vol. 26, pp. 353-359, 2016.

[10] W.-C. Hsu, J. K. Tong, B. Liao, Y. Huang, S. V. Boriskina, and G. Chen, Entropic and Near-Field Improvements of Thermoradiative Cells, *Scientific Reports*, Vol. 6, p. 34837, 2016.

[11] K. Chen, P. Santhanam, and S. Fan, Near-Field Enhanced Negative Luminescent Refrigeration, *Physical Review Applied*, Vol. 6, p. 024014, 2016.

[12] B. Bitnar, W. Durisch, and R. Holzner, Thermophotovoltaics on the Move to Applications, *Applied Energy*, Vol. 105, pp. 430-438, 2013.

[13] A. Datas and A. Martí, Thermophotovoltaic Energy in Space Applications: Review and Future Potential, *Solar Energy Materials and Solar Cells*, Vol. 161, pp. 285-296, 2017.

[14] E. J. Tervo, W. A. Callahan, E. S. Toberer, M. A. Steiner, and A. J. Ferguson, Solar Thermoradiative-Photovoltaic Energy Conversion, *Cell Reports Physical Science*, Vol. 1, p. 100258, 2020.

[15] V. L. Teofilo, P. Choong, J. Chang, Y. L. Tseng, and S. Ermer, Thermophotovoltaic Energy Conversion for Space, *The Journal of Physical Chemistry C*, Vol. 112, pp. 7841-7845, 2008.

[16] Z. Zhou, E. Sakr, Y. Sun, and P. Bermel,2016, "Solar Thermophotovoltaics: Reshaping the Solar Spectrum," in Nanophotonics **5**, ed, p. 1.

[17] K. F. Mustafa, S. Abdullah, M. Z. Abdullah, and K. Sopian, A Review of Combustion-Driven Thermoelectric (TE) and Thermophotovoltaic (TPV) Power Systems, *Renewable and Sustainable Energy Reviews*, Vol. 71, pp. 572-584, 2017.

[18] G. Wehmeyer, T. Yabuki, C. Monachon, J. Wu, and C. Dames, Thermal Diodes, Regulators, and Switches: Physical Mechanisms and Potential Applications, *Applied Physics Reviews*, Vol. 4, p. 041304, 2017.

[19] D. Polder and M. Van Hove, Theory of Radiative Heat Transfer between Closely Spaced Bodies, *Physical Review B*, Vol. 4, pp. 3303-3314, 1971.

[20] J. B. Pendry, Radiative Exchange of Heat between Nanostructures, *Journal of Physics: Condensed Matter*, Vol. 11, pp. 6621-6633, 1999.

[21] K. Joulain, J.-P. Mulet, F. Marquier, R. Carminati, and J.-J. Greffet, Surface Electromagnetic Waves Thermally Excited: Radiative Heat Transfer, Coherence Properties and Casimir Forces Revisited in the Near Field, *Surface Science Reports*, Vol. 57, pp. 59-112, 2005.

[22] S. Basu, Z. M. Zhang, and C. J. Fu, Review of Near-Field Thermal Radiation and Its Application to Energy Conversion, *International Journal of Energy Research*, Vol. 33, pp. 1203-1232, 2009.

[23] S.-A. Biehs, P. Ben-Abdallah, and F. S. Rosa, Nanoscale Radiative Heat Transfer and Its Applications, *Infrared Radiation*, pp. 1-26, 2012.

[24] G. Chen, Nanoscale Energy Transport and Conversion: A Parallel Treatment of Electrons, Molecules, Phonons, and Photons, Oxford university press, 2005.

[25] J. J. Loomis and H. J. Maris, Theory of Heat Transfer by Evanescent Electromagnetic Waves, *Physical Review B*, Vol. 50, pp. 18517-18524, 1994.

[26] Y. Xuan, An Overview of Micro/Nanoscaled Thermal Radiation and Its Applications, *Photonics and Nanostructures - Fundamentals and Applications*, Vol. 12, pp. 93-113, 2014.

[27] B. Song, A. Fiorino, E. Meyhofer, and P. Reddy, Near-Field Radiative Thermal Transport: From Theory to Experiment, *AIP Advances*, Vol. 5, p. 053503, 2015.

[28] S. M. Rytov, Y. A. Kravtsov, and V. I. Tatarskii, Priniciples of Statistical Radiophysics. 3. Elements of Random Fields, *Priniciples of statistical*

radiophysics. 3. Elements of random fields., by Rytov, SM; Kravtsov, YA; Tatarskii, VI. Springer, Berlin (Germany, FR), 1989, 249 p., ISBN 3-540-17829-5, 1989.

[29] M. Francoeur, M. P. Mengüç, and R. Vaillon, Spectral Tuning of Near-Field Radiative Heat Flux between Two Thin Silicon Carbide Films, *Journal of Physics D: Applied Physics*, Vol. 43, p. 075501, 2010.

[30] C. J. Fu and Z. M. Zhang, Nanoscale Radiation Heat Transfer for Silicon at Different Doping Levels, *International Journal of Heat and Mass Transfer*, Vol. 49, pp. 1703-1718, 2006.

[31] P.-O. Chapuis, S. Volz, C. Henkel, K. Joulain, and J.-J. Greffet, Effects of Spatial Dispersion in Near-Field Radiative Heat Transfer between Two Parallel Metallic Surfaces, *Physical Review B*, Vol. 77, p. 035431, 2008.

[32] M. Francoeur and M. Pinar Mengüç, Role of Fluctuational Electrodynamics in Near-Field Radiative Heat Transfer, *Journal of Quantitative Spectroscopy and Radiative Transfer*, Vol. 109, pp. 280-293, 2008.

[33] M. Francoeur, M. Pinar Mengüç, and R. Vaillon, Solution of Near-Field Thermal Radiation in One-Dimensional Layered Media Using Dyadic Green's Functions and the Scattering Matrix Method, *Journal of Quantitative Spectroscopy and Radiative Transfer*, Vol. 110, pp. 2002-2018, 2009.

[34] S. A. Biehs, Thermal Heat Radiation, Near-Field Energy Density and Near-Field Radiative Heat Transfer of Coated Materials, *The European Physical Journal B*, Vol. 58, pp. 423-431, 2007.

[35] M. Francoeur, M. P. Mengüç, and R. Vaillon, Near-Field Radiative Heat Transfer Enhancement via Surface Phonon Polaritons Coupling in Thin Films, *Applied Physics Letters*, Vol. 93, p. 043109, 2008.

[36] C. J. Fu and W. C. Tan, Near-Field Radiative Heat Transfer between Two Plane Surfaces with One Having a Dielectric Coating, *Journal of Quantitative Spectroscopy and Radiative Transfer*, Vol. 110, pp. 1027-1036, 2009.

[37] J.-P. Mulet, K. Joulain, R. Carminati, and J.-J. Greffet, Nanoscale Radiative Heat Transfer between a Small Particle and a Plane Surface, *Applied Physics Letters*, Vol. 78, pp. 2931-2933, 2001.

[38] S.-A. Biehs, O. Huth, and F. Rüting, Near-Field Radiative Heat Transfer for Structured Surfaces, *Physical Review B*, Vol. 78, p. 085414, 2008.

[39] C. Otey and S. Fan, Numerically Exact Calculation of Electromagnetic Heat Transfer between a Dielectric Sphere and Plate, *Physical Review B*, Vol. 84, p. 245431, 2011.

[40] A. I. Volokitin and B. N. J. Persson, Radiative Heat Transfer between Nanostructures, *Physical Review B*, Vol. 63, p. 205404, 2001.

[41] A. P. Mccauley, M. T. H. Reid, M. Krüger, and S. G. Johnson, Modeling Near-Field Radiative Heat Transfer from Sharp Objects Using a General Three-Dimensional Numerical Scattering Technique, *Physical Review B*, Vol. 85, p. 165104, 2012.

[42] A. Narayanaswamy and G. Chen, Thermal Near-Field Radiative Transfer between Two Spheres, *Physical Review B*, Vol. 77, p. 075125, 2008.

[43] P.-O. Chapuis, M. Laroche, S. Volz, and J.-J. Greffet, Radiative Heat Transfer between Metallic Nanoparticles, *Applied Physics Letters*, Vol. 92, p. 201906, 2008.

[44] C. R. Otey, L. Zhu, S. Sandhu, and S. Fan, Fluctuational Electrodynamics Calculations of Near-Field Heat Transfer in Non-Planar Geometries: A Brief Overview, *Journal of Quantitative Spectroscopy and Radiative Transfer*, Vol. 132, pp. 3-11, 2014.

[45] A. G. Polimeridis, M. T. H. Reid, W. Jin, S. G. Johnson, J. K. White, and A. W. Rodriguez, Fluctuating Volume-Current Formulation of Electromagnetic Fluctuations in Inhomogeneous Media: Incandescence and Luminescence in Arbitrary Geometries, *Physical Review B*, Vol. 92, p. 134202, 2015.

[46] C. M. Hargreaves, Anomalous Radiative Transfer between Closely-Spaced Bodies, *Physics Letters A*, Vol. 30, pp. 491-492, 1969.

[47] G. A. Domoto, R. F. Boehm, and C. L. Tien, Experimental Investigation of Radiative Transfer between Metallic Surfaces at Cryogenic Temperatures, *Journal of Heat Transfer*, Vol. 92, pp. 412-416, 1970.

[48] E. G. Cravalho, C. L. Tien, and R. P. Caren, Effect of Small Spacings on Radiative Transfer between Two Dielectrics, *Journal of Heat Transfer*, Vol. 89, pp. 351-358, 1967.

[49] C. M. Hargreaves, Radiative Transfer between Closely Spaced Bodies, NV Philips' Gloeilampenfabrieken, 1973.

[50] N. Borisevich, S. Blinov, A. Dorokhin, G. Zalesskaya, and A. Kotov, Effect of Magnitude of Gap between Metal Plates on Their Thermal Interaction at Cryogenic Temperatures, in *Soviet Physics Doklady*, p. 575, 1978.

[51] L. Hu, A. Narayanaswamy, X. Chen, and G. Chen, Near-Field Thermal Radiation between Two Closely Spaced Glass Plates Exceeding Planck's Blackbody Radiation Law, *Applied Physics Letters*, Vol. 92, p. 133106, 2008.

[52] S. Shen, A. Mavrokefalos, P. Sambegoro, and G. Chen, Nanoscale Thermal Radiation between Two Gold Surfaces, *Applied Physics Letters*, Vol. 100, p. 233114, 2012.

[53] J. I. Watjen, B. Zhao, and Z. M. Zhang, Near-Field Radiative Heat Transfer between Doped-Si Parallel Plates Separated by a Spacing Down to 200 nm, *Applied Physics Letters*, Vol. 109, p. 203112, 2016.

[54] S. Shen, A. Narayanaswamy, and G. Chen, Surface Phonon Polaritons Mediated Energy Transfer between Nanoscale Gaps, *Nano Letters*, Vol. 9, pp. 2909-2913, 2009.

[55] E. Rousseau, A. Siria, G. Jourdan, S. Volz, F. Comin, J. Chevrier, and J.-J. Greffet, Radiative Heat Transfer at the Nanoscale, *Nature Photonics*, Vol. 3, pp. 514-517, 2009.

[56] B. Song, Y. Ganjeh, S. Sadat, D. Thompson, A. Fiorino, V. Fernández-Hurtado, J. Feist, F. J. Garcia-Vidal, J. C. Cuevas, P. Reddy, and E. Meyhofer, Enhancement of Near-Field Radiative Heat Transfer Using Polar Dielectric Thin Films, *Nature Nanotechnology*, Vol. 10, pp. 253-258, 2015.

[57] A. Kittel, W. Müller-Hirsch, J. Parisi, S.-A. Biehs, D. Reddig, and M. Holthaus, Near-Field Heat Transfer in a Scanning Thermal Microscope, *Physical Review Letters*, Vol. 95, p. 224301, 2005.

[58] K. Kim, B. Song, V. Fernández-Hurtado, W. Lee, W. Jeong, L. Cui, D. Thompson, J. Feist, M. T. H. Reid, F. J. García-Vidal, J. C. Cuevas, E. Meyhofer, and P. Reddy, Radiative Heat Transfer in the Extreme Near Field, *Nature*, Vol. 528, pp. 387-391, 2015.

[59] K. Kloppstech, N. Könne, S.-A. Biehs, A. W. Rodriguez, L. Worbes, D. Hellmann, and A. Kittel, Giant Heat Transfer in the Crossover Regime between Conduction and Radiation, *Nature Communications*, Vol. 8, p. 14475, 2017.

[60] A. Fiorino, D. Thompson, L. Zhu, B. Song, P. Reddy, and E. Meyhofer, Giant Enhancement in Radiative Heat Transfer in Sub-30 nm Gaps of Plane Parallel Surfaces, *Nano Letters*, Vol. 18, pp. 3711-3715, 2018.

[61] M. Lim, S. S. Lee, and B. J. Lee, Near-Field Thermal Radiation between Doped Silicon Plates at Nanoscale Gaps, *Physical Review B*, Vol. 91, p. 195136, 2015.

[62] R. S. Ottens, V. Quetschke, S. Wise, A. A. Alemi, R. Lundock, G. Mueller, D. H. Reitze, D. B. Tanner, and B. F. Whiting, Near-Field Radiative Heat Transfer between Macroscopic Planar Surfaces, *Physical Review Letters*, Vol. 107, p. 014301, 2011.

[63] B. Song, D. Thompson, A. Fiorino, Y. Ganjeh, P. Reddy, and E. Meyhofer, Radiative Heat Conductances between Dielectric and Metallic Parallel Plates with Nanoscale Gaps, *Nature Nanotechnology*, Vol. 11, pp. 509-514, 2016.

[64] M. Ghashami, H. Geng, T. Kim, N. Iacopino, S. K. Cho, and K. Park, Precision Measurement of Phonon-Polaritonic Near-Field Energy Transfer between Macroscale Planar Structures under Large Thermal Gradients, *Physical Review Letters*, Vol. 120, p. 175901, 2018.

[65] J. Desutter, L. Tang, and M. Francoeur, A Near-Field Radiative Heat Transfer Device, *Nature Nanotechnology*, Vol. 14, pp. 751-755, 2019.

[66] S. Lang, G. Sharma, S. Molesky, P. U. Kränzien, T. Jalas, Z. Jacob, A. Y. Petrov, and M. Eich, Dynamic Measurement of near-Field Radiative Heat Transfer, *Scientific Reports*, Vol. 7, p. 13916, 2017.

[67] M. P. Bernardi, D. Milovich, and M. Francoeur, Radiative Heat Transfer Exceeding the Blackbody Limit between Macroscale Planar Surfaces Separated by a Nanosize Vacuum Gap, *Nature Communications*, Vol. 7, p. 12900, 2016.

[68] K. Ito, A. Miura, H. Iizuka, and H. Toshiyoshi, Parallel-Plate Submicron Gap Formed by Micromachined Low-Density Pillars for Near-Field Radiative Heat Transfer, *Applied Physics Letters*, Vol. 106, p. 083504, 2015.

[69] R. St-Gelais, L. Zhu, S. Fan, and M. Lipson, Near-Field Radiative Heat Transfer between Parallel Structures in the Deep Subwavelength Regime, *Nature Nanotechnology*, Vol. 11, pp. 515-519, 2016.

[70] T. Kralik, P. Hanzelka, M. Zobac, V. Musilova, T. Fort, and M. Horak, Strong Near-Field Enhancement of Radiative Heat Transfer between Metallic Surfaces, *Physical Review Letters*, Vol. 109, p. 224302, 2012.

[71] J. Yang, W. Du, Y. Su, Y. Fu, S. Gong, S. He, and Y. Ma, Observing of the Super-Planckian Near-Field Thermal Radiation between Graphene Sheets, *Nature Communications*, Vol. 9, p. 4033, 2018.

[72] M. Ghashami, A. Jarzembski, M. Lim, B. J. Lee, and K. Park, Experimental Exploration of near-Field Radiative Heat Transfer, *Annual Review of Heat Transfer*, Vol. 23, 2020.

[73] M. D. Whale and E. G. Cravalho, Modeling and Performance of Microscale Thermophotovoltaic Energy Conversion Devices, *IEEE Transactions on Energy Conversion*, Vol. 17, pp. 130-142, 2002.

[74] M. Laroche, R. Carminati, and J.-J. Greffet, Near-Field Thermophotovoltaic Energy Conversion, *Journal of Applied Physics*, Vol. 100, p. 063704, 2006.

[75] K. Park, S. Basu, W. P. King, and Z. M. Zhang, Performance Analysis of Near-Field Thermophotovoltaic Devices Considering Absorption Distribution, *Journal of Quantitative Spectroscopy and Radiative Transfer*, Vol. 109, pp. 305-316, 2008.

[76] M. Francoeur, R. Vaillon, and M. P. Mengüç, Thermal Impacts on the Performance of Nanoscale-Gap Thermophotovoltaic Power Generators, *IEEE Transactions on Energy Conversion*, Vol. 26, pp. 686-698, 2011.

[77] A. Narayanaswamy and G. Chen, Surface Modes for Near Field Thermophotovoltaics, *Applied Physics Letters*, Vol. 82, pp. 3544-3546, 2003.

[78] M. P. Bernardi, O. Dupré, E. Blandre, P.-O. Chapuis, R. Vaillon, and M. Francoeur, Impacts of Propagating, Frustrated and Surface Modes on Radiative, Electrical and Thermal Losses in Nanoscale-Gap Thermophotovoltaic Power Generators, *Scientific Reports*, Vol. 5, p. 11626, 2015.

[79] J. Desutter, R. Vaillon, and M. Francoeur, External Luminescence and Photon Recycling in Near-Field Thermophotovoltaics, *Physical Review Applied*, Vol. 8, p. 014030, 2017.

[80] E. Blandre, P.-O. Chapuis, and R. Vaillon, High-Injection Effects in Near-Field Thermophotovoltaic Devices, *Scientific Reports*, Vol. 7, p. 15860, 2017.

[81] D. Feng, E. J. Tervo, S. K. Yee, and Z. M. Zhang, Effect of Evanescent Waves on the Dark Current of Thermophotovoltaic Cells, *Nanoscale and Microscale Thermophysical Engineering*, Vol. 24, pp. 1-19, 2020.

[82] W. A. Callahan, D. Feng, Z. M. Zhang, E. S. Toberer, A. J. Ferguson, and E. J. Tervo, Coupled Charge and Radiation Transport Processes in Thermophotovoltaic and Thermoradiative Cells, *Physical Review Applied*, Vol. 15, p. 054035, 2021.

[83] D. Feng, E. J. Tervo, D. Vasileska, S. K. Yee, A. Rohatgi, and Z. M. Zhang, Spatial Profiles of Photon Chemical Potential in Near-Field Thermophotovoltaic Cells, *Journal of Applied Physics*, Vol. 129, p. 213101, 2021.

[84] B. Li, Q. Cheng, J. Song, K. Zhou, L. Lu, and Z. Luo, Evaluation of Performance of Near-Field Thermophotovoltaic Systems Based on Entropy Analysis, *Journal of Applied Physics*, Vol. 127, p. 063103, 2020.

[85] J. L. Pan, H. K. H. Choy, and C. G. Fonstad, Very Large Radiative Transfer over Small Distances from a Black Body for Thermophotovoltaic Applications, *IEEE Transactions on Electron Devices*, Vol. 47, pp. 241-249, 2000.

[86] K. Chen, P. Santhanam, and S. Fan, Suppressing Sub-Bandgap Phonon-Polariton Heat Transfer in Near-Field Thermophotovoltaic Devices for Waste Heat Recovery, *Applied Physics Letters*, Vol. 107, p. 091106, 2015.

[87] A. Karalis and J. D. Joannopoulos, Temporal Coupled-Mode Theory Model for Resonant Near-Field Thermophotovoltaics, *Applied Physics Letters*, Vol. 107, p. 141108, 2015.

[88] O. Ilic, M. Jablan, J. D. Joannopoulos, I. Celanovic, and M. Soljačić, Overcoming the Black Body Limit in Plasmonic and Graphene Near-Field Thermophotovoltaic Systems, *Optics Express*, Vol. 20, pp. A366-A384, 2012.

[89] R. Messina and P. Ben-Abdallah, Graphene-Based Photovoltaic Cells for near-Field Thermal Energy Conversion, *Scientific Reports*, Vol. 3, p. 1383, 2013.

[90] V. B. Svetovoy and G. Palasantzas, Graphene-on-Silicon Near-Field Thermophotovoltaic Cell, *Physical Review Applied*, Vol. 2, p. 034006, 2014.

[91] M. Lim, S. Jin, S. S. Lee, and B. J. Lee, Graphene-Assisted Si-InSb Thermophotovoltaic System for Low Temperature Applications, *Optics Express*, Vol. 23, pp. A240-A253, 2015.

[92] T. Liao and Z.-Y. Wang, Graphene/N-Type Silicon Schottky Near-Field Thermophotovoltaic Cell, *Journal of Photonics for Energy*, Vol. 9, p. 014502, 2019.

[93] S. Jin, M. Lim, S. S. Lee, and B. J. Lee, Hyperbolic Metamaterial-Based Near-Field Thermophotovoltaic System for Hundreds of Nanometer Vacuum Gap, *Optics Express*, Vol. 24, pp. A635-A649, 2016.

[94] Q. Xu, P. Chen, X. Wu, and Q. Cai, Performance Analysis of a Metamaterial-Based Near-Field Thermophotovoltaic System Considering Cooling System Energy Consumption, *International Journal of Thermophysics*, Vol. 40, p. 30, 2019.

[95] R. Wang, J. Lu, and J.-H. Jiang, Enhancing Thermophotovoltaic Performance Using Graphene-BN-InSb Near-Field Heterostructures, *Physical Review Applied*, Vol. 12, p. 044038, 2019.

[96] J. K. Tong, W.-C. Hsu, Y. Huang, S. V. Boriskina, and G. Chen, Thin-Film 'Thermal Well' Emitters and Absorbers for High-Efficiency Thermophotovoltaics, *Scientific Reports*, Vol. 5, p. 10661, 2015.

[97] A. Karalis and J. D. Joannopoulos, 'Squeezing' Near-Field Thermal Emission for Ultra-Efficient High-Power Thermophotovoltaic Conversion, *Scientific Reports*, Vol. 6, p. 28472, 2016.

[98] J. Z.-J. Lau and B. T. Wong, Thermal Energy Conversion Using Near-Field Thermophotovoltaic Device Composed of a Thin-Film Tungsten Radiator and a Thin-Film Silicon Cell, *Journal of Applied Physics*, Vol. 122, p. 084302, 2017.

[99] N. Vongsoasup, M. Francoeur, and K. Hanamura, Performance Analysis of Near-Field Thermophotovoltaic System with 2D Grating Tungsten Radiator, *International Journal of Heat and Mass Transfer*, Vol. 115, pp. 326-332, 2017.

[100] J. I. Watjen, X. L. Liu, B. Zhao, and Z. M. Zhang, A Computational Simulation of Using Tungsten Gratings in Near-Field Thermophotovoltaic Devices, *Journal of Heat Transfer*, Vol. 139, 2017.

[101] P. Sabbaghi, Y. Yang, J.-Y. Chang, and L. Wang, Near-Field Thermophotovoltaic Energy Conversion by Excitation of Magnetic Polariton inside Nanometric Vacuum Gaps with Nanostructured Drude Emitter and Backside Reflector, *Journal of Quantitative Spectroscopy and Radiative Transfer*, Vol. 234, pp. 108-114, 2019.

[102] S. Molesky and Z. Jacob, Ideal Near-Field Thermophotovoltaic Cells, *Physical Review B*, Vol. 91, p. 205435, 2015.

[103] J.-Y. Chang, Y. Yang, and L. Wang, Tungsten Nanowire Based Hyperbolic Metamaterial Emitters for Near-Field Thermophotovoltaic Applications, *International Journal of Heat and Mass Transfer*, Vol. 87, pp. 237-247, 2015.

[104] Y. Guo, S. Molesky, H. Hu, C. L. Cortes, and Z. Jacob, Thermal Excitation of Plasmons for Near-Field Thermophotovoltaics, *Applied Physics Letters*, Vol. 105, p. 073903, 2014.

[105] M. Lim, J. Song, J. Kim, S. S. Lee, I. Lee, and B. J. Lee, Optimization of a Near-Field Thermophotovoltaic System Operating at Low Temperature and Large Vacuum Gap, *Journal of Quantitative Spectroscopy and Radiative Transfer*, Vol. 210, pp. 35-43, 2018.

[106] M. Lim, S. S. Lee, and B. J. Lee, Effects of Multilayered Graphene on the Performance of near-Field Thermophotovoltaic System at Longer Vacuum Gap Distances, *Journal of Quantitative Spectroscopy and Radiative Transfer*, Vol. 197, pp. 84-94, 2017.

[107] Y. Yang, J.-Y. Chang, P. Sabbaghi, and L. Wang, Performance Analysis of a near-Field Thermophotovoltaic Device with a Metallodielectric Selective Emitter and Electrical Contacts for the Photovoltaic Cell, *Journal of Heat Transfer*, Vol. 139, 2017.

[108] G. T. Papadakis, S. Buddhiraju, Z. Zhao, B. Zhao, and S. Fan, Broadening near-Field Emission for Performance Enhancement in Thermophotovoltaics, *Nano Letters*, Vol. 20, pp. 1654-1661, 2020.

[109] T. Inoue, K. Watanabe, T. Asano, and S. Noda, Near-Field Thermophotovoltaic Energy Conversion Using an Intermediate Transparent Substrate, *Optics Express*, Vol. 26, pp. A192-A208, 2018.

[110] F. R. Chen, Z. G. Xu, and Y. T. Wang, Near-Field Radiative Heat Transfer Enhancement in the Thermophotovoltaic System Using Hyperbolic Waveguides, *International Journal of Thermal Sciences*, Vol. 166, p. 106978, 2021.

[111] D. Feng, S. K. Yee, and Z. M. Zhang, Improved Performance of a Near-Field Thermophotovoltaic System by a Back Gapped Reflector, *arXiv preprint arXiv:2107.09772*, 2021.

[112] T. J. Bright, L. P. Wang, and Z. M. Zhang, Performance of Near-Field Thermophotovoltaic Cells Enhanced with a Backside Reflector, *Journal of Heat Transfer*, Vol. 136, 2014.

[113] R. St-Gelais, G. R. Bhatt, L. Zhu, S. Fan, and M. Lipson, Hot Carrier-Based Near-Field Thermophotovoltaic Energy Conversion, *ACS Nano*, Vol. 11, pp. 3001-3009, 2017.

[114] J. Song, M. Lim, S. S. Lee, and B. J. Lee, Analysis of Photocurrent Generation within a Schottky-Junction-Based Near-Field Thermophotovoltaic System, *Physical Review Applied*, Vol. 11, p. 044040, 2019.

[115] C. Jiang, H. Huang, and Z. Zhou, Enhancement in the Multi-Junction Thermophotovoltaic System Based on Near-Field Heat Transfer and Hyperbolic Metamaterial, *Solar Energy*, Vol. 217, pp. 390-398, 2021.

[116] R. S. Dimatteo, P. Greiff, S. L. Finberg, K. A. Young-Waithe, H. K. H. Choy, M. M. Masaki, and C. G. Fonstad, Enhanced Photogeneration of Carriers in a Semiconductor via Coupling across a Nonisothermal Nanoscale Vacuum Gap, *Applied Physics Letters*, Vol. 79, pp. 1894-1896, 2001.

[117] K. Hanamura and K. Mori, Nano-Gap TPV Generation of Electricity through Evanescent Wave in Near-Field above Emitter Surface, *AIP Conference Proceedings*, Vol. 890, pp. 291-296, 2007.

[118] T. Inoue, T. Koyama, D. D. Kang, K. Ikeda, T. Asano, and S. Noda, One-Chip Near-Field Thermophotovoltaic Device Integrating a Thin-Film Thermal Emitter and Photovoltaic Cell, *Nano Letters*, Vol. 19, pp. 3948-3952, 2019.

[119] T. Inoue, K. Ikeda, B. Song, T. Suzuki, K. Ishino, T. Asano, and S. Noda, Integrated Near-Field Thermophotovoltaic Device Overcoming Blackbody Limit, *ACS Photonics*, Vol. 8, pp. 2466-2472, 2021.

[120] A. Fiorino, L. Zhu, D. Thompson, R. Mittapally, P. Reddy, and E. Meyhofer, Nanogap Near-Field Thermophotovoltaics, *Nature Nanotechnology*, Vol. 13, pp. 806-811, 2018.

[121] C. Lucchesi, D. Cakiroglu, J.-P. Perez, T. Taliercio, E. Tournié, P.-O. Chapuis, and R. Vaillon, Near-Field Thermophotovoltaic Conversion with High Electrical Power

Density and Cell Efficiency above 14%, *Nano Letters*, Vol. 21, pp. 4524-4529, 2021.

[122] R. Mittapally, B. Lee, L. Zhu, A. Reihani, J. W. Lim, D. Fan, S. R. Forrest, P. Reddy, and E. Meyhofer, Near-Field Thermophotovoltaics for Efficient Heat to Electricity Conversion at High Power Density, *Nature Communications*, Vol. 12, p. 4364, 2021.

[123] C. Lin, B. Wang, K. H. Teo, and Z. Zhang, Performance Comparison between Photovoltaic and Thermoradiative Devices, *Journal of Applied Physics*, Vol. 122, p. 243103, 2017.

[124] B. Wang, C. Lin, K. H. Teo, and Z. Zhang, Thermoradiative Device Enhanced by Near-Field Coupled Structures, *Journal of Quantitative Spectroscopy and Radiative Transfer*, Vol. 196, pp. 10-16, 2017.

[125] A. Ghanekar, Y. Tian, X. Liu, and Y. Zheng, Performance Enhancement of near-Field Thermoradiative Devices Using Hyperbolic Metamaterials, *Journal of Photonics for Energy*, Vol. 9, p. 032706, 2019.

[126] C. Lin, B. Wang, K. H. Teo, and Z. Zhang, Near-Field Enhancement of Thermoradiative Devices, *Journal of Applied Physics*, Vol. 122, p. 143102, 2017.

[127] B. Li, Q. Cheng, J. Song, K. Zhou, L. Lu, Z. Luo, and X. Zhuo, Thermodynamic Bounds of Work and Efficiency in Near-Field Thermoradiative Systems, *International Journal of Heat and Mass Transfer*, Vol. 180, p. 121807, 2021.

[128] T. Liao, X. Zhang, Z. Yang, X. Chen, and J. Chen, Near-Field Thermoradiative Electron Device, *IEEE Transactions on Electron Devices*, Vol. 66, pp. 3099-3102, 2019.

[129] T. P. Xiao, K. Chen, P. Santhanam, S. Fan, and E. Yablonovitch, Electroluminescent Refrigeration by Ultra-Efficient GaAs Light-Emitting Diodes, *Journal of Applied Physics*, Vol. 123, p. 173104, 2018.

[130] T. P. Xiao, K. Chen, P. Santhanam, S. Fan, and E. Yablonovitch, Practical Efficiency Limits of Electroluminescent Cooling, SPIE, 2019.

[131] P. Han, K.-J. Jin, Y. Zhou, X. Wang, Z. Ma, S.-F. Ren, A. G. Mal'shukov, and K. A. Chao, Analysis of Optothermionic Refrigeration Based on Semiconductor Heterojunction, *Journal of Applied Physics*, Vol. 99, p. 074504, 2006.

[132] A. G. Mal'shukov and K. A. Chao, Opto-Thermionic Refrigeration in Semiconductor Heterostructures, *Physical Review Letters*, Vol. 86, pp. 5570-5573, 2001.

[133] G. C. Dousmanis, C. W. Mueller, H. Nelson, and K. G. Petzinger, Evidence of Refrigerating Action by Means of Photon Emission in Semiconductor Diodes, *Physical Review*, Vol. 133, pp. A316-A318, 1964.

[134] S.-T. Yen and K.-C. Lee, Analysis of Heterostructures for Electroluminescent Refrigeration and Light Emitting without Heat Generation, *Journal of Applied Physics*, Vol. 107, p. 054513, 2010.

[135] J. Piprek and Z.-M. Li, Electroluminescent Cooling Mechanism in InGaN/GaN Light-Emitting Diodes, *Optical and Quantum Electronics*, Vol. 48, p. 472, 2016.

[136] Z. Li, J. Xue, and R. Ram, A Design of a PhC-Enhanced LED for Electroluminescence Cooling, SPIE, 2017.

[137] T. P. Xiao, K. Chen, P. Santhanam, S. Fan, and E. Yablonovitch, Electro-Luminescent Refrigeration Enabled by Highly Efficient Photovoltaics, in *2017 IEEE 44th Photovoltaic Specialist Conference (PVSC)*, pp. 2185-2189, 2017.

[138] J. Wang, D. Ding, S. Yu, S. R. Johnson, and Y. Zhang, Electroluminescence Cooling in Semiconductors, in *2005 Quantum Electronics and Laser Science Conference*, pp. 655-657 Vol. 651, 2005.

[139] O. Heikkilä, J. Oksanen, and J. Tulkki, Ultimate Limit and Temperature Dependency of Light-Emitting Diode Efficiency, *Journal of Applied Physics*, Vol. 105, p. 093119, 2009.

[140] T. Sadi, I. Radevici, P. Kivisaari, and J. Oksanen, Electroluminescent Cooling in III–V Intracavity Diodes: Efficiency Bottlenecks, *IEEE Transactions on Electron Devices*, Vol. 66, pp. 2651-2656, 2019.

[141] D. J. G. Jr., P. Santhanam, and R. J. Ram, Design for Enhanced Thermo-Electric Pumping in Light Emitting Diodes, *Applied Physics Letters*, Vol. 103, p. 123503, 2013.

[142] J.-B. Wang, S. R. Johnson, D. Ding, S.-Q. Yu, and Y.-H. Zhang, Influence of Photon Recycling on Semiconductor Luminescence Refrigeration, *Journal of Applied Physics*, Vol. 100, p. 043502, 2006.

[143] K.-C. Lee and S.-T. Yen, Photon Recycling Effect on Electroluminescent Refrigeration, *Journal of Applied Physics*, Vol. 111, p. 014511, 2012.

[144] P. Santhanam, D. J. Gray, and R. J. Ram, Thermoelectrically Pumped Light-Emitting Diodes Operating above Unity Efficiency, *Physical Review Letters*, Vol. 108, p. 097403, 2012.

[145] A. Casado, I. Radevici, T. Sadi, and J. Oksanen, On the Temperature Dependence of the Efficiency of Electroluminescence, *Journal of Applied Physics*, Vol. 126, p. 173102, 2019.

[146] T. Sadi, P. Kivisaari, J. Tiira, I. Radevici, T. Haggren, and J. Oksanen, Electroluminescent Cooling in Intracavity Light Emitters: Modeling and Experiments, *Optical and Quantum Electronics*, Vol. 50, p. 18, 2017.

[147] N.-P. Harder and M. A. Green, Thermophotonics, *Semiconductor Science and Technology*, Vol. 18, pp. S270-S278, 2003.

[148] M. A. Green, Third Generation Photovoltaics: Ultra-High Conversion Efficiency at Low Cost, *Progress in Photovoltaics: Research and Applications*, Vol. 9, pp. 123-135, 2001.

[149] T. Sadi, I. Radevici, and J. Oksanen, Thermophotonic Cooling with Light-Emitting Diodes, *Nature Photonics*, Vol. 14, pp. 205-214, 2020.

[150] K.-C. Lee and S.-T. Yen, 2017, "Electroluminescent Refrigerators," in *Handbook of Optoelectronic Device Modeling and Simulation*, ed: CRC Press, pp. 541-560.

[151] P. Santhanam, D. Huang, D. Gray, and R. Ram, Electro-Luminescent Cooling: Light Emitting Diodes above Unity Efficiency, SPIE, 2013.

[152] K. Chen, P. Santhanam, S. Sandhu, L. Zhu, and S. Fan, Heat-Flux Control and Solid-State Cooling by Regulating Chemical Potential of Photons in Near-Field Electromagnetic Heat Transfer, *Physical Review B*, Vol. 91, p. 134301, 2015.

[153] K. Chen, T. P. Xiao, P. Santhanam, E. Yablonovitch, and S. Fan, High-Performance Near-Field Electroluminescent Refrigeration Device Consisting of a GaAs Light Emitting Diode and a Si Photovoltaic Cell, *Journal of Applied Physics*, Vol. 122, p. 143104, 2017.

[154] J. Song, J. Jang, M. Lim, J. Lee, S. S. Lee, and B. J. Lee, Near-Field Electroluminescent Refrigeration System Consisting of Two Graphene Schottky Diodes, *Journal of Heat Transfer*, Vol. 142, 2020.

[155] P. Berdahl, Radiant Refrigeration by Semiconductor Diodes, *Journal of Applied Physics*, Vol. 58, pp. 1369-1374, 1985.

[156] A. R. Adams, C. T. Elliott, A. Krier, B. N. Murdin, and C. T. Elliott, Negative Luminescence and Its Applications, *Philosophical Transactions of the Royal Society of London. Series A: Mathematical, Physical and Engineering Sciences*, Vol. 359, pp. 567-579, 2001.

[157] V. I. Ivanov-Omskii and B. A. Matveev, Negative Luminescence and Devices Based on this Phenomenon, *Semiconductors*, Vol. 41, pp. 247-258, 2007.

[158] L. Zhu, A. Fiorino, D. Thompson, R. Mittapally, E. Meyhofer, and P. Reddy, Near-Field Photonic Cooling through Control of the Chemical Potential of Photons, *Nature*, Vol. 566, pp. 239-244, 2019.

[159] M. Auslender and S. Hava, Scattering-Matrix Propagation Algorithm in Full-Vectorial Optics of Multilayer Grating Structures, *Optics Letters*, Vol. 21, pp. 1765-1767, 1996.

[160] J. Drevillon, "Design Ab-Initio De Matériaux Micro Et Nanostructurés Pour L'émission Thermique Cohérente En Champ Proche Et En Champ Lointain," Université de Nantes, 2007.

[161] G. J. Kovacs, 1982, "Optical Excitation of Surface Plasmon-Polaritons in Layered Media," in *Electromagnetic Surface Modes*, Boardman, A. D., Ed., ed New York: Wiley.

[162] X. L. Liu, R. Z. Zhang, and Z. M. Zhang, Near-Field Radiative Heat Transfer with Doped-Silicon Nanostructured Metamaterials, *International Journal of Heat and Mass Transfer*, Vol. 73, pp. 389-398, 2014.

[163] J. Nelson, The Physics of Solar Cells, World Scientific Publishing Company, 2003.

[164] D. A. Neamen, Semiconductor Physics and Devices: Basic Principles, New York, NY: McGraw-Hill, 2012.

[165] S. Selberherr, Analysis and Simulation of Semiconductor Devices, Springer Science & Business Media, 2012.

[166] D. Vasileska and S. M. Goodnick, Computational Electronics, *Synthesis Lectures on Computational Electromagnetics*, Vol. 1, pp. 1-216, 2006.

[167] D. L. Scharfetter and H. K. Gummel, Large-Signal Analysis of a Silicon Read Diode Oscillator, *IEEE Transactions on Electron Devices*, Vol. 16, pp. 64-77, 1969.

[168] R. Vaillon, L. Robin, C. Muresan, and C. Ménézo, Modeling of Coupled Spectral Radiation, Thermal and Carrier Transport in a Silicon Photovoltaic Cell, *International Journal of Heat and Mass Transfer*, Vol. 49, pp. 4454-4468, 2006.

[169] W. D. Eades and R. M. Swanson, Calculation of Surface Generation and Recombination Velocities at the Si-SiO_2 Interface, *Journal of Applied Physics*, Vol. 58, pp. 4267-4276, 1985.

[170] O. J. Sandberg and A. Armin, On the Effect of Surface Recombination in Thin Film Solar Cells, Light Emitting Diodes and Photodetectors, *Synthetic Metals*, Vol. 254, pp. 114-121, 2019.

[171] D. Y. Petrovykh, J. P. Long, and L. J. Whitman, Surface Passivation of InAs(001) with Thioacetamide, *Applied Physics Letters*, Vol. 86, p. 242105, 2005.

[172] B. Gaury, Y. Sun, P. Bermel, and P. M. Haney, Sesame: A 2-Dimensional Solar Cell Modeling Tool, *Solar Energy Materials and Solar Cells*, Vol. 198, pp. 53-62, 2019.

[173] W. Shockley and H. J. Queisser, Detailed Balance Limit of Efficiency of P-N Junction Solar Cells, *Journal of Applied Physics*, Vol. 32, pp. 510-519, 1961.

[174] S. M. Sze and K. K. Ng, Physics of Semiconductor Devices, John Wiley & Sons, 2006.

[175] M. Zenker, A. Heinzel, G. Stollwerck, J. Ferber, and J. Luther, Efficiency and Power Density Potential of Combustion-Driven Thermophotovoltaic Systems Using GaSb Photovoltaic Cells, *IEEE Transactions on Electron Devices*, Vol. 48, pp. 367-376, 2001.

[176] B. Zhao, P. Santhanam, K. Chen, S. Buddhiraju, and S. Fan, Near-Field Thermophotonic Systems for Low-Grade Waste-Heat Recovery, *Nano Letters*, Vol. 18, pp. 5224-5230, 2018.

[177] C. Lin, B. Wang, K. H. Teo, and Z. Zhang, A Coherent Description of Thermal Radiative Devices and Its Application on the Near-Field Negative Electroluminescent Cooling, *Energy*, Vol. 147, pp. 177-186, 2018.

[178] X. Liu, L. Wang, and Z. M. Zhang, Near-Field Thermal Radiation: Recent Progress and Outlook, *Nanoscale and Microscale Thermophysical Engineering*, Vol. 19, pp. 98-126, 2015.

[179] S. Basu and Z. M. Zhang, Maximum Energy Transfer in Near-Field Thermal Radiation at Nanometer Distances, *Journal of Applied Physics*, Vol. 105, p. 093535, 2009.

[180] S. Adachi, Material Parameters of $In_{1-x}Ga_xAs_yP_{1-y}$ and Related Binaries, *Journal of Applied Physics*, Vol. 53, pp. 8775-8792, 1982.

[181] E. D. Palik, Handbook of Optical Constants of Solids Academic press, 1998.

[182] M. A. Green, Self-Consistent Optical Parameters of Intrinsic Silicon at 300 K Including Temperature Coefficients, *Solar Energy Materials and Solar Cells*, Vol. 92, pp. 1305-1310, 2008.

[183] N. M. Ravindra and B. Prasad, Saturation Current in Solar Cells: an Analysis, *Solar Cells*, Vol. 2, pp. 109-113, 1980.

[184] S. Basu, Y.-B. Chen, and Z. M. Zhang, Microscale Radiation in Thermophotovoltaic Devices – A Review, *International Journal of Energy Research*, Vol. 31, pp. 689-716, 2007.

[185] A. Martí, J. L. Balenzategui, and R. F. Reyna, Photon Recycling and Shockley's Diode Equation, *Journal of Applied Physics*, Vol. 82, pp. 4067-4075, 1997.

[186] Q. Lu, X. Zhou, A. Krysa, A. Marshall, P. Carrington, C.-H. Tan, and A. Krier, InAs Thermophotovoltaic Cells with High Quantum Efficiency for Waste Heat Recovery Applications Below 1000°C, *Solar Energy Materials and Solar Cells*, Vol. 179, pp. 334-338, 2018.

[187] D. Milovich, J. Villa, E. Antolin, A. Datas, A. Marti, R. Vaillon, and M. Francoeur, Design of an Indium Arsenide Cell for Near-Field Thermophotovoltaic Devices, *Journal of Photonics for Energy*, Vol. 10, p. 025503, 2020.

[188] M. Levinshtein and S. Rumyantsev, Handbook Series on Semiconductor Parameters, World Scientific, Singapore, 1996.

[189] M. Sotoodeh, A. H. Khalid, and A. A. Rezazadeh, Empirical Low-Field Mobility Model for III–V Compounds Applicable in Device Simulation Codes, *Journal of Applied Physics*, Vol. 87, pp. 2890-2900, 2000.

[190] T. Burger, C. Sempere, B. Roy-Layinde, and A. Lenert, Present Efficiencies and Future Opportunities in Thermophotovoltaics, *Joule*, Vol. 4, pp. 1660-1680, 2020.

[191] J. Fernández, F. Dimroth, E. Oliva, M. Hermle, and A. W. Bett, Back-Surface Optimization of Germanium TPV Cells, *AIP Conference Proceedings*, Vol. 890, pp. 190-197, 2007.

[192] D. Fan, T. Burger, S. Mcsherry, B. Lee, A. Lenert, and S. R. Forrest, Near-Perfect Photon Utilization in an Air-Bridge Thermophotovoltaic Cell, *Nature*, Vol. 586, pp. 237-241, 2020.

[193] T. Inoue, T. Suzuki, K. Ikeda, T. Asano, and S. Noda, Near-Field Thermophotovotaic Devices with Surrounding Non-Contact Reflectors for Efficient Photon Recycling, *Optics Express*, Vol. 29, pp. 11133-11143, 2021.

[194] Y. Da and Y. Xuan, Role of Surface Recombination in Affecting the Efficiency of Nanostructured Thin-Film Solar Cells, *Optics Express*, Vol. 21, pp. A1065-A1077, 2013.

[195] U. Rau, Reciprocity Relation between Photovoltaic Quantum Efficiency and Electroluminescent Emission of Solar Cells, *Physical Review B*, Vol. 76, p. 085303, 2007.

[196] S. Basu and Z. M. Zhang, Ultrasmall Penetration Depth in Nanoscale Thermal Radiation, *Applied Physics Letters*, Vol. 95, p. 133104, 2009.

[197] W. Van Roosbroeck and W. Shockley, Photon-Radiative Recombination of Electrons and Holes in Germanium, *Physical Review*, Vol. 94, pp. 1558-1560, 1954.

[198] T. Trupke, M. A. Green, P. Würfel, P. P. Altermatt, A. Wang, J. Zhao, and R. Corkish, Temperature Dependence of the Radiative Recombination Coefficient of Intrinsic Crystalline Silicon, *Journal of Applied Physics*, Vol. 94, pp. 4930-4937, 2003.

[199] J.-J. Greffet, P. Bouchon, G. Brucoli, and F. Marquier, Light Emission by Nonequilibrium Bodies: Local Kirchhoff Law, *Physical Review X*, Vol. 8, p. 021008, 2018.

[200] W. W. Anderson, Absorption Constant of $Pb_{1-x}Sn_xTe$ and $Hg_{1-x}Cd_xTe$ Alloys, *Infrared Physics*, Vol. 20, pp. 363-372, 1980.

[201] Z. Djuric, B. Livada, V. Jovic, M. Smiljanic, M. Matic, and Z. Lazic, Quantum Efficiency and Responsivity of InSb Photodiodes Utilizing the Moss-Burstein Effect, *Infrared Physics*, Vol. 29, pp. 1-7, 1989.

[202] J. S. C. Prentice, Coherent, Partially Coherent and Incoherent Light Absorption in Thin-Film Multilayer Structures, *Journal of Physics D: Applied Physics*, Vol. 33, pp. 3139-3145, 2000.

[203] T. S. Moss, The Interpretation of the Properties of Indium Antimonide, *Proceedings of the Physical Society. Section B*, Vol. 67, pp. 775-782, 1954.

[204] E. Burstein, Anomalous Optical Absorption Limit in InSb, *Physical Review*, Vol. 93, pp. 632-633, 1954.

[205] C. R. Otey, W. T. Lau, and S. Fan, Thermal Rectification through Vacuum, *Physical Review Letters*, Vol. 104, p. 154301, 2010.

[206] L. P. Wang and Z. M. Zhang, Thermal Rectification Enabled by Near-Field Radiative Heat Transfer between Intrinsic Silicon and a Dissimilar Material, *Nanoscale and Microscale Thermophysical Engineering*, Vol. 17, pp. 337-348, 2013.

[207] S. Basu and M. Francoeur, Near-Field Radiative Transfer Based Thermal Rectification Using Doped Silicon, *Applied Physics Letters*, Vol. 98, p. 113106, 2011.

[208] L. Tang and M. Francoeur, Photonic Thermal Diode Enabled by Surface Polariton Coupling in Nanostructures, *Optics Express*, Vol. 25, pp. A1043-A1052, 2017.

[209] E. Nefzaoui, J. Drevillon, Y. Ezzahri, and K. Joulain, Simple Far-Field Radiative Thermal Rectifier Using Fabry–Perot Cavities Based Infrared Selective Emitters, *Applied Optics*, Vol. 53, pp. 3479-3485, 2014.

[210] P. Ben-Abdallah and S.-A. Biehs, Contactless Heat Flux Control with Photonic Devices, *AIP Advances*, Vol. 5, p. 053502, 2015.

[211] M. Lim, J. Song, S. S. Lee, and B. J. Lee, Tailoring near-Field Thermal Radiation between Metallo-Dielectric Multilayers Using Coupled Surface Plasmon Polaritons, *Nature Communications*, Vol. 9, p. 4302, 2018.

[212] P. J. Van Zwol, L. Ranno, and J. Chevrier, Tuning near Field Radiative Heat Flux through Surface Excitations with a Metal Insulator Transition, *Physical Review Letters*, Vol. 108, p. 234301, 2012.

[213] K. Ito, K. Nishikawa, A. Miura, H. Toshiyoshi, and H. Iizuka, Dynamic Modulation of Radiative Heat Transfer Beyond the Blackbody Limit, *Nano Letters*, Vol. 17, pp. 4347-4353, 2017.

[214] A. Fiorino, D. Thompson, L. Zhu, R. Mittapally, S.-A. Biehs, O. Bezencenet, N. El-Bondry, S. Bansropun, P. Ben-Abdallah, E. Meyhofer, and P. Reddy, A Thermal Diode Based on Nanoscale Thermal Radiation, *ACS Nano*, Vol. 12, pp. 5774-5779, 2018.

[215] M. Elzouka and S. Ndao, High Temperature Near-Field Nanothermomechanical Rectification, *Scientific Reports*, Vol. 7, p. 44901, 2017.

[216] J. Huang, Q. Li, Z. Zheng, and Y. Xuan, Thermal Rectification Based on Thermochromic Materials, *International Journal of Heat and Mass Transfer*, Vol. 67, pp. 575-580, 2013.

[217] Y. Yang, S. Basu, and L. Wang, Radiation-Based Near-Field Thermal Rectification with Phase Transition Materials, *Applied Physics Letters*, Vol. 103, p. 163101, 2013.

[218] P. Ben-Abdallah and S.-A. Biehs, Phase-Change Radiative Thermal Diode, *Applied Physics Letters*, Vol. 103, p. 191907, 2013.

[219] K. Ito, K. Nishikawa, H. Iizuka, and H. Toshiyoshi, Experimental Investigation of Radiative Thermal Rectifier Using Vanadium Dioxide, *Applied Physics Letters*, Vol. 105, p. 253503, 2014.

[220] A. Ghanekar, G. Xiao, and Y. Zheng, High Contrast Far-Field Radiative Thermal Diode, *Scientific Reports*, Vol. 7, p. 6339, 2017.

[221] S. O. Kasali, J. Ordonez-Miranda, and K. Joulain, Optimization of the Rectification Factor of Radiative Thermal Diodes Based on Two Phase-Change Materials, *International Journal of Heat and Mass Transfer*, Vol. 154, p. 119739, 2020.

[222] Z. Zheng, X. Liu, A. Wang, and Y. Xuan, Graphene-Assisted Near-Field Radiative Thermal Rectifier Based on Phase Transition of Vanadium Dioxide (VO_2), *International Journal of Heat and Mass Transfer*, Vol. 109, pp. 63-72, 2017.

[223] G. Xu, J. Sun, H. Mao, and T. Pan, Highly Efficient Near-Field Thermal Rectification between InSb and Graphene-Coated SiO_2, *Journal of Quantitative Spectroscopy and Radiative Transfer*, Vol. 220, pp. 140-147, 2018.

[224] S. Wen, X. Liu, S. Cheng, Z. Wang, S. Zhang, and C. Dang, Ultrahigh Thermal Rectification Based on Near-Field Thermal Radiation between Dissimilar Nanoparticles, *Journal of Quantitative Spectroscopy and Radiative Transfer*, Vol. 234, pp. 1-9, 2019.

[225] J. Shen, X. Liu, H. He, W. Wu, and B. Liu, High-Performance Noncontact Thermal Diode via Asymmetric Nanostructures, *Journal of Quantitative Spectroscopy and Radiative Transfer*, Vol. 211, pp. 1-8, 2018.

[226] F. Chen, X. Liu, Y. Tian, and Y. Zheng, Dynamic Tuning of Near-Field Radiative Thermal Rectification, *Advanced Engineering Materials*, Vol. 23, p. 2000825, 2021.

[227] J. Ordonez-Miranda, K. Joulain, D. D. S. Meneses, Y. Ezzahri, and J. Drevillon, Photonic Thermal Diode Based on Superconductors, *Journal of Applied Physics*, Vol. 122, p. 093105, 2017.

[228] E. Moncada-Villa and J. C. Cuevas, Normal-Metal–Superconductor Near-Field Thermal Diodes and Transistors, *Physical Review Applied*, Vol. 15, p. 024036, 2021.

[229] P. Y. Liu and J. C. Maan, Optical Properties of InSb between 300 and 700 K. I. Temperature Dependence of the Energy Gap, *Physical Review B*, Vol. 47, pp. 16274-16278, 1993.

[230] G. W. Gobeli and H. Y. Fan, Infrared Absorption and Valence Band in Indium Antimonide, *Physical Review*, Vol. 119, pp. 613-620, 1960.

[231] A. Poddubny, I. Iorsh, P. Belov, and Y. Kivshar, Hyperbolic Metamaterials, *Nature Photonics*, Vol. 7, pp. 948-957, 2013.

[232] X. Liu, R. Z. Zhang, and Z. Zhang, Near-Perfect Photon Tunneling by Hybridizing Graphene Plasmons and Hyperbolic Modes, *ACS Photonics*, Vol. 1, pp. 785-789, 2014.

[233] A. Kumar, T. Low, K. H. Fung, P. Avouris, and N. X. Fang, Tunable Light–Matter Interaction and the Role of Hyperbolicity in Graphene–hBN System, *Nano Letters*, Vol. 15, pp. 3172-3180, 2015.

[234] B. Zhao and Z. M. Zhang, Enhanced Photon Tunneling by Surface Plasmon–Phonon Polaritons in Graphene/hBN Heterostructures, *Journal of Heat Transfer*, Vol. 139, 2016.

[235] X. Wu and C. Fu, Near-Field Radiative Heat Transfer between Uniaxial Hyperbolic Media: Role of Volume and Surface Phonon Polaritons, *Journal of Quantitative Spectroscopy and Radiative Transfer*, Vol. 258, p. 107337, 2021.

[236] O. D. Miller, E. Yablonovitch, and S. R. Kurtz, Strong Internal and External Luminescence as Solar Cells Approach the Shockley–Queisser Limit, *IEEE Journal of Photovoltaics*, Vol. 2, pp. 303-311, 2012.

[237] Z. M. Fang, K. Y. Ma, D. H. Jaw, R. M. Cohen, and G. B. Stringfellow, Photoluminescence of InSb, InAs, and InAsSb Grown by Organometallic Vapor Phase Epitaxy, *Journal of Applied Physics*, Vol. 67, pp. 7034-7039, 1990.

[238] T. S. Moss, S. D. Smith, and T. D. F. Hawkins, Absorption and Dispersion of Indium Antimonide, *Proceedings of the Physical Society. Section B*, Vol. 70, pp. 776-784, 1957.

[239] S. W. Kurnick and J. M. Powell, Optical Absorption in Pure Single Crystal InSb at 298° and 78° K, *Physical Review*, Vol. 116, pp. 597-604, 1959.

[241] D. Feng, S. K. Yee, and Z. M. Zhang, Near-Field Photonic Thermal Diode Based on hBN and InSb film, *Applied Physics Letters*, Vol. 119, p. 181111, 2021.

[241] X. Zhang, Y. S. Ang, J. C. Chen, and L. K. Ang, Design of an InSb Thermoradiative System for Harvesting Low-Grade Waste Heat, *Optics Letters*, Vol. 44, pp. 3354-3357, 2019.

[242] T. J. Bright, X. L. Liu, and Z. M. Zhang, Energy Streamlines in Near-Field Radiative Heat Transfer between Hyperbolic Metamaterials, *Optics Express*, Vol. 22, pp. A1112-A1127, 2014.

[243] D. Feng, S. K. Yee, and Z. M. Zhang, Spatial Effect on the External Radiative Recombination in Thin-Film Near-Field Radiative Energy Converters, *arXiv preprint arXiv:2111.10996*